

**STRUCTURAL STUDIES OF SUPRAMOLECULAR
MICROPOROUS MATERIALS**

Miss Aungkana Chatkon

A Thesis Submitted in Partial Fulfillment of the Requirements

for the Degree of Master of Science in Chemistry

Suranaree University of Technology

Academic Year 2001

ISBN 974-533-074-4

การศึกษาโครงสร้างของวัสดุซูปราโมเลกุลาร์ที่มีรูพรุนขนาดเล็ก

นางสาวอังคณา ชาติก้อน

วิทยานิพนธ์นี้เป็นส่วนหนึ่งของการศึกษาตามหลักสูตรปริญญาวิทยาศาสตรมหาบัณฑิต

สาขาวิชาเคมี

มหาวิทยาลัยเทคโนโลยีสุรนารี

ปีการศึกษา 2544

ISBN 974-533-074-4

STRUCTURAL STUDIES OF SUPRAMOLECULAR MICROPOROUS MATERIALS

**Suranaree University of Technology Council has approved this thesis,
submitted in partial fulfillment of the requirements for a Master's Degree.**

Thesis Examining Committee

.....
(Asst. Prof. Dr. Malee Tangsathitkulchai)
Chairman

.....
(Assoc. Prof. Dr. Kenneth J. Haller)
Thesis Advisor

.....
(Asst. Prof. Dr. Kunwadee Rangriwatananon)
Committee

.....
(Assoc. Prof. Dr. Tawit Chitsomboon)
Vice Rector for Academic Affairs

.....
(Assoc. Prof. Dr. Prasart Suebka)
Dean of the Institute of Science

อังคณา ชาติก้อน: การศึกษาโครงสร้างของวัสดุซูปราโมเลกุลที่มีรูพรุนขนาดเล็ก
(STRUCTURAL STUDIES OF SUPRAMOLECULAR MICROPOROUS MATERIALS)

อาจารย์ที่ปรึกษา : รศ. ดร. เค็นเนท เจ. แสลดอร์, 95 หน้า. ISBN 974-533-074-4

วิทยานิพนธ์นี้เป็นการศึกษาโครงสร้างของวัสดุที่สังเคราะห์ขึ้นภายใต้เงื่อนไขที่จะนำไปสู่วัสดุที่เป็นซูปราโมเลกุลที่มีรูพรุนขนาดเล็ก และสำหรับสารที่มีโครงสร้างผลึกเหมือนกันของ $MV_2O_6 \cdot 2H_2O$ เมื่อ M เป็น Ni, Co อยู่ใน space group *Pmma* โครงสร้างของผลึกประกอบด้วย ทรงเหลี่ยมสี่หน้าของ VO_4 เชื่อมต่อกันเป็นโซ่ผ่านทางมุมของออกซิเจนสองอะตอมในทิศทาง [100] โดยระหว่างโซ่ของ VO_4 ที่อยู่ใกล้กันจะเชื่อมต่อกันด้วยทรงเหลี่ยมแปดหน้าของ MO_6 โดยออกซิเจนทั้งสี่อะตอมบนแกน equatorial ของโลหะเกิดพันธะกับอะตอมของวาเนเดียม VO_4 ในโซ่ที่ต่างกัน และออกซิเจนอะตอมบนแกน axial จะเป็นออกซิเจนของโมเลกุลน้ำ สำหรับสารประกอบของ $CoV_2O_6 \cdot 2H_2O$ ที่ตีพิมพ์แล้วนั้น ได้รายงานผลที่ได้จากเครื่องมือที่มีอำนาจในการจำแนกค่า พบว่าความยาวพันธะของ Co-O ของโมเลกุลน้ำมีความสมดุลกัน แต่ปรากฏว่ามีสองฟิสิกส์ในกระบวนการสูญเสียจากการวิเคราะห์ผลของ thermogravimetric ในการนำข้อมูลมาศึกษาใหม่ด้วยเครื่องมือที่มีประสิทธิภาพสูงจะให้ค่า $R_1 = 0.026$ โดยนำโมเลกุลที่หนึ่งจะให้ไฮโดรเจนทั้งสองอะตอมกับออกซิเจนที่เป็น mirror related ของโซ่ VO_4 เพื่อเกิดพันธะไฮโดรเจน และรับไฮโดรเจนจากน้ำโมเลกุลที่สองในการเกิดพันธะไฮโดรเจนกับอิเล็กตรอนคู่โดดเดี่ยวของออกซิเจน สำหรับน้ำโมเลกุลที่สองจะเกิดการ disordered จาก mirror plane เนื่องจากอะตอมของไฮโดรเจนที่เหลือเกิดพันธะไฮโดรเจนกับออกซิเจนหนึ่งในสองอะตอมที่สมดุลกันในโซ่ของ VO_4 และโครงสร้างแสดงความยาวพันธะที่ไม่สมดุลกันของ Co-O ของโมเลกุลน้ำซึ่งมีค่าเท่ากับ 2.117(2) และ 2.079(2) Å ตามลำดับ โดยมีพันธะไฮโดรเจนในช่องว่างของโครงผลึกและหากดึงน้ำออกจากช่องว่างของโครงผลึกจะทำให้โครงผลึกเสียรูปทรง สำหรับ $NiV_2O_6 \cdot 2H_2O$ จะมีโครงสร้างเหมือนกับสารประกอบของโคบอลต์ ซึ่งความยาวพันธะที่ไม่สมดุลกันของ Ni-O ของโมเลกุลน้ำมีค่าเท่ากับ 2.066(3) และ 2.030(3) Å ตามลำดับ และให้ค่า $R_1 = 0.030$

ผลึกของ $[enH_2]_5[V_6B_{20}O_{50}H_8] \cdot 7H_2O$ อยู่ใน space group *C2/c*, $Z = 4$ มี inversion centers ภายในคลัสเตอร์ โดยกลุ่มอะตอมที่อยู่ตรงกลางของคลัสเตอร์คือ V_6O_{18} ซึ่งเกิดจากการเชื่อมต่อกันด้วยขอบของพีระมิดฐานสี่เหลี่ยมของวาเนดิลจำนวนหกหมู่ (V^{+4}) ด้านบนและด้านล่างของกลุ่มอะตอมเป็นกลุ่มแพโพลิโบเรตลิแกนด $[B_{10}O_{16}H_4]^{10-}$ ที่เชื่อมต่อกันด้วยอะตอมออกซิเจนของลิแกนดที่ซึ่งส่วนปลายของแต่ละลิแกนดเป็นหมู่ไฮดรอกซิลจำนวนสี่หมู่ ที่จะเกิดพันธะไฮโดรเจนระหว่างคลัสเตอร์ที่อยู่ใกล้เคียง ผ่านไฮโดรเจนอะตอมของหมู่ไฮดรอกซิลในการจัดตัวในสามมิติเป็นสารซูปราโมเลกุลที่มีรูพรุนในโครงสร้าง เอธิลีนไดแอมโมเนียมและโมเลกุลของน้ำซึ่งมีประมาณ $1/3$ ของปริมาตรผลึก จะเกิดพันธะไฮโดรเจนซึ่งกันและกันในรูปแบบพันธะ O-H...O และ N-H...O และบรรจุในช่องว่างรอบๆ คลัสเตอร์ ความยาวพันธะและมุมพันธะมีค่าปกติโดยให้ค่า $R_1 = 0.048$

สาขาวิชาเคมี
ปีการศึกษา 2544

ลายมือชื่อนักศึกษา
ลายมือชื่ออาจารย์ที่ปรึกษา
ลายมือชื่ออาจารย์ที่ปรึกษาร่วม
ลายมือชื่ออาจารย์ที่ปรึกษาร่วม

**AUNGKANA CHATKON: STRUCTURAL STUDIES OF SUPRAMOLECULAR
MICROPOROUS MATERIALS**

THESIS ADVISOR: ASSOCIATE PROFESSOR KENNETH J. HALLER, Ph.D.,

95 PP. ISBN 974-533-074-4

Structural studies of materials synthesized under conditions that generally lead to microporous supramolecular materials are presented in this thesis.

The isomorphous $MV_2O_6 \cdot 2H_2O$ ($M = Ni, Co$) compounds crystallize in the orthorhombic space group *Pnma* and consist of VO_4 tetrahedra vertex-linked through two of the oxygen atoms into chains along the [100] direction. Adjacent VO_4 chains are interconnected by MO_6 octahedra where each of the four equatorial oxygen atoms is shared with a VO_4 oxygen atom of a different VO_4 chain, and the axial oxygen atoms are waters of hydration. $CoV_2O_6 \cdot 2H_2O$ has been reported as a low resolution structure with equivalent Co-O bonds for the waters of hydration, but with two peaks in the dehydration process by thermogravimetric analysis. The current study provides a high quality structure, $R_1=0.026$. One water molecule is ordered and uses all three hydrogen bonds, donating both H atoms to form O-H...O hydrogen bonds to mirror related O of the VO_4 chains, and accepting one H from the second water molecule. The second water molecule is disordered off of the mirror plane by its second H bond which forms to one of two equivalent VO_4 chain O atoms (it is not an H-bond acceptor). The structure thus demonstrates nonequivalent coordination of the waters, both in Co-O distances, 2.117(2) and 2.079(2) Å, and in the hydrogen bonding environment within the pores of the lattice framework. Removing the waters from the pores results in collapse of the lattice. $NiV_2O_6 \cdot 2H_2O$, $R_1=0.030$, has the same disorder and nonequivalent water features with Ni-O distances of 2.066(3) and 2.030(3) Å.

$[enH_2]_5[V_6B_{20}O_{50}H_8] \cdot 7H_2O$ crystallizes in monoclinic space group *C2/c*, $Z=4$, with the clusters on inversion centers. The cluster has a central V_6O_{18} band of six edge sharing square-pyramidal vanadyl (V^{+4}) groups, capped top and bottom through the basal oxygen atoms by raft-like $[B_{10}O_{16}H_4]^{-10}$ polyborate ligands, each terminated by four hydroxyl groups. O-H...O hydrogen bonds interconnect adjacent clusters through the hydroxyl H atoms into a porous three dimensional supramolecular array. The ethylenediammonium dications and water molecules (approximately $1/3$ of the crystal volume) engage in extensive O-H...O and N-H...O hydrogen bonding with each other and the cluster filling the channels surrounding the clusters. Cluster bond lengths and angles are within normal values. Final $R_1=0.048$.

School of Chemistry

Academic Year 2001

Student

Advisor

Coadvisor

Coadvisor

Acknowledgments

I would like to express my sincere thanks to my supervisor, Assoc. Prof. Dr. Kenneth J. Haller. Without his long-term guidance and patient help this thesis would not be possible.

I would also like to express my gratitude to all the teachers of the School of Chemistry who taught and helped me during my study at SUT in the School of Chemistry. I wish to express my special thanks to the chairman of the School of Chemistry, Asst. Prof. Dr. Malee Tangsathikulchai and Asst. Prof. Dr. Kunwadee Rangriwatananon for their warm hearted support, encouragement, and help.

Thanks to Suranaree University of Technology for a Research Grant to support my thesis research, and for a Travel Grant to support my attendance at the 27th Science and Technology of Thailand meeting in Haad Yai, Thailand. Thanks to the Asian Crystallographic Association for a Bursary Award to support my attendance at AsCA'01, the 4th meeting of the Asian Crystallographic Association in Bangalore, India, and to MacScience Co. Ltd. for a Registration Grant for the same meeting.

Figure 3.1 is reproduced with permission of the CEM Corporation, and Figures A.1 and A.2 are created from the *International Tables for Crystallography* as permitted by the International Union of Crystallography. Thanks to both sources.

Finally, I thank my friends in the group and my family for their love, devotion, understanding, consultation, and consolation for my success in my studies.

Aungkana Chatkon

Contents

	Page
Abstract in Thai	I
Abstract in English	II
Acknowledgments	III
Contents	IV
List of Tables	VI
List of Figures	VII
List of Symbols and Abbreviations	IX
Chapters	
I Introduction	1
II Theory of Single Crystal X-ray Diffraction	13
2.1 Introduction	13
2.2 Source of X-rays	13
2.3 Crystalline State	16
2.4 Diffraction and the Bragg Equation	22
2.5 Diffraction by Atoms or Groups of Atoms in Crystals	23
2.6 Structure Factor and Electron Density	24
III Instrumentation, Materials, and Techniques	29
3.1 Instrumentation	29
3.2 Materials	32
3.3 Techniques	34
IV $MV_2O_6 \cdot 2H_2O$, $M = Co, Ni$	41
4.1 Introduction	41
4.2 Experimental, $NiV_2O_6 \cdot 2H_2O$	42
4.3 Structure Description, $NiV_2O_6 \cdot 2H_2O$	47
4.4 Structure of $CoV_2O_6 \cdot 2H_2O$	54
4.5 FTIR Experiment	60
4.6 Thermal Analysis: Dehydration	61
V $[enH_2]_5[V_6B_{20}O_{50}H_8] \cdot 7H_2O$	65
5.1 Introduction	65
5.2 Experimental	65
5.3 Structure Description	73

Contents (Continued)

	Page
VI Conclusions	81
References	84
Appendices	
Appendix A Space Group Tables	89
Appendix B Bond Valence Calculation	91
Appendix C Ring Fourier Calculation	92
Curriculum Vitae	95

List of Tables

Table	Page
1.1 Pore Size Classification and Important Porous Inorganic Materials	5
1.2 Metamorphosis of the Vanadium Coordination Polyhedra	10
1.3 Bond Lengths in V-O _n Polyhedra	10
2.1. Crystal Systems	18
3.1. Hydrothermal Reactions of 5 hr Duration	35
3.2. Hydrothermal Reactions of 15 hr Duration	36
4.1 Crystal Data for the Isomorphous MV ₂ O ₆ ·2H ₂ O Compounds	45
4.2 Fractional Monoclinic Coordinates and Isotropic Atomic Displacement Parameters for NiV ₂ O ₆ ·2H ₂ O	46
4.3 Anisotropic Atomic Displacement Parameters for NiV ₂ O ₆ ·2H ₂ O	46
4.4 Selected Interatomic Distances and Angles for NiV ₂ O ₆ ·2H ₂ O	49
4.5 Hydrogen Bond Parameters for NiV ₂ O ₆ ·2H ₂ O	49
4.6 Bond Valence Sums for Atoms in NiV ₂ O ₆ ·2H ₂ O	54
4.7 Fractional Orthorhombic Coordinates and Isotropic Atomic Displacement Parameters for CoV ₂ O ₆ ·2H ₂ O	56
4.8 Anisotropic Atomic Displacement Parameters for CoV ₂ O ₆ ·2H ₂ O	56
4.9 Selected Interatomic Distances and Angles for CoV ₂ O ₆ ·2H ₂ O	57
4.10 Hydrogen Bonding of CoV ₂ O ₆ ·2H ₂ O	57
4.11 Bond Valence Sums for Atoms in CoV ₂ O ₆ ·2H ₂ O	58
4.12 Bond Valence Sums for Atoms in α-Ni(VO ₃) ₂ ·2H ₂ O	59
4.13 XRD Results of NiV ₂ O ₆ ·2H ₂ O	63
5.1 Crystal Data for [enH ₂] ₅ [V ₆ B ₂₀ O ₅₀ H ₈]·7H ₂ O	69
5.2 Fractional Monoclinic Coordinates and Equivalent Atomic Displacement Parameters for [enH ₂] ₅ [V ₆ B ₂₀ O ₅₀ H ₈]·7H ₂ O	70
5.3 Selected Interatomic Bond Distances (Å) and Angles(Deg) for the [V ₆ B ₂₀ O ₅₀ H ₈] ⁻¹⁰ Cluster	72
5.4 Hydrogen Bond Parameters for [enH ₂] ₅ [V ₆ B ₂₀ O ₅₀ H ₈]·7H ₂ O	78

List of Figures

Figure	Page
1.1 Selection of Supramolecular Synthons	2
1.2 Nine Porphyrin and Twelve Palladium Moieties Assembled into a Nanosieve Array	4
1.3 Diagram of Vanadium Redox Battery	12
2.1 Schematic Diagram of an X-ray Tube	14
2.2 X-ray Spectra with Characteristic Peaks	15
2.3 Unit Cells and Lattices	16
2.4 The Bravais Lattices	19
2.5 Tetragonal Lattices Illustrating Cell Centering	20
2.6 Reflection Combined with Two-Fold Rotation	21
2.7 Reflection of an X-ray Beam	22
2.8 The Relationship between Real and Reciprocal Lattices	23
2.9 Atomic Scattering Factor Curves	24
2.10 Vector Representation of the Structure Factor	25
3.1 HP-500 Plus Pressure/Temperature Control Vessel Assembly	31
3.2 EDX Spectrum of $\text{NiV}_2\text{O}_6 \cdot 2\text{H}_2\text{O}$	37
3.3 TGA curve of $\text{NiV}_2\text{O}_6 \cdot 2\text{H}_2\text{O}$	38
3.4 Thermodiffraction from XRD	40
4.1 Disorder Model for O3 in $\text{NiV}_2\text{O}_6 \cdot 2\text{H}_2\text{O}$	44
4.2 $\text{NiV}_2\text{O}_6 \cdot 2\text{H}_2\text{O}$ Showing NiO_6 and VO_4 Coordination	48
4.3 Hydrogen Bonding of $\text{NiV}_2\text{O}_6 \cdot 2\text{H}_2\text{O}$	50
4.4 Structure of $\text{NiV}_2\text{O}_6 \cdot 2\text{H}_2\text{O}$ Projected Parallel to [100]	52
4.5 Structure of $\text{NiV}_2\text{O}_6 \cdot 2\text{H}_2\text{O}$ Projected Parallel to [010]	53
4.6 Structure of $\text{CoV}_2\text{O}_6 \cdot 2\text{H}_2\text{O}$	55
4.7 FTIR Spectrum of $\text{NiV}_2\text{O}_6 \cdot 2\text{H}_2\text{O}$	60
4.8 TGA curve of $\text{NiV}_2\text{O}_6 \cdot 2\text{H}_2\text{O}$	61
4.9 DSC curve of $\text{NiV}_2\text{O}_6 \cdot 2\text{H}_2\text{O}$	62
5.1 Polyhedral Representation of the Central V_6O_{18} Band	73
5.2 The Raft-Like $\text{B}_{10}\text{O}_{16}\text{H}_4$ Polyborate Cap	75
5.3 $[\text{V}_6\text{B}_{20}\text{O}_{50}\text{H}_8]^{-10}$ Cluster	76

List of Figures (Continued)

Figure	Page
5.4. Hydrogen Bond between Cluster	77
5.5 Projection of Half Cluster on <i>bc</i> Plane	79
A.1 Space Group Table for <i>Pnma</i> (No. 62)	89
A.2 Space Group Table for <i>C2/c</i> (No. 15)	90

List of Symbols and Abbreviations

A, B	Values of $ F_{(hkl)} \cos \alpha$ and $f_j \sin \alpha$
A	A centered lattice
a, b, c	Unit cell vectors of the direct lattice
<i>a, b, c</i>	Unit cell axial lengths in direct space
a*, b*, c*	Unit cell vectors of the reciprocal lattice
<i>a*, b*, c*</i>	Unit cell axial lengths in reciprocal lattice
atm	atmosphere, unit of pressure
B	B centered lattice
B_{iso}	Isotropic vibration parameter
C	C centered lattice
d	Space between the lattice planes in crystal
F	F centered lattice
 F_o , F_c 	Amplitude of structure observed and calculate
F_(hkl)	The structure factor
f	Atomic scattering factor
<i>h, k, l</i>	Miller indices to identify a family of planes or a reflection
I	I centered lattice
P	Primitive lattice
psi	Pounds per square inch, unit of pressure
R	Primitive lattice for a rhombohedral crystal system
R_I	Conventional discrepancy index = $\frac{\sum (F_o - F_c)}{\sum F_o }$
$\langle u^2 \rangle$	Mean square amplitude of atomic vibration
2θ	Angle between incident and diffracted x-ray beams
α	Phase angle
<i>α, β, γ</i>	Angles between unit cell axis in direct space
<i>α*, β*, γ*</i>	Angles between unit cell axis in reciprocal space
λ	Wavelength of x-rays used in a given diffraction experiment
ρ or ρ_(xyz)	Electron density

Chapter I

Introduction

Molecule chemistry, and its impact on our daily lives, has been revolutionized since the middle of the nineteenth century by increased mastery in the formation of the covalent bond. Another evolution centered on noncovalent intermolecular forces has now begun. Organized species of higher complexity, often called supramolecular species, resulting from the association of two or more chemical species held together by intermolecular forces including hydrogen bonds and coordination bonds are being designed, synthesized and studied. (Dagani, 1998, Atwood, Davies, MacNicol & Vögtle, 1996).

Hydrogen bonded assemblies are built from molecular components that have hydrogen bond donor sites and hydrogen bond acceptor sites on different parts of the molecule binding to each other to form a larger structure. The criteria for classification of the intermolecular forces are distance-dependence and directionality. Hydrogen bonds of the types O–H···O and N–H···O may be termed strong or conventional hydrogen bonds (energies 20-40 kJ mol⁻¹). The distinctive geometrical attributes of strong hydrogen bonds, D–H···A–X (D = donor, A = acceptor, X = atom bonded to the acceptor), can be seen in the case of O–H···O bonds with typical H···A distances of 1.60-1.80 Å, D–H···A angles mostly in the range 150-160°, and H···A–X angles generally around 120-130°. This marked directionality of hydrogen bonds is well established and is the basis for efficient, reliable supramolecular construction using supramolecular synthons that contain groups such as –OH, or –CO₂H.

At the other end of the interaction spectrum are the weaker nondirectional forces including C–H···O, O–H···π, and C–H···π hydrogen bonding interactions (energies 2-20 kJ mol⁻¹), the strength and effectiveness of C–H···O hydrogen bond interactions depends on the C–H carbon acidity and on the oxygen atom basicity. A selection of supramolecular synthons are illustrated in Figure 1.1.

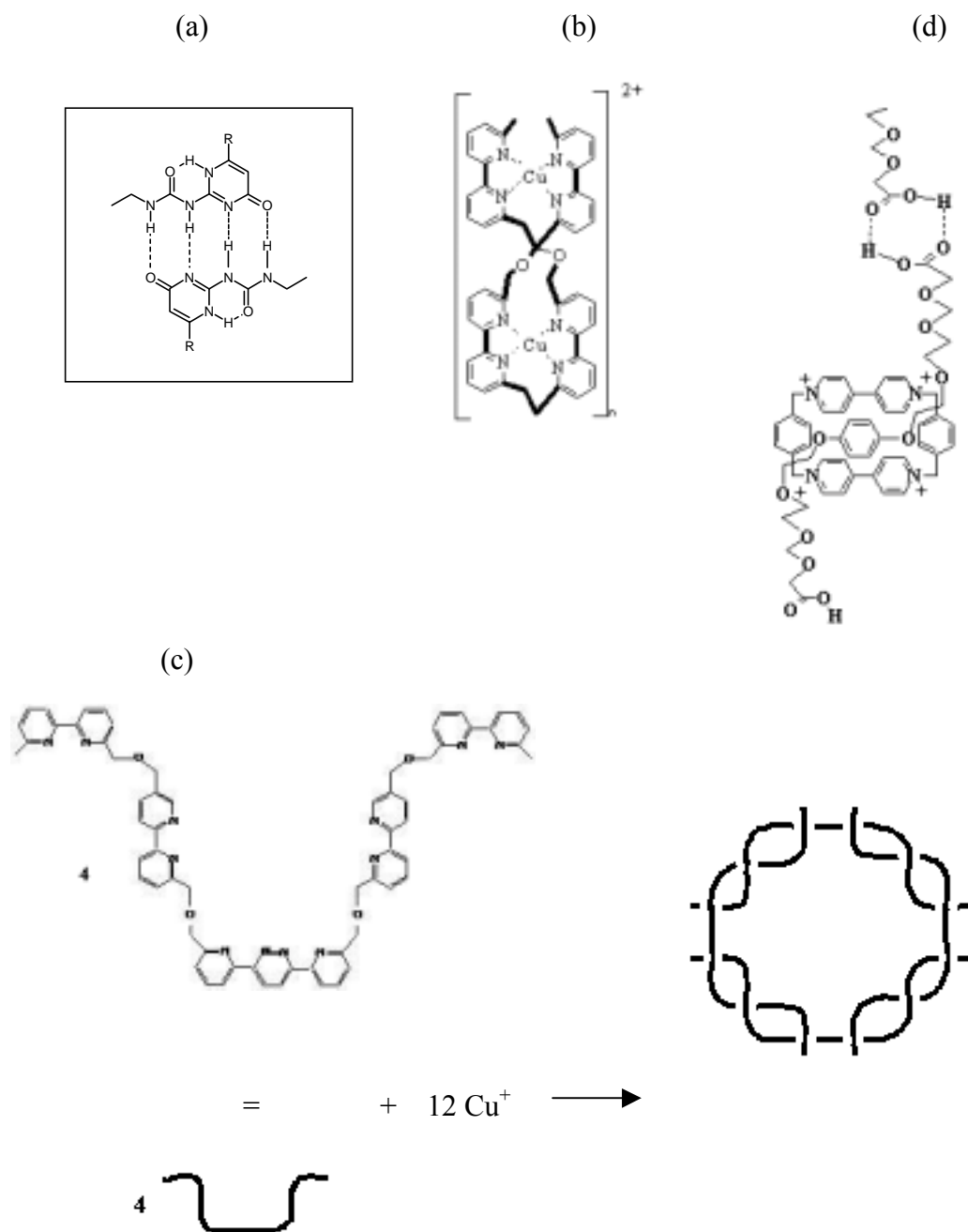


Figure 1.1. Selection of Supramolecular Synthons.

One recent example of a supramolecular structure is the three dimensional network hydrogen bonded polymer made by Sijbesma, Beijer, Brunsveld, Folmer, Hirschberg, Lange, Lowe & Meijer (1997). The monomer consists of a hydrocarbon chain terminated with 2-ureido-4-pyrimidone end groups which form polymeric

chains by hydrogen bonding as illustrated in Figure 1.1a. Each junction consists of two donors and two acceptors from each molecule complementing each other to form four hydrogen bonds. The hydrogen bond connection offers advantages over covalent three dimensional networks both at formation when the weaker hydrogen bonds can form, break, and re-form leading to fewer unreacted functional group defects, and again during use since, when a supramolecular polymer is put under strain, hydrogen bonds may temporarily break to release the strain, then re-form elsewhere in an unstrained arrangement (Dagani, 1997) by using the hydrogen bond functionality of the end groups in a reversible self-assembling polymer system, thereby maintaining the integrity of the material.

Metal atoms, and the coordination bonds they form (energies 85-335 kJ mol⁻¹) are a natural complement to hydrogen bonds in forming supramolecular structures. A wide variety of coordination geometries are available, depending on the metal and its oxidation state, giving many choices to the supramolecular architect. Thus, for example, by selecting suitable coordination geometry for each metal binding site a variety of double- and triple-helical complexes, including a complex in which two different strands form a double helix has been prepared. Schubert and Eisenbach (1999) built double helical complexes by using the well known specific self-assembly feature of the bis-bipyridine molecule in the presence of copper(I) ion (Figure 1.1b). The ligand incorporates two 2,2'-bipyridine binding sites separated by a methoxy-methylene spacer that sterically prevents the two metal binding sites from coordinating to a single metal center. Reaction of the ligand with octahedral metal ions which require three bidentate pyridyl-imine units to satisfy their coordinate requirement induces formation of a triple helical complex as in the case of the nickel complex (Hannon, Painting, Jackson, Hamblin & Errington, 1997). Another related complex uses a hybrid ligand with six binding sites complexed with copper(I) ions to form a macrocycle consisting of four ligand molecules and twelve Cu⁺ ions linked into double helical sections with twelve Cu⁺ crossing points as shown in Figure 1.1c. The central cavity of the wreath shaped macrocycle holds four PF₆⁻ anions (Funeriu, Lehn, Baum & Fenske, 1997).

Furthermore, workers in this field are seeking to understand the synthetic supramolecular chemistry that leads to self-assembly, the spontaneous generation of well defined supramolecular and molecular architectures from specifically engineered building blocks with preordained architecture using functional molecules (Desiraju,

1995; Dagani, 1998). One such example based on hydrogen bonds uses a dicarboxylic acid possessing a π -excessive hydroquinone ring which can thread through the macrocyclic cavity of a π -deficient tetracationic cyclophane to form a pseudorotaxane supramolecular structure stabilized by aryl-aryl face-to-face and edge-to-face interactions supplemented by C–H \cdots O hydrogen bonds and possessing pendent carboxyl groups for further noncovalent association as shown in Figure 1.1d (Fyfe & Stoddart, 1997). An example of the use of coordination bonds comes from Drain and coworkers (Drain, Nifiatis, Vasenko & Batteas, 1998) who designed a square array of nine porphyrins tethered together by twelve palladium ions into a structure (Figure 1.2) which with the correct ratio of the components is shaped like a four-pane-window five nanometers (50 Å) on a side. They have thus created a self assembling nanosieve built from three different kinds of porphyrin in a 1:4:4 ratio (a +-shaped coordination unit at the center of the array that coordinates to four metal ions, T-shaped coordination units that coordinate to three metal ions and form the sides of the array, and L-shaped coordination units that coordinate to two metal ions and form the corners of the array.)

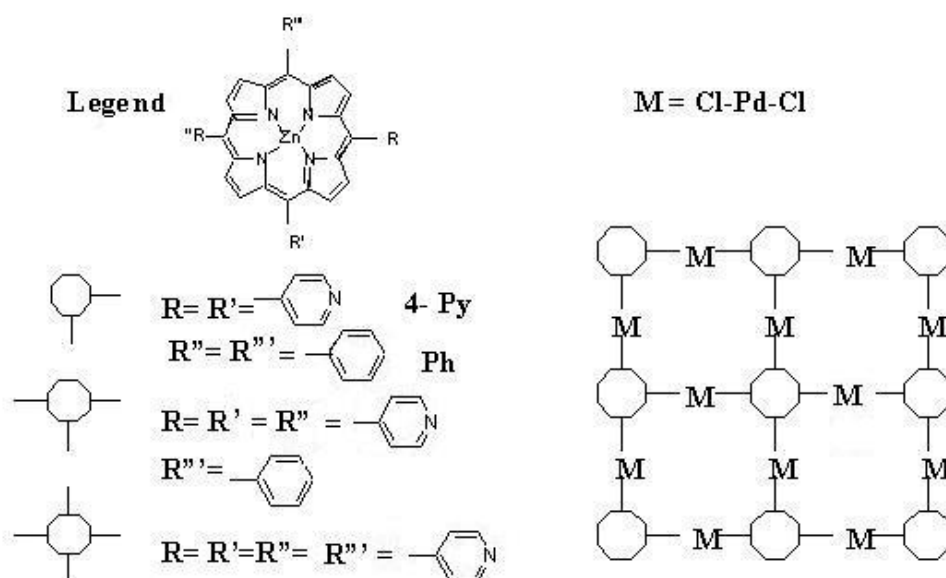


Figure 1.2. Nine Porphyrin and Twelve Palladium Moieties Assembled into a Nanosieve Array.

The solid materials with internal pore structures called molecular sieves have been extensively studied since the 1930s because of their applications as simple absorbers, ion-exchange materials, and catalysts. The selection of a proper sorbent useful for adsorption and separation purposes is based on a high equilibrium capacity and/or high selectivity. The capacity and selectivity are controlled by the pore volume, pore size distribution, surface area, and surface composition of the sorbent. The sorbent must have good kinetic properties for which control of crystal size, particle size, macroporosity, and binder type is essential; also good physical properties, manifested in a high bulk density, a high crush strength, and good erosion resistance of the sorbent; and finally good lifetime performance derived from high chemical, thermal, and mechanical stability. Classification of pore sizes and a list of selected important inorganic microporous materials are given in Table 1.1.

Table 1.1. Pore Size Classification and Important Porous Inorganic Materials.

Pore Size Range (Å)	Type	Materials	Pore Size Range (Å)
< 7	Ultramicropore	Zeolites	2-13
7-20	Micropore	Layered structures	2-100
20-500	Mesopore	Clays	
		Nonclay layer compound	
		Pillared layer compound	
> 500	Macropore	Gels and Colloids	20-500
		Composite materials	100-1,000

(Separation Technology, E. F. Vansant, 1994.)

Active search for such microporous materials with new architecture, pore chemistry, and composition has stimulated much recent interest in synthesis of mixed organic-inorganic materials, especially in the area of organo-templated synthesis of solid state inorganic materials (sometimes as inorganic structures containing weakly bound organic molecules and other times as coordinated molecules or even as ion pairs). Such organo-templated control of inorganic chain and layer aluminophosphate structures by amines (Williams, Gao, Chen, Ngai, Lin & Xu 1996) and diaminopropane (Gao, Li, Chen, Li, Xu & Williams, 1997) in low symmetry two dimensional AIPO networks were found to give similar $[Al_3P_4O_{16}]^{3-}$ layers separated

by organic cations but consequently connected in different manner to form interlayer rings consisting of four AlO_4 and six PO_4 tetrahedra or four AlO_4 and eight PO_4 tetrahedra, respectively.

Lewis and coworkers have presented a method for designing template molecules by computationally “growing” the template in the desired inorganic framework (Lewis, Willock, Catlow, Thomas & Hutchings, 1996). The efficacy of the template can be rationalized in terms of the energetics of the host-template interaction. Two complementary criteria which must be satisfied for an organic molecule to successfully template a zeolite have been identified from the calculated geometries of template-framework combinations of neutral moieties which are in agreement with the experimental structural data. First, the favorable nonbonding interaction between the template and the framework must be maximized. The packing energy, ΔE_{pack} , can be defined as

$$\Delta E_{\text{pack}} = (E_n / n) - E_1$$

where E_1 and E_n are the nonbonding energy of one and n template molecules in the host lattice, respectively. Second, molecular volume provides a good measure of template size with respect to the efficacy of the template to form a framework.

The framework structure is often stabilized by the template molecules. One such example is the new class of crystalline clathrates, porous supramolecular frameworks whose voids are filled with guest molecules, (Russell & Ward, 1997, Evans, Sukarto & Ward, 1999) that might have applications in the separation of fine chemicals, possibly even chiral separations. The absence of a template in the crystallizing gel leads to the formation of amorphous or dense materials under the same experimental conditions. In many systems the frameworks are not stable unless the guest molecules are in the voids.

One particular goal of current work is incorporation of active metals into the microporous phase to modify its catalytic behavior. Haushalter and Mundi (1992) reviewed the synthesis, structure, and properties of molybdenum phosphates from molecule to one dimensional polymer to two dimensional layer to three dimensional supramolecular microporous solid. The materials are synthesized in aqueous H_3PO_4 with cationic templates to guide the formation of the anionic metal oxide frameworks. They found it easy to incorporate cations into defect-free frameworks but had difficulty in removing the templates as the passages out of the pores are too small to

allow easy passage of hydrocarbon sized molecules. Thus, although these early materials were of limited catalytic utility, they demonstrated the ease of incorporating transition metals into framework materials and the large number of variables available to tune the synthetic process.

Feng, Bu and Stucky (1997) were interested in substituting aluminium in aluminophosphate with cobalt. An amine was chosen to be structure directing for the cobalt phosphate because it has strong attractive interaction, and the ligand-field stabilization energies for d^7 Co^{2+} disfavour the tetrahedral configuration relative to the octahedral configuration to a lesser extent than for most other d^n configurations.

Wang, Yu, Kumada and Kinomura (2000) utilized nonaqueous synthesis to form a layered zirconium phosphate templated with mixed organic ethylenediamine and inorganic ammonium cation. The two kinds of cation lie between the layers of zirconium phosphate. The ion exchange properties of this compound are worthy of investigation. Manganese phosphate templated by ethylenediamine has been prepared by hydrothermal synthesis. The result is another structure with cations located between inorganic sheets. The authors suggest the material may be useful for its magnetic properties (Fernández, Mesa, Pizarro, Lezama, Arriortua, Olazcuaga & Rojo, 2000).

Additional work to develop new phase type mixed transition metal phosphate frameworks, such as the hydrothermal synthesis of a cobalt molybdenum phosphate containing ethylenediammonium template ions, and a cobalt indium phosphate templated by ethylenediamine, have recently been reported (Lu, Xu, Goh & Chia, 1998). Another cobalt indium system formed with HF among the reactants has metal atoms in chains of alternating cobalt and indium atoms connected by bent fluoride bridges. The $(\text{CoO}_5\text{-F-InO}_5)$ chains are cross linked by hydrogen phosphate groups coordinated to the metals to form a two dimensional sheet structure (Yu, Sung & Williams, 1999). Other interesting new structures incorporate alkaline earth elements, $(\text{Sr}(\text{VO})_2)(\text{PO}_4)_2$ and $\text{Ca}(\text{VO})_2(\text{PO}_4)_2$ (Berrah, Leclaire, Borel, Guesden & Raveau, 1999) or mixed valency $(\text{V}_{0.94}\text{Co}_{0.46})[\text{PO}_4(\text{OH})_{0.74}(\text{OH}_2)_{0.26}]$ (Fur, Riou, Pena & Pivan, 2000).

Borate can be used in place of phosphate to form microporous transition metal borates as in the alkylamine templated oxovanadium borate cluster (Rijssenbeek, Rose, Haushalter & Zubieta, 1997), the transition metal main group oxide cluster in

the oxovanadium borate system, $(\text{H}_3\text{O})_{12}[(\text{VO})_{12}\{\text{B}_{16}\text{O}_{32}(\text{OH})_4\}]\cdot 0.48\text{H}_2\text{O}$ (Williams, Wu, Sung, Zhang & Yu, 1998), and the hydrothermally synthesized polyoxovanadium borate cluster, $\text{Rb}_4[(\text{VO})_6\{\text{B}_{10}\text{O}_{16}(\text{OH})\}]\cdot 0.5\text{H}_2\text{O}$ with quite unusual structure (Warren, Rijssenbeek, Rose, Haushalter & Zubieta, 1998).

Several of the materials mentioned above were prepared by hydrothermal synthesis, a particularly efficient technique for synthesis of solid phase supramolecular materials, especially framework/template materials, from mixtures of two or more solid components. In this technique the reaction takes place in superheated water in a closed reaction vessel. One important consequence of superheated water as the solvent is that the solubility of many species is considerably enhanced.

The physical properties of water are also strongly influenced by the increase in temperature and pressure. The density and dielectric constant of liquid water decrease as the temperature increases and increase as the pressure increases. The coefficient of self-diffusion increases and the viscosity decreases as the temperature increases. Thus, water mobility and reactivity are enhanced at high temperature and diffusion of dissolved species is faster at high temperature. These combined effects make it possible to carry out 'solid state' reactions at quite moderate temperatures in much shorter times than the previously used ceramic synthesis techniques. The mild conditions make it possible to include organic materials (mentioned above as templates for pores) which would decompose long before the reaction occurs in the traditional ceramic synthesis methods.

A closely related synthesis technique is solvothermal synthesis where the water is replaced by nonaqueous solvent. Similar alterations of solubilities and physical properties occurs, and again reactions that would have previously been impossible to conduct or that would have required high temperature can be done under mild conditions in relatively short times.

The compounds reported in this thesis all contain vanadium. Vanadium is widely distributed in nature, having been identified in the sun, stars, and meteorites, and in low concentration in many plants and animals. It forms up to 0.05% of the earth's crust and there are 158 vanadium containing minerals in the mineralogy database. The chief sources of the metal are patronite (VS_3 - VS_6 polysulfide), roscoelite (V containing mica) and mottramite $\{(\text{Pb}, \text{Ca}, \text{Cu})_3(\text{VO}_4)_2\}$. More recently,

vanadium has also been produced as a byproduct of uranium production which uses carnotite ores, $\{[K_2(UO_2)_2(VO_4)_2] \cdot 3H_2O\}$, as a source of uranium (Page & Wass, 1997). The situation is similar in Thailand; vanadium is not found pure in nature but exists in minerals, and while not investigated in detail, the Thai Mineral Resources Department has found low concentrations of vanadium in uranium containing minerals.

Chirayil, Zavalij and Whittingham (1998) used hydrothermal synthesis with organic species or simple cations such as alkali or alkaline earth elements as structure directing groups along with pH control to prepare many new vanadium oxide phase types. Zavalij and Whittingham (1999) offered a crystal chemical and topographical analysis of vanadium oxides with open structure. The frameworks were proposed based on the scheme: polyhedra to chain to layer to three dimensional framework. They and others have been interested in vanadium transition element compounds because of the variety of vanadium oxidation states and their redox properties which readily allow the insertion or removal of small ions such as lithium; such materials may be useful for secondary cathode materials in advanced lithium batteries (Broussely, Biensan & Simon, 1999).

Schindler, Hawthorne and Baur (2000) studied relationships among vanadium oxidation state, geometry, and bond distance using the available structural data for well-refined vanadium phosphates, synthetic vanadates, and mineral vanadates. In minerals vanadium is most often found in the +3, +4, and +5 oxidation states. The oxidation state correlates with the coordination polyhedron type, varying from tetrahedral through trigonal bipyramid and square pyramid to octahedral as the oxidation state decreases from +5 to +3 as shown in Table 1.2. Inorganic frameworks have five coordinate vanadium in square pyramidal only, except some cases of mixed-metal frameworks which have trigonal bipyramid polyhedra (Shiro & Fernando, 1971). Vanadium's neighbors in the periodic table Ti, Cr, and Mn are most commonly found with more restricted ranges of oxidation states, +4 and +3, +3 and +6, and +2, +4 and +7, respectively. Similarly, their typical coordination is restricted to octahedral for Ti, Cr, and Mn in oxidation state +4 or less and tetrahedral for Cr and Mn in higher oxidation states.

The bond length distribution in VO_n polyhedra show distinct populations which can be used to define vanadyl groups, V-O bonds *trans* to vanadyl groups, and

V-O bonds not *trans* to vanadyl groups (sometimes called equatorial V-O bonds). The distribution of bond lengths in V-O_n polyhedra is shown in Table 1.3.

Table 1.2. Metamorphosis of the Vanadium Coordination Polyhedra.

Oxidation State	Coordination Number	Geometry
V ³⁺	6	octahedral
V ⁴⁺	6	octahedral
	5	trigonal bipyramidal & square pyramidal
V ⁵⁺	4	tetrahedral

Table 1.3 Bond Lengths in V-O_n Polyhedra.

Kind of Polyhedra	Bond *	Average Length (Å)
Octahedral, overall mean	V ³⁺ -O _{all}	2.01(5)
Square pyramidal [1+4]	V ⁴⁺ -O _V	1.59(2)
	V ⁴⁺ -O _E	1.98(4)
	overall mean	V ⁴⁺ -O _{all}
Octahedral [1+4+1]	V ⁴⁺ -O _V	1.60(4)
	V ⁴⁺ -O _E	2.00(5)
	V ⁴⁺ -O _T	2.27(12)
	overall mean	V ⁴⁺ -O _{all}
Square pyramidal [1+4]	V ⁵⁺ -O _V	1.59(3)
	V ⁵⁺ -O _E	1.89(6)
	overall mean	V ⁵⁺ -O _{all}
Octahedral [1+4+1]	V ⁵⁺ -O _V	1.61(3)
	V ⁵⁺ -O _E	1.92(9)
	V ⁵⁺ -O _T	2.31(8)
	overall mean	V ⁵⁺ -O _{all}
Polyhedral [2+3]	V ⁵⁺ -O _V	1.66(4)
	V ⁵⁺ -O _E	1.95(8)
	overall mean	V ⁵⁺ -O _{all}
Octahedral [2+2+2]	V ⁵⁺ -O _V	1.67(4)
	V ⁵⁺ -O _E	1.93(6)
	V ⁵⁺ -O _T	2.20(14)
	overall mean	V ⁵⁺ -O _{all}

* V-O_V = vanadyl bond; V-O_E = equatorial bond; V-O_T = *trans* bond

As the synthesis of compounds containing vanadium increased dramatically exotic new structure types were discovered. These include a vanadium phosphate double helix (Soghomonian, Chen, Haushalter, Zubieta & O'Connor, 1993) and a microporous vanadium phosphate with a V_5O_9 group in the shape of a spiked helmet (Khan, Meyer, Haushalter, Schweitzer, Zubieta & Dye, 1996), as well as the mixed valance super Keggin ion polyoxovanadate cluster, $[V_{18}O_{42}(PO_4)]^{11-}$ and the doughnut shaped $[V_{12}B_{32}O_{84}Na_4]^{15-}$ anions. In the latter the cavity produced by the cyclic $[V_{12}B_{32}O_{84}]^{19-}$ anion is occupied by a tetragonal moiety made up of four Na^+ ions. The complex shows antiferromagnetic interaction in terms of the nearest $V \cdots V$ distances in the anion (Yamase, Suzuki & Ohtaka, 1997).

A new family of porous mixed metal oxide, manganese vanadates has been formed which is stable to loss of water and offers the prospect of engineering either novel porous phases or compounds of magnetic interest (Williams, Law, Sung, Wen & Zhang, 2000). Many open inorganic frameworks in which the channel content is an integral part of the crystal structure such that it is not possible to remove the content of channel without loss of crystallinity and collapse of the framework have been prepared. This is a common problem that will no doubt be overcome by more subtle chemical treatments.

Another recent development is the vanadium redox battery which has been proposed for large scale load leveling applications. The vanadium redox battery stores energy by employing a vanadium redox couple (V^{2+}/V^{3+} in the negative half cell and V^{4+}/V^{5+} in the positive half cell) with the vanadium ions stored in mild sulfuric acid electrolyte solutions. During the reversible charge/discharge cycle, hydronium ions are exchanged between the two electrolyte tanks through a polymer membrane that is permeable to hydronium ions. During discharge, as positive hydronium ions flow through the membrane, electrons flow in the external circuit of the battery producing about 1.4-1.6 volts. The net efficiency of this battery can be as high as 85%. Like other flow batteries, the power and energy rating of the vanadium redox battery are independent of each other. It is expected that the vanadium redox battery will be a low cost method of providing cleaner peak power demands. A diagram of a vanadium redox battery is shown in Figure 1.3 (Skylas-Kazacos & Robins, 1988).

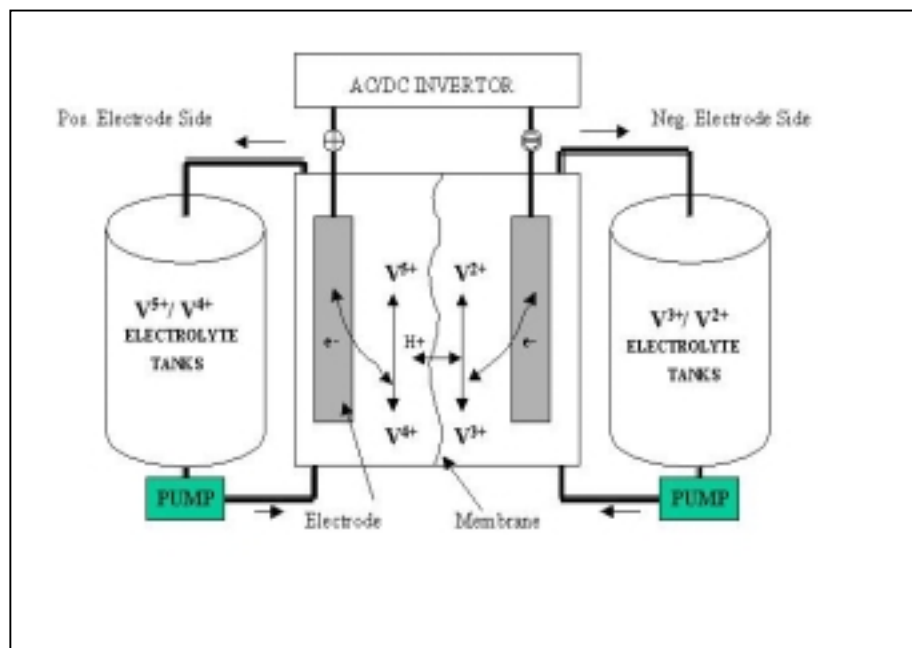
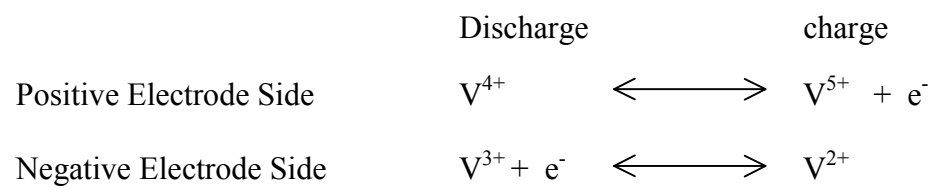


Figure 1.3. Diagram of Vanadium Redox Battery.



Chapter II

Theory of Single Crystal X-ray Diffraction

2.1 Introduction

Objects of macroscopic size are visible to us because they scatter light falling on them and our eye lens can recombine the individual rays into an image on the retina. For smaller objects magnification by a powerful microscope lens can help to produce a large enough image on the retina that they are visible to us. For objects smaller than visible light wavelengths (400–700 nm) shorter wavelengths must be used to “see” the object. Thus, to observe objects of molecular dimensions light with wavelengths on the order of Ångstroms, *i.e.* hard x-rays, must be used.

However, x-rays cannot be used in the same way as visible radiation. The physical property that makes the optical lens possible is refractive index, often described as the ability of a material to “bend” light rays, as for example the apparent bending of a stick at the point where it enters water when placed in water at an angle. While it is easy to find a material with a relatively large index of refraction for wavelengths in the visible light region the situation is quite different for hard x-rays; even high density materials have indices of refraction that differ from unity on the order of 10^{-4} - 10^{-5} for hard x-ray wavelengths. Thus, there is no suitable material for a lens to focus x-rays. Many elementary textbooks suggest an analogy. X-rays interact by being scattered by the electrons in matter. The scattered rays then interact to form an interference pattern. An x-ray diffractometer can record the intensity maxima of the scattered x-ray interference pattern produced from a single crystal, and sophisticated calculations can be carried out to create a model consistent with the observed intensity pattern. Thus, similar to the lens for visible light, the computer and its software can act as a lens carrying out the recombination of the scattered x-ray radiation to form an image of the molecule.

2.2 Source of X-rays

The standard laboratory source of x-rays is the sealed x-ray tube illustrated schematically in Figure 2.1. The tube is an evacuated enclosure of glass or ceramic

and metal construction, which includes a tungsten filament through which an electric current can be passed to provide a source of electrons which are accelerated towards a metal anode by an accelerating voltage applied between the filament and the anode. The electrons collide with the anode and are either decelerated producing Bremsstrahlung radiation, or collide with electrons in the anode atoms ejecting them from their orbitals.

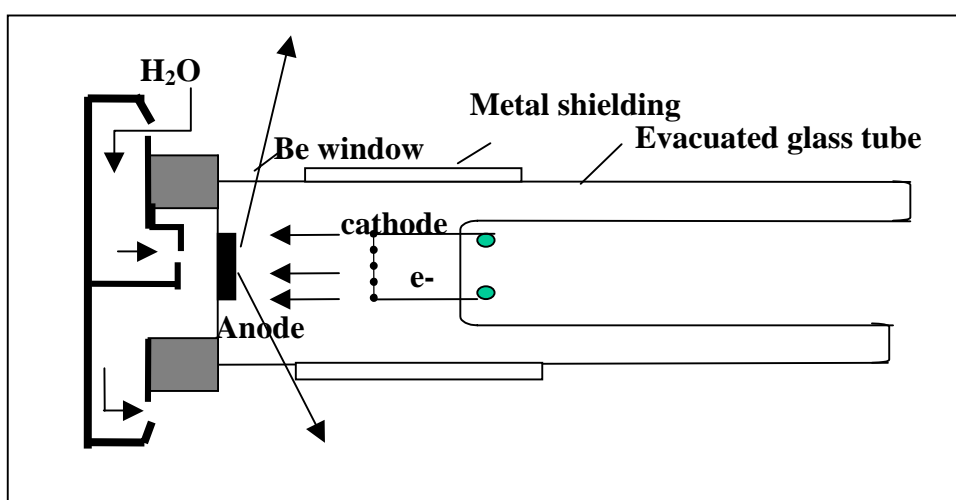


Figure 2.1. Schematic Diagram of an X-ray Tube.

At low accelerating voltage an electron collision with the anode results only in deceleration and a continuum of radiation is produced. As the accelerating voltage is increased the wavelength cutoff also increases. When the accelerating voltage reaches the critical target energy the second process also occurs and the output radiation then consists of a series of intense sharp maximum superimposed on the broad-spectrum continuum background as shown in Figure 2.2. The sharp peaks are the result of an electron from a higher orbital falling into the lower energy space, and in the process emitting a single photon corresponding to the energy difference between the two orbitals. If the ejected electron is from a $1s$ orbital and an electron from a $2s$ orbital takes its place the resulting x-ray photon will be a hard x-ray with a wavelength on the order of Ångstroms. Thus, the positions of the sharp peaks are characteristic for each target as is the minimum accelerating voltage required to produce the characteristic

peaks. For a typical laboratory x-ray source an accelerating voltage of about 40,000-60,000 volts between the filament and the anode is used.

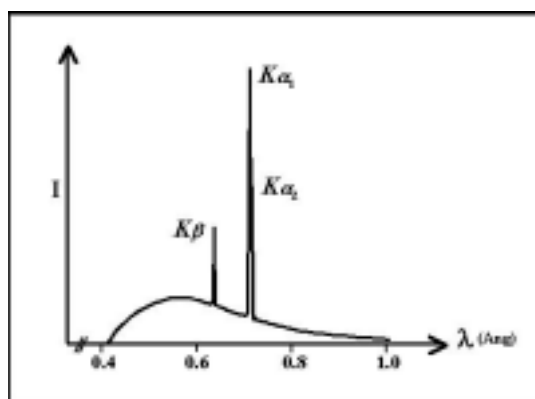


Figure 2.2. X-ray Spectra with Characteristic Peaks.

When the x-ray photon is emitted it is equally probable that it go in any direction. Thus, more than half the photons produced are reabsorbed in the anode itself. The x-ray beam to be used for the experiment is taken from the tube through thin beryllium or aluminum foil windows as shown above. As a typical x-ray beam aperture is on the order of one mm^2 located at least 25-30 mm from the anode, only a small fraction of one percent of the x-rays produced are actually used in the traditional x-ray diffraction experiment.

The anode is heated by the reabsorbed x-ray photons noted above, as well as by the transfer of energy from the colliding high energy electrons from the cathode. Approximately 1% of the incident energy becomes x-rays, while the other 99% is changed to heat energy. The limit on the power that can be applied to an x-ray tube is determined by how quickly this energy can be transferred away from the anode. Cooling is usually by chilled water circulated through the back side of the anode, and the practical power limit for an anode made from copper with a collision site of 1×10 mm is about 3000 watts.

The radiation used for normal single crystal x-ray diffraction work should be monochromatic and of high intensity. Both the Bruker Analytical X-ray System's and the B. V. Nonius' diffractometers employed in this study used a pyrolytic graphite crystal monochromator to select the K_{α} portion of the diffracted x-ray beam into the

collimator port. The monochromator design and position relative to the anode eliminates most of the Bremstrahlung radiation and allows only a limited angular range of x-rays including the strong and sharp K_{α} and K_{β} peaks for the common anode materials to make direct contact with the graphite crystal.

2.3 Crystalline State

The defining characteristic of the crystalline state is a very high degree of internal order made up of the repetition of a structural unit by translation in three dimensions to form crystals. A crystal lattice is a three dimensional array of points in which the environment of each point is identical. The convolution of this lattice with a structure motif gives three dimensional solid crystal structure. The imaginary parallelepiped that contains one unit of the translationally repeating pattern is termed the unit cell. The conventional unit cell has the shortest possible sides, generally with $a \leq b$ and interaxial angles as close as possible to 90° while including the full symmetry of the three dimensional arrangement. A two dimensional example of a lattice using a flower as the repeating motif is shown in Figure 2.3a.

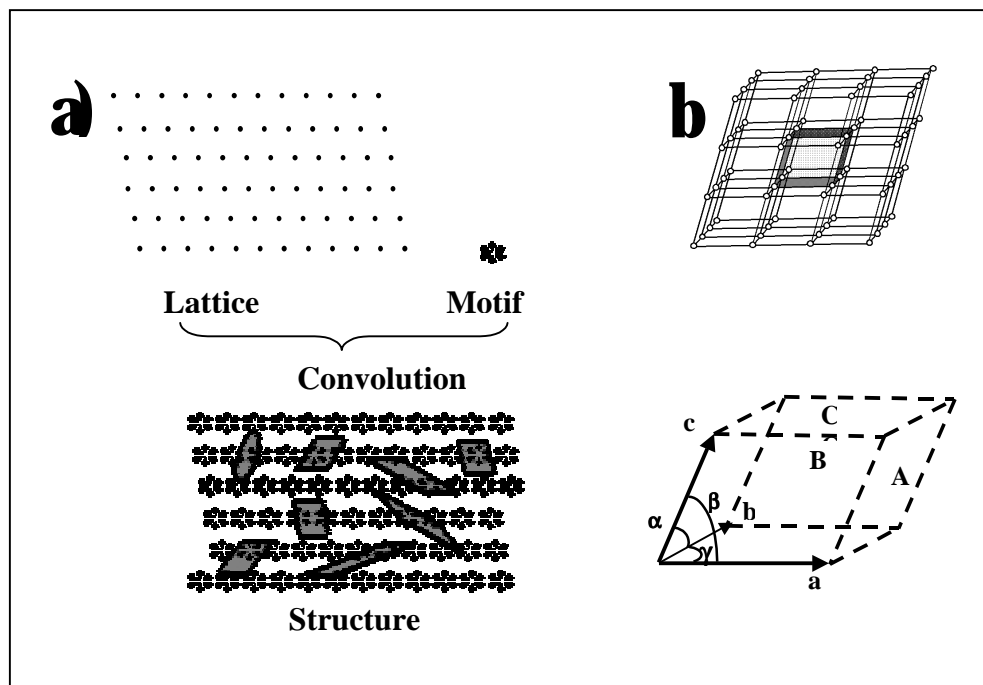


Figure 2.3. Unit Cells and Lattices. a) Two dimensional. b) Three dimensional unit cell and lattice.

Figure 2.3b illustrates a three dimensional lattice of unit cells and a single unit cell showing the unit vectors **a**, **b**, and **c** corresponding to the x, y, and z crystallographic axes. The angles between them are indicated by α , β , and γ with α being the angle between **b** and **c**, β the angle between **a** and **c**, and γ the angle between **a** and **b**. The magnitudes of **a**, **b**, and **c**, indicated by *a*, *b*, and *c*, are the lengths of the translation repeats.

Crystallographic Planes and Miller Indices

Crystallography, before the discovery of x-rays, was largely concerned with the description of crystal forms and the use of crystal habit to identify materials. The individual faces bounding a crystal can be assigned indices that relate back to the unit cell of the crystal. Each face can be considered to represent a family of parallel planes existing in the extended crystal lattice. The family of parallel planes can be defined by the number of times each unit cell axes is cut by intersection of planes from that family in going from 0 to 1 in each axial direction (or the equivalent alternative, the reciprocal of the fraction of the axes one must move to go from one plane in the family to the adjacent planes in the same family). The three integers obtained by either of these methods are called the Miller indices and are designated by *h*, *k*, and *l* for the index related to the **a**, **b**, and **c** axes, respectively.

The Seven Crystal Systems

Early crystallographers noticed that well-formed crystals generally exhibited symmetrical relationships between their faces, and sometimes special relationships between the unit cell parameters. Based on these they were able to divide crystals into seven classes characterized by the relationships between unit cell edges and unit cell angles as summarized in Table 2.1. The lattices for each of the crystal systems thus defined by the metrical relationships between the unit cell parameters has a characteristic symmetry also given in Table 2.1. The lattice points defining a unit cell are equally distributed about the point in the center of the unit cell since the point midway between two adjacent lattice points in any direction relates them by an inversion center. Thus the lattice symmetry for each crystal system is inherently centrosymmetric.

Table 2.1. Crystal Systems.

Crystal System	Parameter	Lattice Symmetry
Triclinic	$a \neq b \neq c; \alpha \neq \beta \neq \gamma$	$\bar{1}$
Monoclinic	$a \neq b \neq c; \alpha = \gamma = 90^\circ, \beta > 90^\circ$	2/m
Orthorhombic	$a \neq b \neq c; \alpha = \beta = \gamma = 90^\circ$	mmm
Tetragonal	$a = b \neq c; \alpha = \beta = \gamma = 90^\circ$	4/mmm
Trigonal/Rhombohedral	$a = b = c; \alpha = \beta = \gamma \neq 90^\circ$	$\bar{3}m$
Hexagonal	$a = b \neq c; \alpha = \beta = 90^\circ; \gamma = 120^\circ$	6/mmm
Cubic	$a = b = c; \alpha = \beta = \gamma = 90^\circ$	m $\bar{3}$ m

Bravais Lattices, Point Groups, and Space Groups

The simplest lattice in each of the crystal systems has lattice points only at the corners of the unit cell, that is the equivalent of one lattice point per unit cell. Such lattices are termed primitive and are designated by the letter P (except rhombohedral where R is used). The seven types of primitive crystal systems can be described using only the lattice metrics. The conventional crystallographic unit cell requires another consideration. The conventional cell, as noted above, also includes the full symmetry of the three dimensional arrangement, which gives rise to seven additional unique lattice systems which require more than one lattice point per unit cell.

The nonprimitive lattices are those with a pair of lattice points centered on opposite faces of the unit cell, designated A , B or C depending (see Figure 2.3b) on whether the added lattice points are on the bc , ac or ab faces respectively, those with an additional lattice point located at the body center of the unit cell, designated I ; and those with lattice points centered on all faces of the cell, designated F . The fourteen unique primitive and centered lattices, called the Bravais lattices, are illustrated in Figure 2.4. It may appear that there should be more centered cells, however, inspection will show that a metric transformation can convert any other centered cell to one of those given. A projection example is given in Figure 2.5 for tetragonal lattices (two sides of the cell have equal length) where P , I , C , and F lattices are outlined. The different centering patterns can be seen to be transformable to tetragonal P and I lattices.

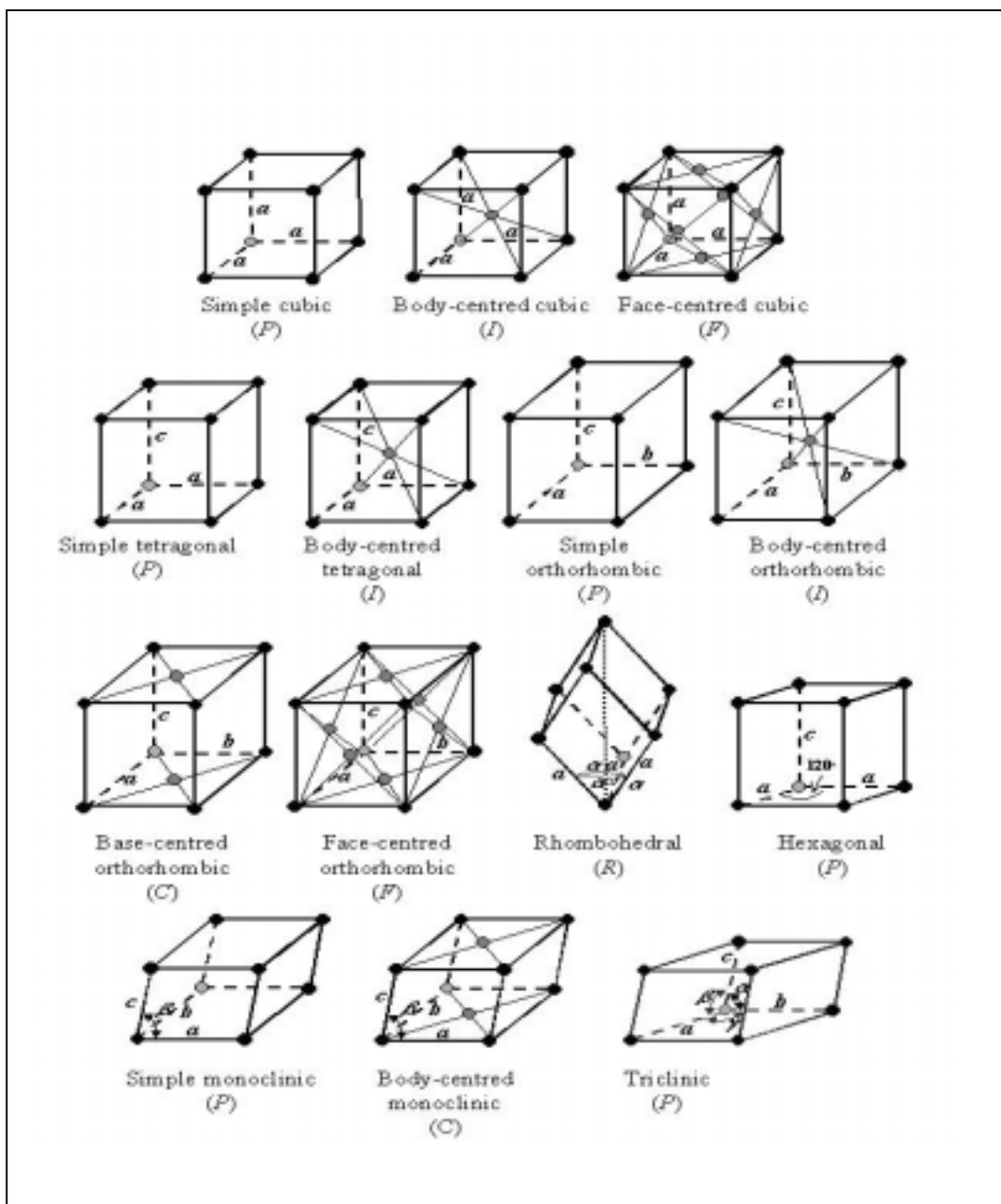


Figure 2.4. The Bravais Lattices.

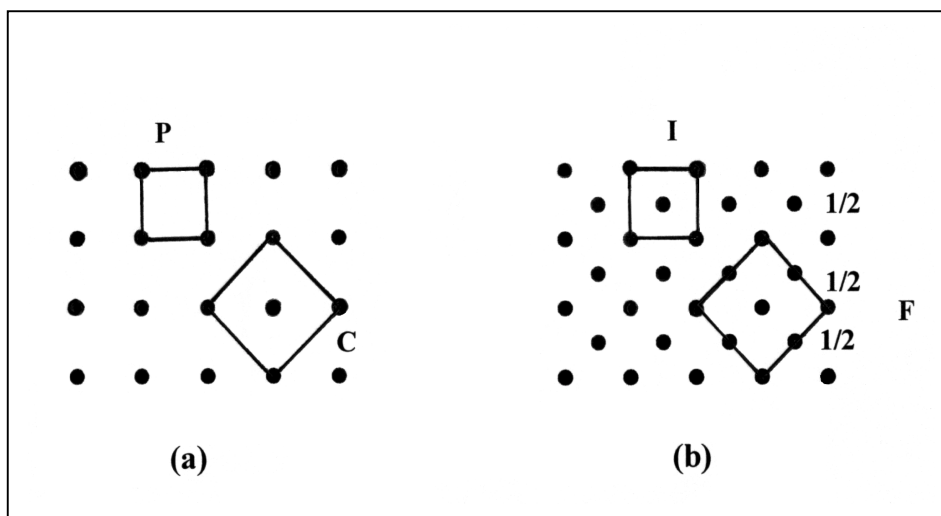


Figure 2.5. Tetragonal Lattices Illustrating Cell Centering. a) *P* lattice and *C* centered lattice that can be metrically reduced to the *P* lattice. b) *I* and *F* centered lattices. The *F* lattice can be metrically reduced to the *I* lattice.

If the faces of a crystal are considered as planes defining an idealized solid figure and they are related by the symmetry operations that can act about a point (*i.e.* rotation axes, mirrors, center of symmetry, and rotary-inversion axes), crystals can be classified in terms of the group symmetry operations relating their faces in just 32 ways or as 32 crystallographic point groups. The 32 point groups include both centrosymmetric and noncentrosymmetric groups, but x-ray diffraction patterns, to a first approximation, are always centrosymmetric. Adding an inversion center to the symmetry elements actually present for each of the noncentrosymmetric groups, then classifying the 32 point groups by the resulting eleven classes gives what are known as the eleven Laue groups.

The conventional crystallographic unit cell defined above is the smallest unit of the translationally repeating pattern containing the full symmetry of the crystal. Thus, there may be multiple identical subunits of structure within the unit cell related to one another by symmetry elements. The smallest unique subunit of structure is called the asymmetric unit. The combination of the Bravais lattices with the patterns of symmetry relationships between the asymmetric units consistent with the lattice symmetries, provides the simplest description of the total structure.

The symmetry operations combine according to the rules of group theory, sometimes giving additional symmetry operations, for example if a mirror operation is added perpendicular to an existing 2-fold operation two new asymmetric units are

created. As illustrated in Figure 2.6, the asymmetric unit, represented by a comma, at position **1** is rotationally related to the second asymmetric unit, represented by a backwards comma, by rotation of the asymmetric unit at position **1** by 180° about the z axis to position **2**. Addition of the mirror plane perpendicular to the 2-fold axis transforms the asymmetric unit created by the rotation at position **2** into the third asymmetric unit, represented by an inverted comma at position **3**. The two units, **1** and **3** are related by an inversion operation through the point of intersection of the 2-fold axis and the mirror plane. Thus, a 2-fold operation followed by a perpendicular mirror operation generates an inversion operation. The asymmetric unit at position 4, represented by an inverted backwards comma, can be generated from the asymmetric unit at position 1, 2, or 3 by reflection, inversion, or rotation, respectively.

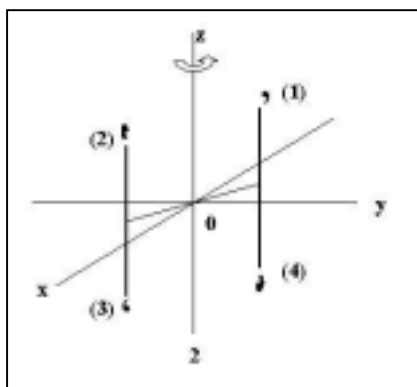


Figure 2.6. Reflection Combined with Two-fold Rotation.

In addition to the centering operations and the point symmetry operations discussed above, there are two additional symmetry operations (called space symmetry operations since they cannot act through a single point) that can relate asymmetric units within the unit cell. One space symmetry operator combines translation with rotation (called a screw axis) and the other combines translation with reflection (called a glide plane). When all of the point symmetry operations, the space symmetry operations, and the Bravais lattices are combined only 230 unique three dimensional combinations (groups) result. These 230 combinations are the total number of ways atoms and molecules can be arranged to make a crystal. They are the 230 space groups and can be found listed in the International Tables for Crystallography (Hahn, 1992).

2.4. Diffraction and the Bragg Equation

The diffraction of x-rays by crystals was discovered by Max von Laue and Friedrich Knipping in 1912 and described in terms of diffraction from a three dimensional grating. In the same year W. L. Bragg with his father noticed that the diffracted beams behaved as if they were reflected from planes passing through points of the crystal lattice, similar to optical reflection. They derived the simple equation, now known as Bragg's Law by considering an x-ray beam (represented in Figure 2.7 by the two rays **1** and **2**) incident on a pair of parallel planes **P1** and **P2** with angle θ . Electrons assumed at **O** and **C** will be forced to vibrate by the oscillating field of incident beam, and as vibrating charges they will emit electromagnetic radiation in all directions. Secondary rays **1'** and **2'**, resulting from constructive interference, will emerge as though they are reflected from the planes at angle θ .

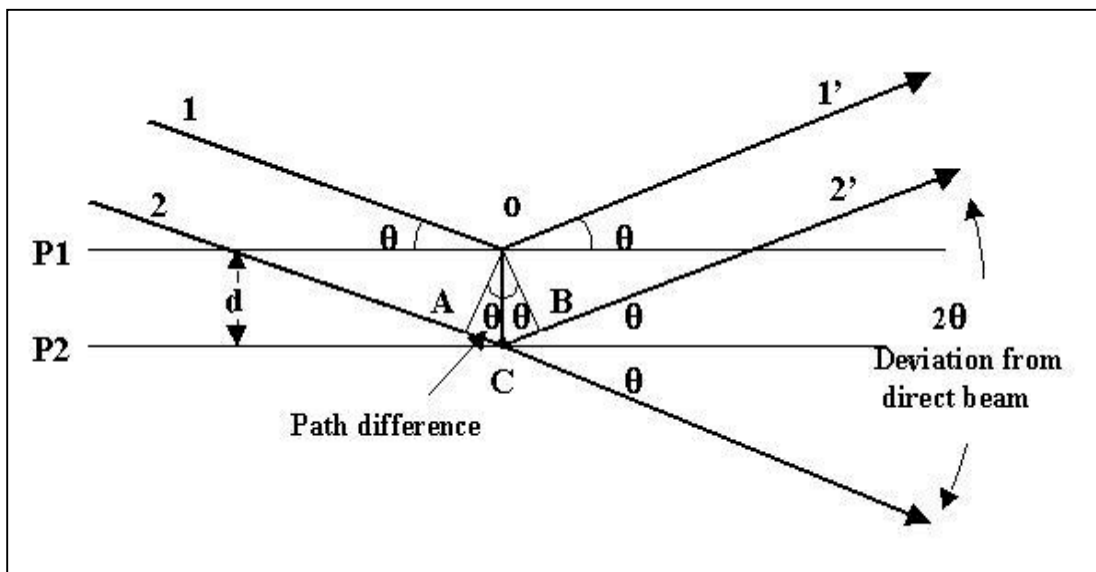


Figure 2.7. Reflection of an X-ray Beam.

A diffracted beam will result if the secondary waves represented are in phase. Thus $\angle AOC = \angle BOC = \theta$ and $AC = CB$ and the **1'** and **2'** rays are in phase, *i.e.* crest to crest, when the path difference between the two rays is an integral number of wavelengths, $AC + CB = 2AC = n\lambda$, n an integer. From the rule for sine in a right triangle, $AC/d = \sin \theta$, thus $AC = d \sin \theta$, $\therefore 2d \sin \theta = n\lambda$, which is Bragg's law for x-ray scattering from a set of parallel crystal planes.

2.5 Diffraction by Atoms or Groups of Atoms in Crystals

As noted in section 2.1, the diffraction intensity pattern results from the scattering of x-rays by an object. In crystallography the object is a crystal made up of a periodic array of atoms. The atomic electrons act as secondary sources of x-rays, scattering them in all directions. Due to the periodic nature of the crystal the diffraction pattern produced is also periodic and each diffraction maximum has a particular combination of amplitude and phase. As can be seen from the Bragg's Law equation as the distance between planes in the lattice increases the distance between the resulting diffraction points decreases, leading to the terms real space and reciprocal space for the crystal lattice and the diffracted intensity pattern, respectively. The relationship between the real lattice and the reciprocal lattice is shown in Figure 2.8.

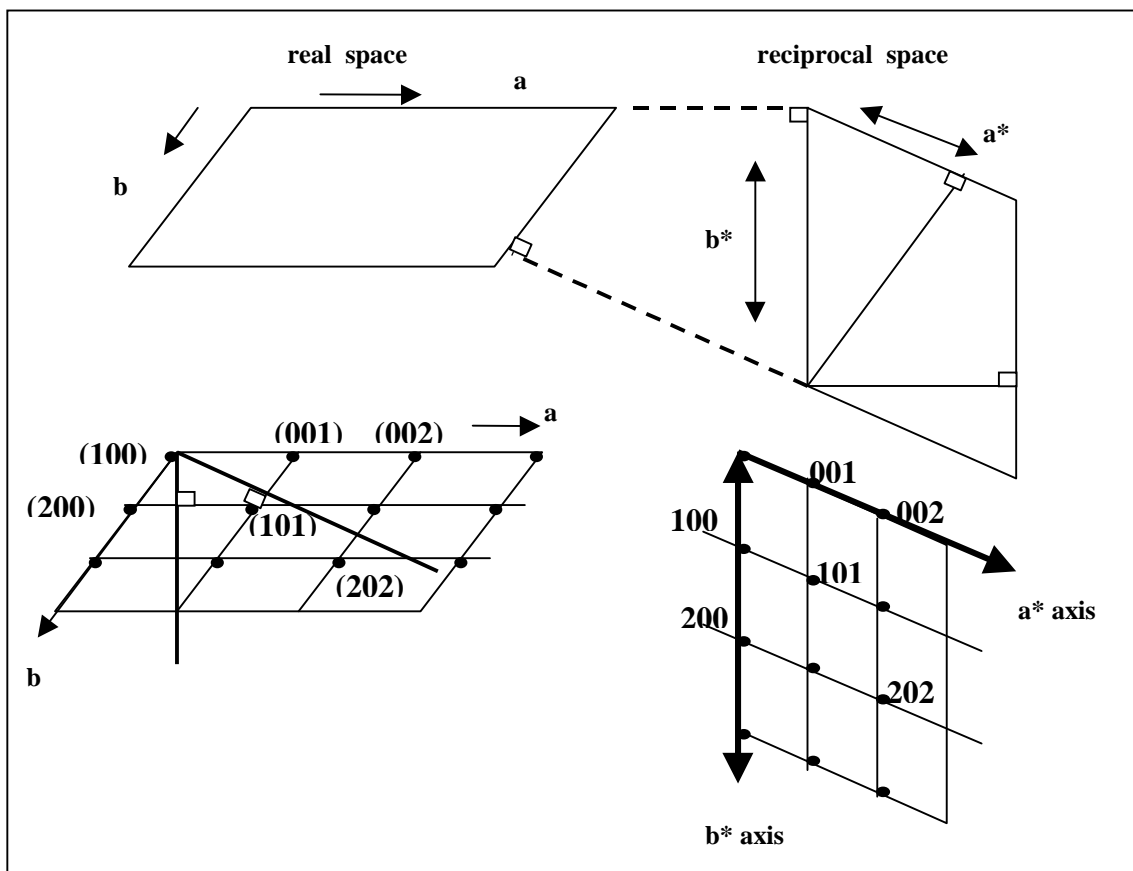


Figure 2.8. The Relationship between Real and Reciprocal Lattices.

The reciprocal lattice parameters (a^* , b^* , c^* , α^* , β^* , γ^* , and V^*) are related to the direct lattice parameters as follows:

$$a^* = bc \sin \alpha / V, \quad b^* = ac \sin \beta / V, \quad c^* = ab \sin \gamma / V \quad \text{where } V^* = 1/V$$

$$\cos \alpha^* = (\cos \beta \cos \gamma - \cos \alpha) / \sin \beta \sin \gamma$$

$$\cos \beta^* = (\cos \alpha \cos \gamma - \cos \beta) / \sin \alpha \sin \gamma$$

$$\cos \gamma^* = (\cos \alpha \cos \beta - \cos \gamma) / \sin \alpha \sin \beta$$

2.6 Structure Factor and Electron Density

The amplitude of scattering for a stationary atom, expressed relative to the scattering power of a free electron, is normalized to the number of electrons in the atom at $\sin \theta / \lambda = 0.0$. The scattering falls off with increasing scattering angle or increasing values of $\sin \theta / \lambda$ as indicated in Figure 2.9. If the electrons were all located at a point the intensity would not fall-off. However, the electrons are distributed in a nonpoint volume and the scattered intensity as a function of $\sin \theta / \lambda$ falls off rapidly. The curve of the scattering intensity as a function of $\sin \theta / \lambda$ is called the atomic scattering factor and is usually designated by f .

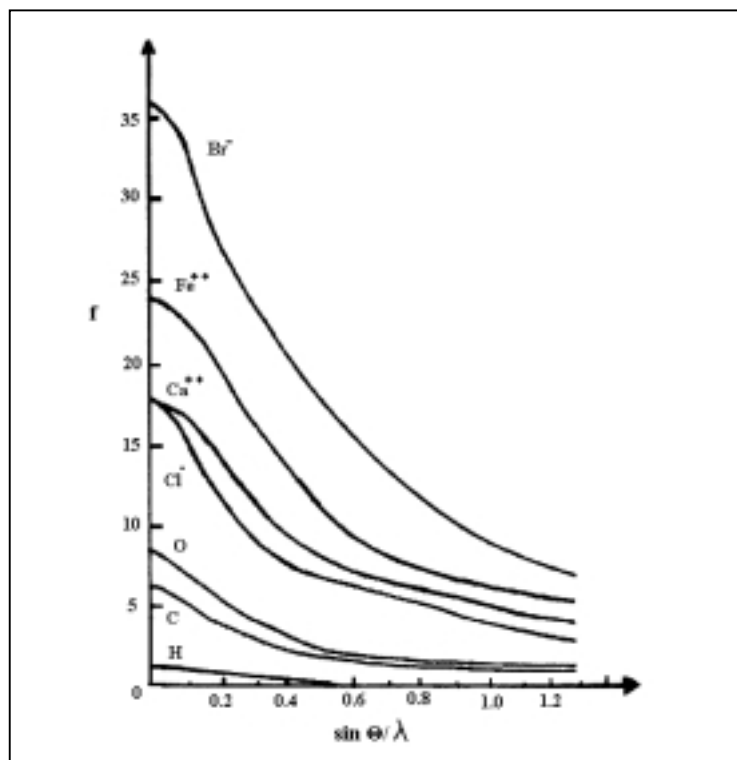


Figure 2.9. Atomic Scattering Factor Curves.

Real atoms are not stationary. They have vibrational motion that is dependent on the temperature, and at zero scattering angle ($\theta = 0^\circ$) the real intensity of scattering will be reduced from the number of electrons in the atom due to this motion. The reduction in intensity relates to temperature, and can be expressed in terms of an angle dependent exponential expression which includes a thermal factor, B . The reduction in intensity of the scattering is described by the following equation:

$$f_B = f e^{-B(\sin\theta/\lambda)^2}$$

The B -factor can be related to the mean displacement, $\langle u \rangle$, of a vibrating atom, or to the more commonly reported $U = \langle u \rangle^2$ by

$$B = 8\pi^2 \langle u \rangle^2 = 8\pi^2 U$$

In most structures of interest the scattering is not by single atoms, but by the group of atoms making up the asymmetric unit. The x-radiation scattered by the repeating unit cell in any direction is the sum of the magnitudes of the diffractive distribution from all the individual atoms to give the amplitude of the scattered wave $|F_{(hkl)}|$ as illustrated in Figure 2.10. The resultant $F_{(hkl)}$ is called the structure factor. The cosine and sine terms in the A and B parts, respectively, emphasize the periodic nature of the phenomena.

$$|F_{(hkl)}| = (A^2 + B^2)^{1/2}, \text{ where}$$

$$A_{(hkl)} = \sum_j f_j \cos \alpha_j$$

$$B_{(hkl)} = \sum_j f_j \sin \alpha_j$$

$$\alpha_j = \tan^{-1} \frac{f_j \sin \alpha_j}{f_j \cos \alpha_j}$$

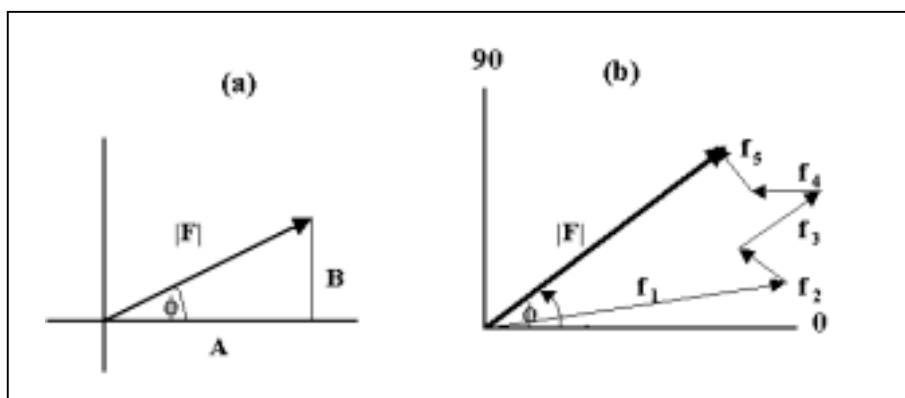


Figure 2.10. Vector Representation of the Structure Factor.

A and B can be viewed as the projections of F on the axes of a Cartesian coordinate system and the structure factor can be written in exponential representation

$$F_{(hkl)} = \sum_j f_j e^{i\alpha_j}$$

or in complex representation

$$F_{(hkl)} = A_{(hkl)} + iB_{(hkl)}$$

$$\alpha = \tan^{-1} \frac{B_{(hkl)}}{A_{(hkl)}}$$

In computational work α and $|F_{(hkl)}|$ are calculated. The phase of the wave scattered (α) in the direction of a reciprocal lattice point (hkl) situated at the position x, y, z in the unit cell relative to the origin (where x, y, z are expressed as fractions of the unit cell a, b, c) can be shown to be $[2\pi(hx + ky + lz)]$ radians, relative to the phase of the wave scattered in the same direction by an atom at the origin. The expressions for A and B can be rewritten as

$$A_{(hkl)} = \sum_j f_j \cos[2\pi(hx_j + ky_j + lz_j)]$$

$$B_{(hkl)} = \sum_j f_j \sin[2\pi(hx_j + ky_j + lz_j)]$$

In complex number representation the structure factor can be expressed as the sum of real and imaginary components (i is $\sqrt{-1}$ an imaginary number), then

$$F_{(hkl)} = A_{(hkl)} + iB_{(hkl)}$$

$$F_{(hkl)} = \sum_j f_j \cos \alpha_j + i \sum_j f_j \sin \alpha_j$$

where $e^{i\alpha_j} \equiv \cos \alpha_j + i \sin \alpha_j$ then

$$e^{i\alpha_j} \equiv \cos[2\pi(hx_j + ky_j + lz_j)] + i \sin[2\pi(hx_j + ky_j + lz_j)]$$

$$F_{(hkl)} = \sum_j f_j e^{i\alpha_j} = \sum_j^n f_j e^{[2\pi i(hx_j + ky_j + lz_j)]} = |F_{(hkl)}| e^{i\alpha_{(hkl)}}$$

The structure factor, $F_{(hkl)}$, is related to intensity, $I_{(hkl)}$, of the corresponding reflection hkl by

$$I_{(hkl)} \propto |F_{(hkl)}|^2$$

As noted earlier, a crystal contains a periodic distribution of scattering matter and the intensity pattern resulting from the interaction of x-rays with the crystal is also periodic. The mathematical theory that is most useful in describing these two periodic patterns and the relationships between them is Fourier transform theory. Collectively, structure factors in reciprocal space can be converted to electron density in direct

space, and electron density in direct space can be converted to structure factors in reciprocal space using Fourier transformations. The first of the two functions is a summation from minus infinity to plus infinity for all indices h , k , and l relating the structure factors and phase angles to the number of electrons per unit volume or electron density (represented as $\rho_{(xyz)}$) at a specific location x , y , and z , that is,

$$\begin{aligned}\rho_{(xyz)} &= 1/V_c \sum_h \sum_k \sum_l F_{hkl} \cdot e^{-i2\pi(hx + ky + lz)} \\ &= 1/V_c \sum_h \sum_k \sum_l F_{hkl} \cdot \{\cos[2\pi(hx + ky + lz)] + i\sin[2\pi(hx + ky + lz)]\}\end{aligned}$$

where V_c is the volume of the unit cell. The Fourier transform pair for calculating the structure factors and phase angles from an electron density distribution (model of the contents of the asymmetric unit) is the integration over all of direct space evaluated for each specific structure factor location, h , k , and l , that is,

$$F_{hkl} = \int_v \rho(xyz) \cdot e^{i2\pi(hx + ky + lz)} dV$$

Thus, each and every structure factor makes a contribution to the electron density function at each point in direct space, and the electron density at each and every point in direct space makes a contribution to each and every structure factor.

In centrosymmetric structures $\cos(\alpha) = \cos(-\alpha)$ but $\sin(\alpha) = -\sin(\alpha)$, thus for centrosymmetric structures the sine term will be zero and only the cosine term must be evaluated. Evaluation of $\rho(xyz)$ gives a three dimensional electron density map from which one can assign atom positions by assuming atoms lie at the positions of peaks on the map. Unfortunately, we need structure factor amplitudes and phase angles for these calculations, but we can obtain only the structure factor amplitudes from the measured intensity data. The lack of measured phase angles is called the phase problem in crystallography. Solving a crystal structure means solving the phase problem. This is generally done by obtaining a trial model of all or part of the structure (for example by the Patterson method) and calculating approximate values of the phase angles for each reflection from the trial structure, or by trying to find values of the phase angles directly from the intensity data and probabilistic relationships among the intensities (Direct methods). Description of structure solution methods is beyond the scope of this thesis, but can be found in several excellent elementary (Clegg, 1998; Glusker & Trueblood, 1985; Hammond, 1997; Massa, 2000; Rhodes, 2000) and advanced (Giacovazzo, Monaco, Viterbo, Scordari, Gilli, Zanotti & Catti, 1992; Stout & Jensen, 1989) textbooks.

The trial structure is expanded by using the calculated phases in conjunction with the observed and calculated structure factors and/or adjusted by linear least squares refinement minimizing the sum of the weighted differences of the squares of $|F_o| - |F_c|$. The crystallographic problem is decidedly nonlinear so the refinement process is repeated until the successive approximations converge (shift divided by error approaches zero). Further information on this process can be found in the textbooks referred to above.

The success or quality of the refined structure can be assessed in several ways. Perhaps the most important is a simple examination of the result with the insight of a chemist. If bond lengths, angles, or other derived quantities do not make chemical sense the model must be reexamined carefully. If the final calculated electron density difference map (observed structure factors minus calculated model structure factors) has large peaks they must be examined carefully in the context of the model to determine if they are significant and if they must be included in the final model. Finally, there are various discrepancy indices. When we compare the observed structure factors with those calculated from the correct model they must agree. The conventional discrepancy index (or residual) is defined as

$$R_I = \frac{\sum (|F_o| - |F_c|)}{\sum |F_o|}$$

For perfect data and a perfect model R_I would be zero. Discrepancy indices in the range of 0.02-0.06 (2-6%) are common for the most reliably determined structures today.

Chapter III

Instrumentation, Materials, and Techniques

3.1 Instrumentation

Unless otherwise noted equipment used in these studies is located in the Equipment Center at Suranaree University of Technology.

1. Single Crystal X-ray Diffractometers

Single crystal x-ray diffraction data were collected on two diffractometer systems. The data for the $\text{CoV}_2\text{O}_6 \cdot 2\text{H}_2\text{O}$ compound were collected on the Bruker/Siemens SMART area detector diffractometer at the Department of Physics, Thammasat University, Rangsit Campus. The TU SMART system operates only at ambient room temperature and did not have an internet connection. Limited data sets could be transferred by breaking them into parts, each smaller than 1.4 Mb using the PC control computer on the SMART system and copying the parts to a series of floppy disks for transfer to SUT. Complete frame data could only be transferred by way of DAT tape from the Silicon Graphics workstation on the SMART system to the Silicon Graphics workstation in the Equipment Center at SUT.

The data for the $\text{NiV}_2\text{O}_6 \cdot 2\text{H}_2\text{O}$ and $[\text{enH}_2]_5[\text{V}_6\text{B}_{20}\text{O}_{50}\text{H}_8] \cdot 7\text{H}_2\text{O}$ compounds were collected on the Nonius KappaCCD area detector diffractometer at the Research School of Chemistry, The Australian National University. The ANU KappaCCD system is equipped with an Oxford Cryosystems 600 variable temperature device capable of producing temperatures at the crystal from near liquid nitrogen temperature to 373 K. The operating temperature of the Cryosystems 600 was 200 K for both data sets. The ANU system is connected to the internet so moderate sized files could be transferred to SUT electronically. However, due to limitations imposed on attachment size by the Center for Computing Services at SUT full frame data files still could not be transferred by internet and were written to CD ROM for transfer.

Both diffractometers were equipped with highly-oriented pyrolytic graphite crystal incident beam monochromators. The source x-radiation was the $\text{K}\alpha$ lines ($\lambda = 0.71073 \text{ \AA}$) from a molybdenum anode operated at tube power levels of 50 kV and

either 25 mA or 30 mA. The SMART system uses standard pinhole incident beam collimators while the KappaCCD has *ifg* focusing optics incident beam collimators which increase the x-ray intensity at the sample by approximately 50-80% for molybdenum $K\alpha$ radiation. Due to the specialized nature of area detector diffractometers and to detector specific corrections, the raw frame data must be reduced to structure factors by the software that is delivered with each individual diffractometer. This requirement produces the disadvantage that the data reduction cannot be optimized based on knowledge gained during the structure solution and refinement stages. Additional details of the data collection and reduction are given in the relevant sections of Chapters 4 and 5.

2. Powder X-ray Diffractometer

Powder x-ray diffraction spectra were recorded on a Bruker/Siemens D5005 diffractometer equipped with a copper x-radiation source operating at a tube power level of 40 kV and 40 mA. Spectra evaluation was carried out with the EVA version 3 evaluation software. Samples were dusted on a plasticene substrate contained in a standard sample holder provided with the diffractometer. The more desirable alternative of mounting on zero background sample holders is not available at SUT.

3. Microwave Accelerated Reaction System

Hydrothermal synthesis carried out at Suranaree University of Technology used the MARS 5 microwave accelerated reaction system manufactured by the CEM Corporation. The MARS 5 system purchased by SUT was designed for microwave digestion of samples in preparation for various analytical chemistry techniques. Typical digestions require only a few minutes, a fact reflected in the time limitation of 60 min maximum per reaction step. An individual program on the MARS5 can have a maximum of five reaction steps, thus a maximum of five hours reaction time. The maximum microwave power delivery is 1,500 watts of microwave energy at a frequency of 2.45 GHz. Double walled reaction vessels, similar to the control vessel illustrated in Figure 3.1, with a reaction volume capacity of 50 mL and PFA fluoropolymer cover and liner sleeve inserts in Ultem polyetherimide outer sleeves were used. Reaction conditions can be controlled for either temperature (ranging to 210 °C) or pressure (ranging to 350 psi). The control vessel is charged with an equivalent volume of water and placed in the designated position in the carousel. Individual reaction mixtures are sealed in the reaction vessels and placed

symmetrically in the carousel to promote even heating. The carousel has spaces for six vessels in addition to the control vessel enabling six simultaneous reactions to be conducted.

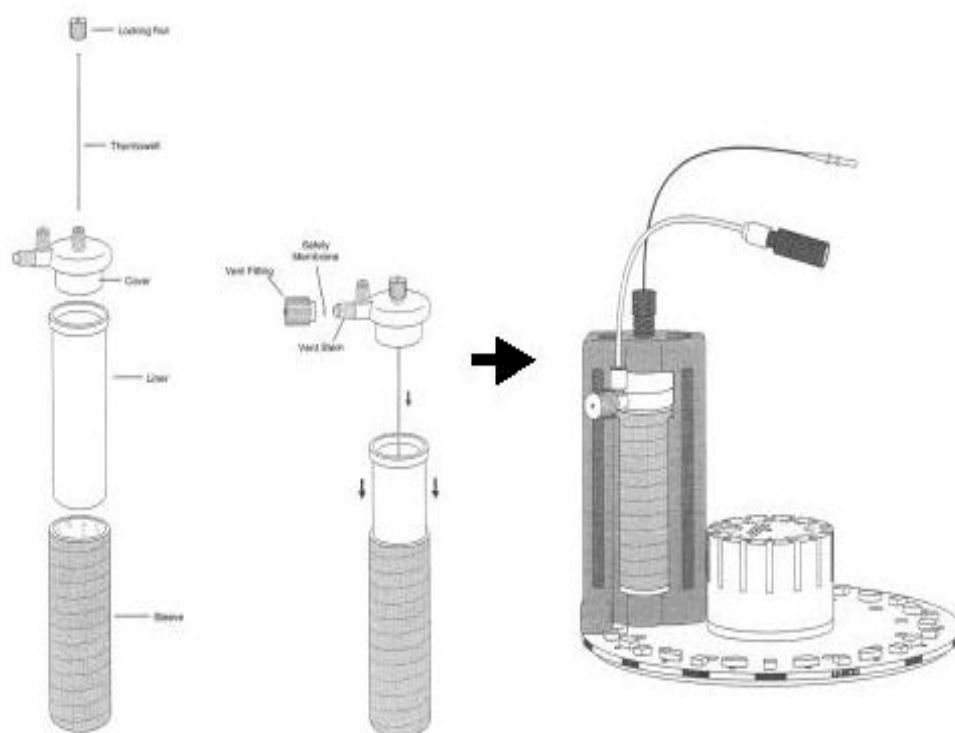


Figure 3.1. HP-500 Plus Pressure/Temperature Control Vessel Assembly.
(Reproduced with permission from CEM Corporation)

4. Thermogravimetric Analyzer (TGA)

TGA spectra were recorded on a TGA 7 thermogravimetric analyzer from Perkin-Elmer using the SCO UNIX System V/386 software to measure the change of mass of sample as a function of increasing temperature. The data is useful for evaluation of heat of sublimation, decomposition reactions, and dehydration reactions.

5. Differential Scanning Calorimeter (DSC)

DSC spectra were recorded on a Netzsch STA 409 C heat flux differential scanning calorimeter equipped with alumina sample pan, located at the Scientific and Technological Research Equipment Center, Chulalongkorn University. The technique

measures the differential heat input power required to keep a sample and reference substance isothermal as temperature is linearly increased. The data is useful for study of heats of reaction, phase transitions, and sample purity.

6. Fourier Transform Infrared Spectrophotometer (FTIR)

FTIR spectra were recorded with a Bio-Rad FTS 175C Fourier transform infrared spectrophotometer with Win-IR software. Operating power 180 VA and 0.1 cm^{-1} resolution.

7. Energy Dispersive X-ray Fluorescence Analyzer (EDX)

EDX spectra were recorded with the Link ISIS Version 1.04 Oxford energy dispersive x-ray spectrometry attachment on a JEOL scanning electron microscope model JSM 6400, running with an electron beam accelerating voltage of 20 kV, vacuum pressure 10^{-4} Pa, and tungsten filament with a working distance of 39 mm. The fluorescence attachment is capable of analyzing nitrogen or heavier elements.

3.2 Materials

1. Ammonium metavanadate NH_4VO_3

Carlo Erba, RPE for analysis, minimum assay 99.5%, chloride < 0.002%, phosphate < 0.005%, water insoluble matter < 0.005%, As (arsenic) < 0.00005%, Fe (iron) < 0.01%, Pb (lead) < 0.002%.

2. Nickel nitrate hexahydrate $[\text{Ni}(\text{NO}_3)_2 \cdot 6\text{H}_2\text{O}]$

AJAX Chemical, minimum assay 97%, chloride 0.04, sulfate 0.1, heavy metal (as Pb) 0.05, iron 0.05.

3. Copper sulfate pentahydrate $[\text{CuSO}_4 \cdot 5\text{H}_2\text{O}]$

Carlo Erba, RPE-ACS for analysis, minimum assay 99.5%, chloride < 0.0005%, diluted H_2SO_4 insoluble matter < 0.003%, substances not precipitated by sulphydric acid < 0.05%, substances precipitated by ammonium sulphide (Ni) < 0.003%, total nitrogen < 0.001%, pH of a 5% sol. at 25 °C 3.85 ± 0.15 , As (arsenic) < 0.0005%, Fe (iron) < 0.002%, Ni (nickel) < 0.002%, Pb (lead) < 0.002%, Zn (zinc) < 0.002%.

4. Manganese sulfate monohydrate [MnSO₄·H₂O]

Carlo Erba, RPE-ACS for analysis, minimum assay 98.1%, chloride < 0.005%, water insoluble matter < 0.005%, heavy metal (Pb) < 0.002%, loss on ignition < 10.0-12.0%, substance reducing KMnO₄ (O) < 0.0005%, Ca (calcium) < 0.005%, Cu (copper) < 0.0005%, Fe (iron) < 0.002%, K (potassium) < 0.005%, Ni (nickel) < 0.02 %, Na (sodium) < 0.005%, Pb (lead) < 0.0005%, Zn (Zinc) < 0.005%.

5. Calcium chloride dihydrate [CaCl₂·2H₂O]

Carlo Erba, RPE for analysis, minimum assay 99.1%, ammonium salts < 0.001%, heavy metal (Pb) < 0.0005%, nitrate < 0.001%, phosphate < 0.001%, silicate (SiO₂) < 0.005, sulfate < 0.0025%, water insoluble matter < 0.005%, pH of a 5% solution at 25 °C 6.5±2.0, As (arsenic) < 0.00005%, Ba (barium) < 0.003%, Cu (copper) < 0.0002%, Fe (iron) < 0.0002%, K (potassium) < 0.005%, Na (sodium) < 0.02%, Mg (magnesium) < 0.03%, Ni (nickel) < 0.0002% Pb (lead) < 0.0002%, Sr (strontium) < 0.01%, Zn (zinc) < 0.0003%.

6. Iron diammonium sulfate hexahydrate [Fe(NH₄)₂(SO₄)₂·6H₂O]

Fluka, Purum, minimum assay > 98%, pH of a 5% solution at 25 °C 3.5-5.0, chloride < 0.005%, Ca (calcium) < 0.005%, Cd (cadmium) < 0.005%, Co (cobalt) < 0.005%, Cu (copper) < 0.005%, K (potassium) < 0.01%, Na (sodium) < 0.01%, Ni (nickel) < 0.005%, Pb (lead) < 0.005%, Zn (zinc) < 0.005%.

7. Zinc sulfate heptahydrate [ZnSO₄·7H₂O]

Fluka, Purum, minimum assay > 99.0%, chloride < 0.005%, Ca (calcium) < 0.01%, Cd (cadmium) < 0.005%, Co (cobalt) < 0.005%, Cu (copper) < 0.005%, Fe (iron) < 0.005%, K (potassium) < 0.01%, Na (sodium) < 0.01%, Ni (nickel) < 0.005%, Pb (lead) < 0.005%.

8. Cobalt nitrate hexahydrate [Co(NO₃)₂·6H₂O]

Riedel, minimum assay 99%, insoluble matter < 0.005%, substances not precipitated by ammonium sulfide < 0.1%, chloride < 0.005%, sulfate < 0.005%, Cu (copper) < 0.001%, Fe (iron) < 0.001%, Mn (manganese) < 0.005%, Ni (nickel) < 0.1%, Pb (lead) < 0.001%, Zn (zinc) < 0.005%.

3.3 Techniques

1. Hydrothermal Synthesis

Hydrothermal reactions take place in superheated water, in a closed reaction vessel at elevated temperature and pressure ($T < 500\text{ }^{\circ}\text{C}$, $P < 2,000\text{ atm}$ for a reaction bomb, but considerably lower in the microwave reaction system at SUT). These conditions help to solubilize reagents and to stabilize new phases. Moreover, seed crystals and temperature gradient can be used for growing crystals.

$\text{CoV}_2\text{O}_6 \cdot 2\text{H}_2\text{O}$ and $[\text{enH}_2]_5[\text{V}_6\text{B}_{20}\text{O}_{50}\text{H}_8] \cdot 7\text{H}_2\text{O}$ were prepared in Ian Williams' research laboratories in Hong Kong where the reactions were run in sealed stainless steel bombs maintained at the reaction temperature in an oven.

Hydrothermal preparations carried out at SUT utilized the HP-500 plus control vessel assembly shown in Figure 3.1 above on the MARS 5 microwave system for pressure and temperature control. Weighed amounts of starting materials and water are mixed and sealed in the reaction vessel. The temperature is elevated and controlled by the amount of microwave power provided to the reaction vessels. The Internal pressure depends on the temperature and the vapor pressure of the reaction components (about 350 psi at $210\text{ }^{\circ}\text{C}$ in the HP-500 Plus vessel under aqueous conditions.)

Typical Experiments: Preparation of $\text{NiV}_2\text{O}_6 \cdot 2\text{H}_2\text{O}$. A solution of $\text{Ni}(\text{NO}_3)_2 \cdot 6\text{H}_2\text{O}$ (0.73 g) and NH_4VO_3 (0.50 g) in 50 ml of distilled water was sealed in an HP-500 Plus reaction vessel mounted in the MARS 5 microwave reactor system. The temperature was raised from ambient to $200\text{ }^{\circ}\text{C}$ over 15 min (approximate heating rate of $12.7\text{ }^{\circ}\text{C min}^{-1}$) and maintained at $200\text{ }^{\circ}\text{C}$ (187-190 psi pressure) for 2 hours, then partially cooled down over 15 minutes, all under the four-step (ramp to $200\text{ }^{\circ}\text{C}$ and hold, ramp to $200\text{ }^{\circ}\text{C}$ (no change) and hold, zero power cool for 15 min) program control. The resulting solution in the reaction vessel was allowed to stand at room temperature about 10-12 hours. The crude product was filtered, washed with distilled water, and dried at ambient pressure yielding a mixture of green and orange crystals. The two components were separated by hand under an optical stereomicroscope for further characterization of the pure products.

Preliminary studies of reactions of other M^{+2} salts with NH_4VO_3 were carried out in a fashion similar to the preparation of $\text{NiV}_2\text{O}_6 \cdot 2\text{H}_2\text{O}$, except changing the

quantity of the M^{+2} salt and continuing the reaction for five hours under the seven-step program controlled process (1 & 2, ramp to 200 °C and hold; 3, ramp to 200 °C (no change) and hold; 4, ramp to 200 °C (no change) and hold; 5, ramp to 200 °C (no change) and hold; 6, ramp to 200 °C (no change) and hold; 7, zero power cool for 15 min). Table 3.1 lists the M^{+2} salts explored along with the quantities used in each reaction and the colors of the observed products.

Table 3.1. Hydrothermal Reactions of 5 hr Duration.

M^{+2} salt	mass of M^{+2} salt	mass of NH_4VO_3	volume of H_2O	description of product
$MnSO_4 \cdot H_2O$	0.69 g	0.59 g	50 ml	thin black-blue plates
$Fe(NH_4)_2(SO_4)_2 \cdot 6H_2O$	0.98 g	0.59 g	50 ml	black plates and orange powder
$CuSO_4 \cdot 5H_2O$	0.62 g	0.59 g	50 ml	yellow-orange powder
$ZnSO_4 \cdot 7H_2O$	0.72 g	0.59 g	50 ml	orange plates and dark blue plates
$CaCl_2 \cdot 2H_2O$	0.37 g	0.59 g	50 ml	yellow-green needles

In a first step to refine the above reactions, 15 hr reaction times were explored for four M^{+2} salts by including manual intervention twice (at 5 hr and 10 hr reaction times) to reinitiate the MARS 5 controller process. The resulting 17 step process was as follows:

Steps 1 & 2	ramp to 200 °C and hold
Step 3	ramp to 200 °C (no change) and hold
Step 4	ramp to 200 °C (no change) and hold
Step 5	ramp to 200 °C (no change) and hold
Step 6	ramp to 200 °C (no change) and hold
first manual intervention Reset/Restart the MARS 5 before the cool down ramp	
Step 7	ramp to 200 °C and hold
Step 8	ramp to 200 °C (no change) and hold
Step 9	ramp to 200 °C (no change) and hold
Step 10	ramp to 200 °C (no change) and hold
Step 11	ramp to 200 °C (no change) and hold
second manual intervention Reset/Restart the MARS 5	
Step 12	ramp to 200 °C and hold
Step 13	ramp to 200 °C (no change) and hold
Step 14	ramp to 200 °C (no change) and hold
Step 15	ramp to 200 °C (no change) and hold
Steps 16 & 17	ramp to 200 °C (no change) and hold, zero power cool for 15 min

The M^{+2} salts explored with 15 hr reaction times along with the quantities used in each reaction and the colors of the observed products are given in Table 3.2.

Table 3.2. Hydrothermal Reactions of 15 hr Duration.

M ⁺² salt	mass of M ⁺² salt	mass of NH ₄ VO ₃	volume of H ₂ O	description of product
Co(NO ₃) ₃ ·6H ₂ O	0.73 g	0.59 g	50 ml	thin black-blue plates
Ni(NO ₃) ₃ ·5H ₂ O	0.73 g	0.59 g	50 ml	thin orange plates and green powder
ZnSO ₄ ·7H ₂ O	0.72 g	0.59 g	50 ml	slightly orange plates and dark blue plates
CaCl ₂ ·2H ₂ O	0.37 g	0.59 g	50 ml	green needles

After these preliminary experiments the MARS 5 control system failed making the equipment unavailable for further experiments. Thus characterization results are only available for NiV₂O₆·2H₂O.

2. Energy Dispersive X-ray Fluorescence Spectrometry

Place 2 or 3 crystals of the green NiV₂O₆·2H₂O on double stick carbon tape on the brass stub sample holder and place in the sample port of the JEOL scanning electron microscope. Locate the crystals with the x-ray beam and analyze the x-radiation produced with the Link ISIS Version 1.04 Oxford energy dispersive x-ray analyzer. The EDX spectrum is shown in Figure 3.2. The peak assignments of vanadium and nickel are made by the software. The relative peak areas indicate more vanadium than nickel, consistent with the 2:1 ratio confirmed by the single crystal x-ray structure determination.

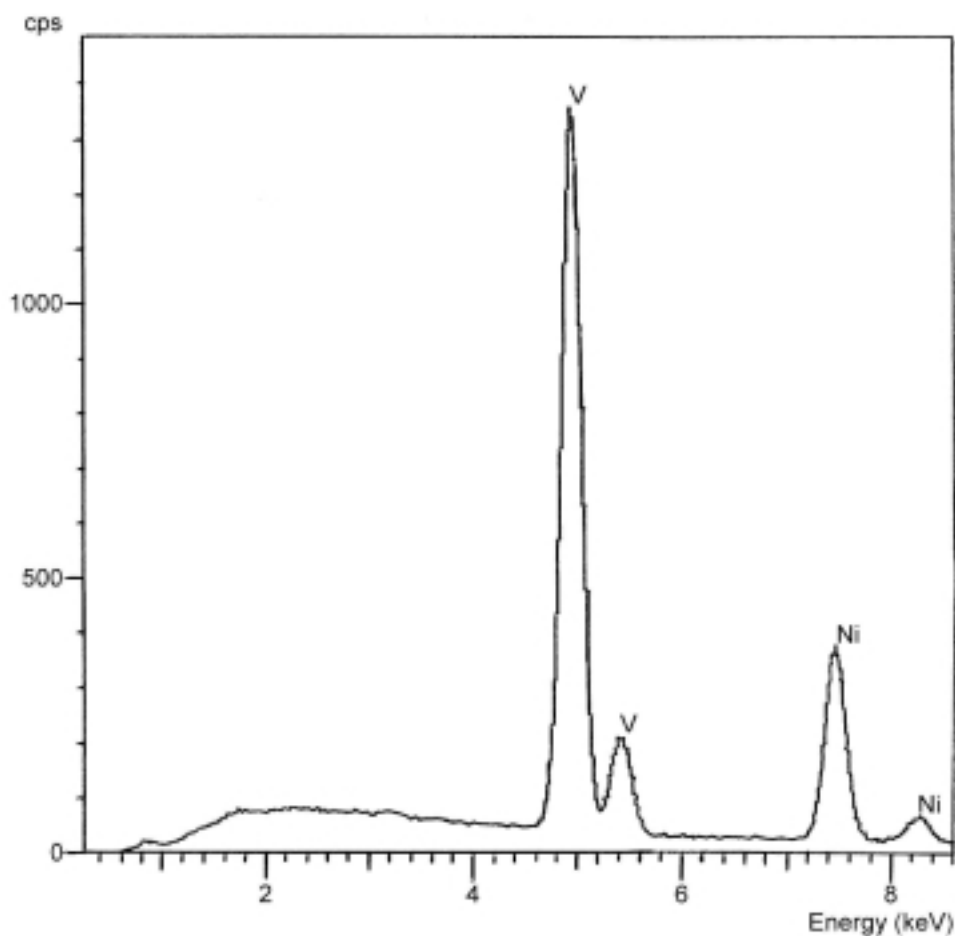


Figure 3.2. EDX Spectrum of $\text{NiV}_2\text{O}_6 \cdot 2\text{H}_2\text{O}$.

3. Fourier Transform Infrared Spectrometry

Mix one milligram of sample with dried potassium bromide powder and grind to a very fine power with an agate mortar and pestle. Press the ground powder into a transparent disk using a hydraulic press at 10 tons of pressure for 1 min. Place the pellet in the sample holder in the instrument beam and record the Mid-IR range ($4000\text{-}400\text{ cm}^{-1}$ or $2.5\text{-}25\text{ mm}$), the fundamental vibration region of the spectrum most used for analytical spectroscopy.

4. Thermogravimetric Analysis

Place 9-10 mg of $\text{NiV}_2\text{O}_6 \cdot 2\text{H}_2\text{O}$ in the platinum sample pan and start the N_2 purge. Two temperature ranges with different heating rates were used; range of $25\text{-}500\text{ }^\circ\text{C}$ with heating rate of $1\text{ }^\circ\text{C min}^{-1}$ required about 8 hours (Figure 3.3) and the second range of $25\text{-}900\text{ }^\circ\text{C}$ with heating rate of $5\text{ }^\circ\text{C min}^{-1}$ required about 3 hours

(Chapter 4, Figure 4.8). In either case when the maximum temperature was reached the instrument was switched off and the sample allowed to cool to room temperature in the instrument.

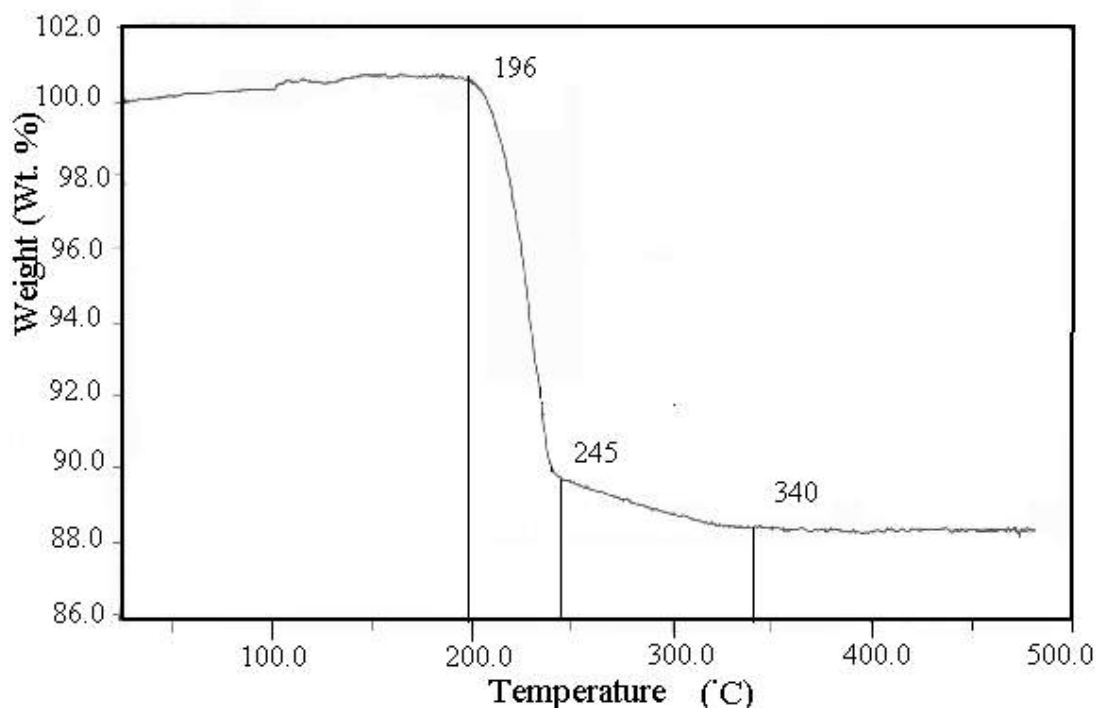


Figure 3.3. TGA curve of NiV₂O₆·2H₂O (5 °C/min).

5. Differential Scanning Calorimeter

Place 20 mg of Al₂O₃ and 9.9 mg of NiV₂O₆·2H₂O on the sample pan and 20 mg of Al₂O₃ on the reference pan of the Netzsch STA 409 C heat flux differential scanning calorimeter. The pans are made from alumina and the analysis is carried out under an N₂ inert atmosphere. In a typical extended range experiment the heating rate is 5 °C min⁻¹ over the range 20-900 °C, taking about 3 hours.

6. Power X-ray Diffractometry

About 10-14 mg of powdered sample, either NiV₂O₆·2H₂O or derived from NiV₂O₆·2H₂O by heat pretreatment as described below, was ground to a fine powder that is as homogeneous as possible. The sample holder well is about 5 mm diameter so cannot be completely filled with the limited sample, so the well was filled with a plasticene base and the ground sample powder was dusted on the surface of the

plasticene for analysis. A blank was recorded for plasticene only which was subtracted from each of the subsequent spectra. All spectra were recorded on the Bruker/Siemens D5005 diffractometer using the spinning sample option and scanning 2θ from 8 to 80° with 0.3 degree steps each recorded for 1.00 sec giving a total scan time of 4 minutes.

The samples for the spectra identified as 200, 280, 330, 450, 800 and 900 $^\circ\text{C}$ were subjected to a pretreatment step of heating in the TGA analyzer at a rate of 5°C min^{-1} to the specified temperature. The TGA analyzer was switched off and the sample allowed to return to ambient temperature overnight then stored in a dessicator until the spectra were recorded. The spectral traces are given in Figure 3.4. Values of two theta, interplanar spacing, intensity in absolute counts, and intensity in relative % were derived from the recorded spectra by the D5005 analysis software and are given in Chapter 4, Table 4.13.

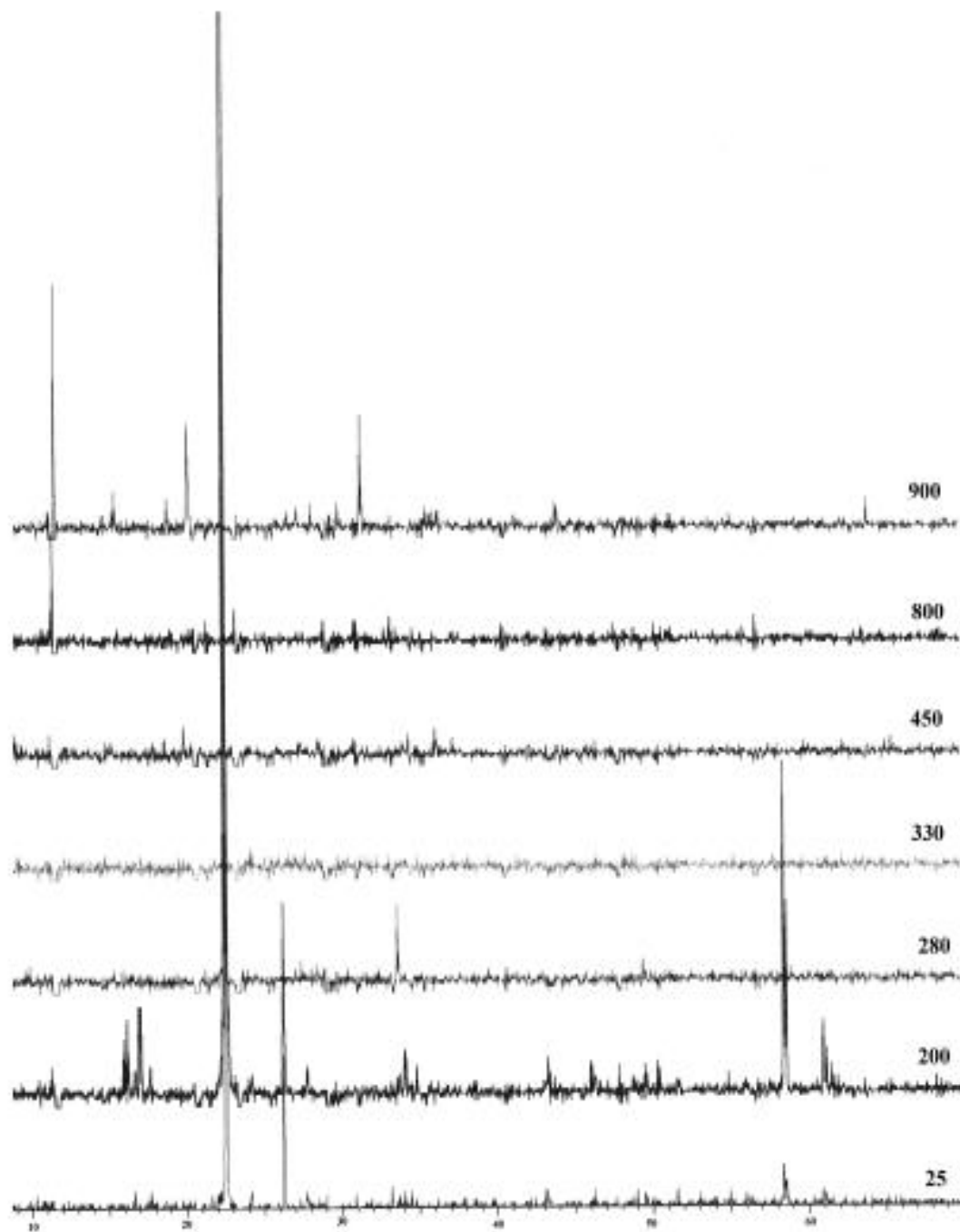


Figure 3.4. Thermodiffraction from XRD.

Chapter IV

$MV_2O_6 \cdot 2H_2O$, $M = Co, Ni$

4.1. Introduction

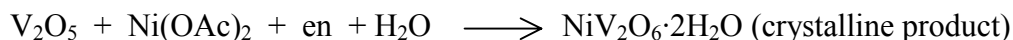
The structure of the cobalt compound, $CoV_2O_6 \cdot 2H_2O$, was reported in 1988 (Murashova, Velikodnyi, Potapov & Trunov, 1988) along with dehydration data obtained by thermogravimetric analysis (TGA). The authors found a framework structure made up of VO_4 tetrahedra and the equatorial oxygens of the CoO_6 octahedra. The water molecules occupy the axial positions of the CoO_6 octahedra and were found to have equivalent bond lengths in the structure. Hydrogen atoms were not located and hydrogen bond analysis was not reported. The authors also report two waves in the TGA spectrum for the loss of the waters of hydration.

The structure of the isomorphous nickel compound, $NiV_2O_6 \cdot 2H_2O$, was reported during the course of this thesis work (Baudrin, Touboul & Nowogrocki, 2000), and represents an improvement on the previous cobalt work. The authors reported a significant difference in the coordination of the two water molecules, but did not provide explanation for the difference and did not report thermal analysis data. The structure of a third isomorphous compound with manganese as the metal has also been reported along with thermal analysis data (Liao, Drezen, Leroux, Guyomard & Piffard, 1996). Structural features are similar to those of the nickel compound. A common feature of the nickel and manganese structures is large anisotropy, oriented perpendicular to the mirror plane on which the water molecules are located, in the atomic displacement parameters of one of the water oxygens.

Reevaluation of the nickel and cobalt structures demonstrates that the large anisotropy of the water oxygen is due to disorder. Examination of the environments about the water molecules shows that they have quite different bonding patterns with the ordered molecule engaged in three hydrogen bonds in addition to the coordination bond, and the disordered molecule engaged in only two hydrogen bonds in addition to the coordination bond. The new structural data also helps understand the thermal analysis data.

4.2. Experimental, NiV₂O₆·2H₂O

The single crystal selected for x-ray data collection was provided as a mounted sample by Dr. Ian D. Williams, Hong Kong University of Science and Technology. It was synthesized as an accidental product of the following hydrothermal reaction intended to produce an organically templated porous material.



The material was subsequently synthesized again by hydrothermal techniques, but without the ethylene diamine, for thermal analysis and other characterizations as described in Chapter 3.

The green sample crystal having dimensions, 0.18 x 0.22 x 0.48 mm, was mounted on the end of a solid glass fiber with epoxy cement. Preliminary examination and data collection were carried out on an Enraf-Nonius KappaCCD diffractometer equipped with a fine focus molybdenum anode ($\lambda_{\text{MoK}\alpha} = 0.71073 \text{ \AA}$) x-ray tube powered at 40 kV and 25 mA, a graphite crystal monochromator, a 0.5 mm *ifg* capillary collimator, and an Oxford Cryosystems 600 low temperature device operating at 200 K. Preliminary examination established an orthorhombic unit cell for which four series of omega scans with total scan length of 346.6 ° were created in response to the design goal of four times redundancy on at least 90 % of the collected data. Data were collected with the detector 25.0 mm from the sample crystal at a scan rate of 8.0 °/min as four series of omega scans each divided into steps 2.0 ° in thickness using the COLLECT routine (Nonius BV, 2000). The three dimensional data were extracted from the scans and corrections for Lorentz and polarization applied with the Denzo/Scalepack (Otwinowski & Minor, 1997) software package which produces properly scaled reduced data from the three dimensional scan data. Absorption corrections were applied to the intensity data from symmetry related reflections using the multiscan technique implemented in the SORTAV routine (Blessing, 1995, 1997) of the maXus package (Mackay, Gilmore, Edwards, Tremayne, Stuart & Shankland, 1998). R_{multiple} , the merging R factor for combining multiple measurements of the same reflection was reduced from 0.066 before the multiscan correction to 0.034 after the multiscan correction, and R_{sym} , the discrepancy factor for combining symmetry related reflections is 0.089.

Initial coordinates for the nonhydrogen atoms were taken from the previously determined isomorphous cobalt structure (Murashova, Velikodnyi, Potapov &

Trunov, 1988) which places the M atom and both water oxygen atoms (designated O3 and O5) on the mirror plane at $y = 1/4$. Atoms located on a symmetry element will be included in the refinement process with occupancy factors less than unity since, as the program performs the symmetry operations it will generate the rest of the atom occupancy. Therefore, the atoms located on the mirror plane are given occupancy factors of 0.5 and the mirror operation generates the other half of the atom's electron density. The initial nonhydrogen coordinate values were refined in two stages by full matrix least squares refinement, first assuming isotropic atomic displacement motion, and then assuming anisotropic atomic displacement motion.

Positions for the hydrogen atoms of the unique two half water molecules were located from an electron density difference Fourier calculation. Two suitable positions located on the mirror plane near O3 were included in the model as two half occupancy isotropic hydrogen atoms, while one suitable general position found near O5 was included in the model as one full occupancy hydrogen atom, all with displacement parameters fixed to be 10% greater than those of the oxygen atoms to which they are bonded. The coordinates of the hydrogen atoms were allowed to vary within the symmetry constraints that hydrogen atoms on O3 must also remain on the mirror plane. The three oxygen-hydrogen bond lengths were constrained to be equivalent.

The refinement converged with discrepancy indices $R_1 = 0.031$ and $R_w = 0.127$, but unreasonable geometry for one water molecule ($d[\text{O3-H2}] = 0.821$, $d[\text{O3-H3}] = 2.051 \text{ \AA}$). On further inspection it was noted that the anisotropic atomic displacement parameter for O3 was considerably larger and more anisotropic (maximum amplitude about 0.038 \AA^2) than displacement parameters on other atoms of the structure (maximum amplitude less than 0.026 \AA^2). The orientation of the high anisotropy was perpendicular to the mirror plane as shown in Figure 4.1a. Figure 4.1b shows a simple graphical fit constructed of two isotropic half oxygen atom positions to approximate the anisotropic ellipsoid. The graphical fit indicates reasonable coordinates (0.235 and 0.265) displaced plus and minus 0.16 \AA relative to the mirror plane at $y = 1/4$. As oxygen atom O3 was split and disordered off of the mirror plane, the associated half hydrogen atoms were also allowed three dimensional flexibility within the restraint that all O-H distances are similar. The apparent separation of the two oxygen atom positions is 0.32 \AA which is considerably less than the resolution of the data set which leads to the refinement difficulty noted later.

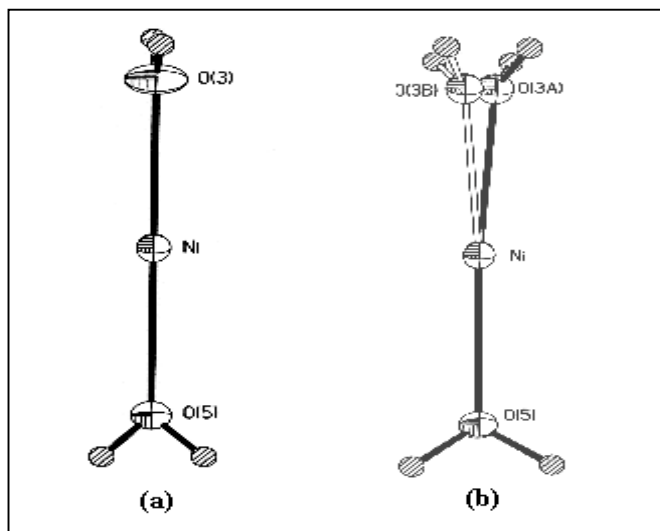


Figure 4.1. Disorder Model for O3 in $\text{NiV}_2\text{O}_6 \cdot 2\text{H}_2\text{O}$. a) Large anisotropy of O3 perpendicular to the mirror plane at $y = 1/4$. b) Disorder model.

Refinement of the disorder model converged with discrepancy indices $R_1 = 0.030$ and $R_w = 0.080$ (R_w being the more significant in assessing model improvement (Hamilton, 1964) as it is related to the quantity being minimized in the least squares refinements). The displacement of O3 from the mirror plane was ill-behaved in the least squares process so was refined by carrying out parallel refinements with the y coordinates of O3A and O3B adjusted manually, then held constant while the remainder of the model was refined to convergence. The resulting best displacement from the mirror plane was 0.014 in fractional coordinates (0.15 \AA), but the geometry about the water molecules was still not satisfactory. Therefore, additional restraints to make all Ni-H nonbond distances similar, and to make the two halves of the disordered water exactly mirror related were added.

The final model thus included all nonhydrogen atoms except O3 with anisotropic atomic displacement parameters, the nickel atom and water atom O5 on the mirror plane, two mirror related positions for the disordered O3 with identical isotropic atomic displacement parameters, and hydrogen atom positions constrained and restrained as described above. The displacement of O3A and O3B from the mirror plane was again optimized by parallel refinements as described above. Refinement converged with discrepancy indices $R_1 = 0.0303$ and $R_w = 0.0786$ with a goodness of fit of 1.216. The final refined displacement of O3 from the mirror plane was 0.014 (0.148 \AA) and the final refined value for $d[\text{O}-\text{H}]$ was 0.82 \AA . The final difference electron density Fourier map had maximum negative and positive peaks of -0.93 and 0.69 e \AA^{-3} respectively, with estimated error on the map of 0.15 e \AA^{-3} . Crystal data and

refinement details for this structure solution and refinement are given in Table 4.1, along with data for the isomorphous cobalt compound discussed later in this chapter and the isomorphous manganese compound studied previously (Liao, Drezen, Leroux, Guyomard & Piffard, 1996).

Table 4.1. Crystal Data for the Isomorphous $MV_2O_6 \cdot 2H_2O$ Compounds.

Compound	NiV ₂ O ₆ ·2H ₂ O	CoV ₂ O ₆ ·2H ₂ O	MnV ₂ O ₆ ·2H ₂ O
Formula weight	292.62	292.86	288.8
Color	green	ruby red	
Crystal size (mm)	0.18x0.22x0.48	0.3x0.4x0.5	0.25x0.43x0.45
Crystal system	orthorhombic	orthorhombic	orthorhombic\
Space group	P _{nma}	P _{nma}	P _{nma}
Unit cell dimension			
<i>a</i> (Å)	5.5322(2)	5.5745(2)	5.6075(4)
<i>b</i> (Å)	10.6201(4)	10.7030(3)	10.9094(7)
<i>c</i> (Å)	11.7524(4)	11.8642(3)	12.030(2)
<i>V</i> (Å ³)	690.48	707.86	735.8
<i>Z</i>	4	4	4
<i>d</i> _{calc} (mg/m ³)	2.815	2.748	2.571
Radiation type	MoKα	MoKα	MoKα
Wavelength (Å)	0.71073	0.71073	0.71073
Temperature (K)	200	295	room
<i>μ</i> (mm ⁻¹)	5.35	4.90	4.17
Diffractionmeter	KappaCCD	SMART	
Absorption corrections	Multiscan	Multiscan	
Measured reflections	10732	6577	
<i>R</i> _{int}	0.0887	0.0461	
<i>R</i> _{sigma}	0.0364	0.0295	
2θ _{max}	60.0	61.0	
<i>h</i> range	-7 to 7	-7 to 7	
<i>k</i> range	-13 to 14	-15 to 15	
<i>l</i> range	-14 to 16	-15 to 16	
Refinement			
Refinement on	<i>F</i> ²	<i>F</i> ²	
<i>R</i> , [<i>F</i> ² > 2σ(<i>F</i> ²)]	0.0303	0.0258	0.024
<i>R</i> _w	0.0786	0.0272	0.027
goodness of fit	1.216	1.209	3.44
independent data	1051	1092	3134
<i>F</i> ² > 4σ(<i>F</i> ²)	1023	1018	2667
ρ _{max} /ρ _{min} /ρ _{error} (e Å ⁻³)	0.69/-0.93/0.15	0.48/-0.84/0.13	1.02/-0.87
refinement software	SHELXTL v5.1	SHELXTL v5.1	SHELXTL-PLUS 4.0

The fractional orthorhombic coordinates with equivalent isotropic atomic displacement parameters, and the anisotropic atomic displacement parameters for $\text{NiV}_2\text{O}_6 \cdot 2\text{H}_2\text{O}$ are gathered in Tables 4.2 and 4.3, respectively.

Table 4.2. Fractional Monoclinic Coordinates and Isotropic Atomic Displacement Parameters for $\text{NiV}_2\text{O}_6 \cdot 2\text{H}_2\text{O}$.

Atom	x	y	z	$U_{eq}(\text{\AA}^2)$
Ni	0.0202(1)	1/4	0.4592	0.0095(2)
V	0.1958(1)	0.53193(4)	0.32612(3)	0.0090(2)
O1	0.1654(3)	0.3801(2)	0.3539(2)	0.0158(4)
O2	-0.1141(3)	0.3850(2)	0.5631(2)	0.0163(4)
O3A	-0.2947(5)	0.264	0.3714(2)	0.0136(5)
H2A	-0.421(2)	0.286(2)	0.403(2)	0.025
H3A	-0.298(4)	0.286(3)	0.3049(9)	0.025
O3B	-0.2947	0.236	0.3714(2)	0.0136(5)
H2B	-0.421(2)	0.214(3)	0.403(2)	0.025
H3B	-0.298(4)	0.214(3)	0.3049(9)	0.025
O4	0.005(3)	0.5724(2)	0.2069(2)	0.0144(4)
O5	0.3420(5)	1/4	0.5483(2)	0.0141(5)
H1	0.375(7)	0.313(1)	0.596(3)	0.03(1)

Table 4.3. Anisotropic Atomic Displacement Parameters for $\text{NiV}_2\text{O}_6 \cdot 2\text{H}_2\text{O}$.

Atom	U_{11}	U_{22}	U_{33}	U_{12}	U_{13}	U_{23}
Ni	0.0123(2)	0.0098(3)	0.0064(2)	0	0.0009(1)	0
V	0.0108(2)	0.0095(2)	0.0067(2)	-0.0003(1)	0.0007(1)	0.0000(1)
O1	0.0207(8)	0.0126(8)	0.0141(8)	-0.0003(7)	0.0023(6)	0.02(1)
O2	0.0184(9)	0.0171(9)	0.0136(8)	0.0021(7)	0.0038(6)	-0.005(1)
O4	0.0130(8)	0.018(9)	0.0123(7)	-0.0019(6)	-0.0012(6)	0.0034(7)
O5w	0.016(1)	0.015(1)	0.012(1)	0	-0.0034(8)	0

4.3. Structure Description, NiV₂O₆·2H₂O

Green crystals from synthesis were studied by EDX which shows the crystals contain nickel and vanadium and indicates more vanadium than nickel. An ORTEP style drawing showing the local environment of the nickel and vanadium atoms for the structure of NiV₂O₆·2H₂O is shown in Figure 4.2. A crystallographic mirror plane runs vertically through atoms Ni and O5 and the symmetry related NiB and O5B. Additional parallel mirror planes occur through the Ni and O5 atoms along the left and right extremes of the diagram. The pseudo octahedral nature of the NiO₆ coordination groups can be seen from atoms Ni and NiB near the center of the drawing. Each of the equatorial oxygen atoms (O1, O2, and mirror related O1A and O2A) acts as a bridge connecting to one of the four nearest vanadium atoms ($d[\text{Ni}-\text{O}] = 2.022(2)$ and $2.025(2)$ Å), while the axial oxygen atoms are from the two waters of hydration. The water molecule containing O5 is located on the mirror plane and ordered, but the molecule containing O3 (the O3B sites are not drawn in this diagram) is pulled off of the mirror plane by its hydrogen bonding interaction to the framework oxygen atom O1.

The pseudo tetrahedral nature of the VO₄ coordination can easily be seen for the four vanadium atoms (V and symmetry related VA, VB, and VC) connected to Ni through the bridges described above. Vanadium atoms are also connected by bridging oxygen atoms. Each vanadium atom binds to two oxygen atoms that bridge to other vanadium atoms ($d[\text{V}-\text{O}] = 1.805(2)$ and $1.807(2)$ Å) and two oxygen atoms that bridge to nickel atoms ($d[\text{V}-\text{O}] = 1.636(2)$ and $1.653(2)$ Å). All of the framework oxygen atoms bridge two and only two metal atoms.

The two crystallographically independent water molecules show distinctly nonequivalent binding to the nickel atom as seen in the Ni–O coordination distances which differ by 0.036 Å or twelve standard deviations; $d[\text{Ni}-\text{O3}] = 1.030(3)$ Å and $d[\text{Ni}-\text{O5}] = 1.066(3)$ Å.

The metal oxide distances and angles are all normal. Selected interatomic distances and angles for the metal oxide framework and the coordinated water molecules is given in Table 4.4.

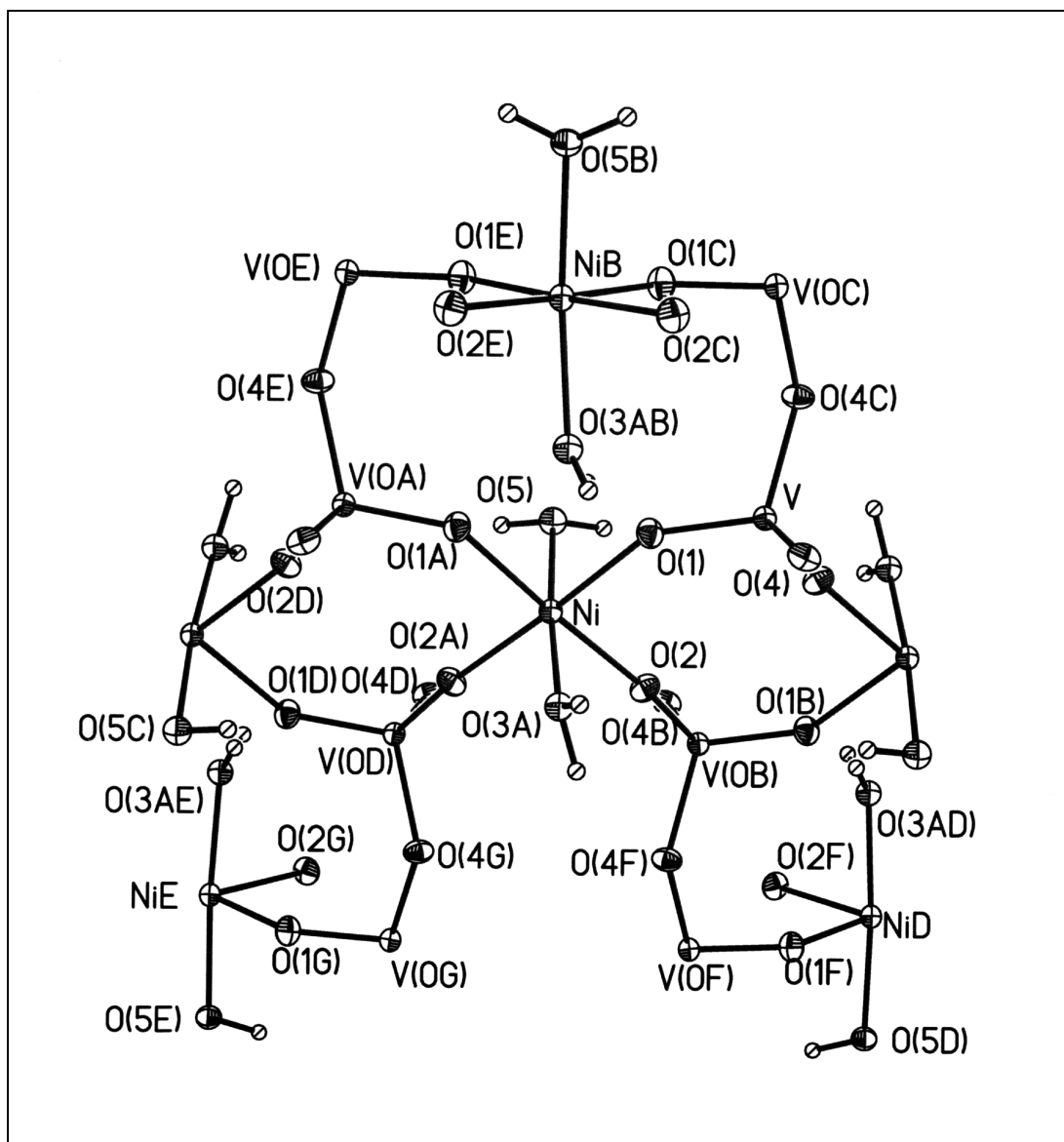


Figure 4.2. $\text{NiV}_2\text{O}_6 \cdot 2\text{H}_2\text{O}$ Showing NiO_6 and VO_4 Coordination.

Table 4.4. Selected Distances (Å) and Angles (deg) for NiV₂O₆·2H₂O.

NiO ₆ octahedron					
Ni–O1	2.022(2)		O1–Ni–O1'	86.24(11)	
Ni–O2	2.025(2)		O1–Ni–O2	91.79(8)	
Ni–O3	2.030(3)		O1–Ni–O2'	177.69(8)	
Ni–O5	2.066(3)		O1–Ni–O3	88.85(8)	
			O1–Ni–O5	88.16(7)	
			O1'–Ni–O2	177.69(8)	
			O1'–Ni–O2'	91.79(8)	
			O1'–Ni–O3	94.59(8)	
			O1'–Ni–O5	88.16(7)	
			O2–Ni–O2'	90.16(11)	
			O2–Ni–O3	86.56(8)	
			O2–Ni–O5	90.59(7)	
			O2'–Ni–O3	92.51(8)	
			O2'–Ni–O5	90.59(7)	
			O3–Ni–O5	175.80(1)	
VO ₄ tetrahedron					
V–O2'	1.636(2)		O1–V–O2'	109.93(10)	
V–O1	1.653(2)		O1–V–O4	109.02(9)	
V–O4	1.807(2)		O1–V–O4'	111.75(9)	
V–O4'	1.805(2)		O2'–V–O4	109.15(9)	
			O2'–V–O4'	107.70(9)	
			O4–V–O4'	109.26(6)	

The water molecules of hydration, in addition to completing the octahedral coordination sphere about the nickel atoms, also interact with the framework and each other *via* hydrogen bonds as they occupy the pores in the framework structure. Hydrogen bond parameters describing these interactions are given in Table 4.5.

Table 4.5. Hydrogen Bond Parameters for NiV₂O₆·2H₂O.

D–H	d[D–H];(Å)	d[H---A];(Å)	<DHA;(deg)	d[D···A];(Å)	A
O3–H2	0.824	2.188	143.9	2.895	O5 ^(I)
O3–H3	0.817	2.124	168.0	2.929	O1 ^(II)
O3–H3	0.817	2.124	168.0	2.929	O1 ^(III)
O5–H1	0.888	1.907	168.83	2.783	O4 ^(IV)

Symmetry codes: (I) $x-1, y, z$; (II) $x-1/2, y, -z-1/2$; (III) $x-1/2, -y-1/2, -z+1/2$; (IV) $-x+1/2, -y+1, z+1/2$.

The crystallographically independent water molecules from two adjacent nickel centers are interrelated, but have quite different environments within the pores as illustrated in Figure 4.3. One molecule of water (O5W) has three strong hydrogen bond interactions while the second molecule (O3W) has only two somewhat weaker hydrogen bonds. This is a result of hydrogen bonding to the two different types of oxygen on the vanadium centers. O5W interacts with the more favorably placed V–O4–V bridging oxygen atoms which accommodate a cooperative pair of equivalent O–H···O hydrogen bonds with O5W acting as the hydrogen bond donor.

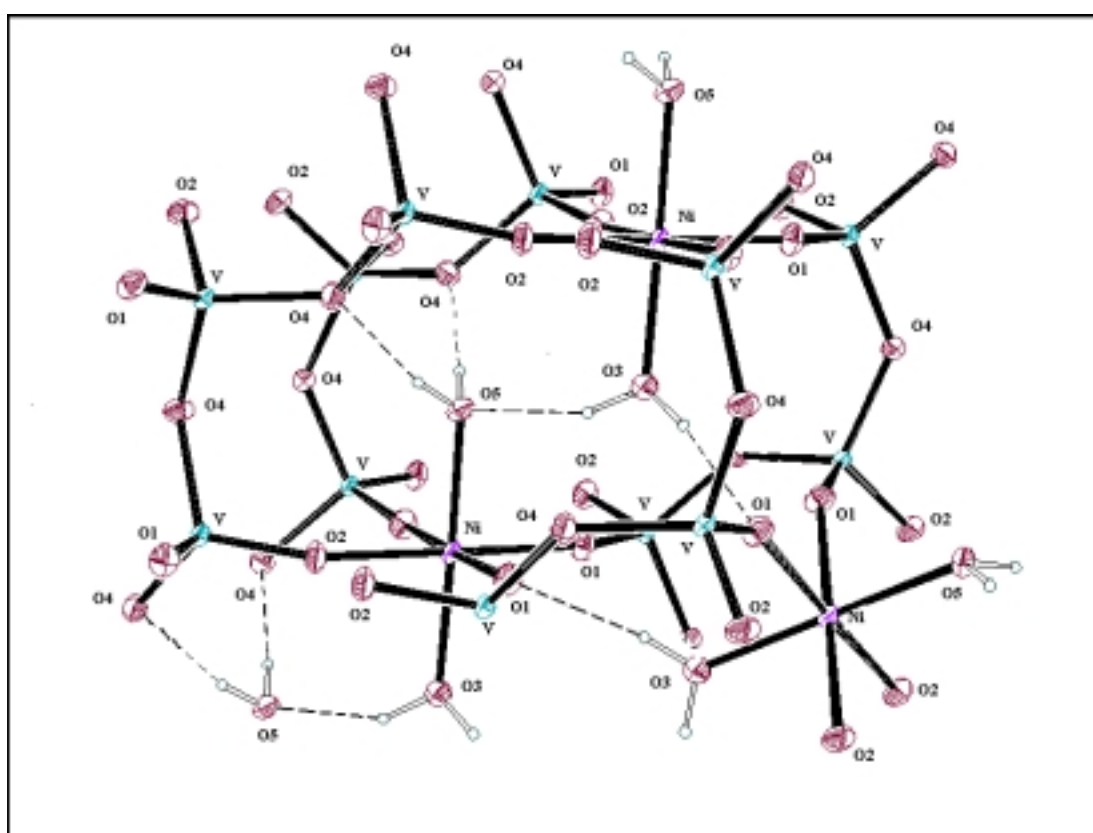


Figure 4.3. Hydrogen Bonding of NiV₂O₆·2H₂O.

On the other hand O3W interacts with the V–O–Ni bridging oxygen atoms which are at a greater distance, such that O3 moves 0.148 Å away from the mirror plane to function as a good hydrogen bond donor to O1. This is the source of the disorder as in any given pore location the two O1 positions are equivalent relative to the mirror plane. When the water molecule enters the lattice it will hydrogen bond to one or the other of the O1 positions giving a statistical distribution in the total crystal. The remaining hydrogen on O3 is then nearer to the lone pair on water molecule O5W

than it is to the mirror related O1 position, thus causing donation of the second O3W hydrogen atom to O5W. As there are no other available hydrogen bond donors in the structure O3W does not have the opportunity to accept a hydrogen bond and is left with only two hydrogen bonds.

The net result is unequal competition for the electron density from O3w and O5w. The 0.036 Å lengthening of the Ni–O5 bond relative to the Ni–O3 bond can be understood on this basis, as O5W has one Ni–O coordination bond and three hydrogen bonds, while O3W has one Ni–O coordination bond but only two hydrogen bonds. The strongest hydrogen bonds at 2.783 Å are those between O5W and O4, perhaps due to the cooperative effect of the paired interactions. The interaction between the two water molecules is 0.11 Å longer at 2.895 Å, comparable to the O3W to O1 interaction at 2.929 Å. It is interesting that the strongest hydrogen bonds are to O5W and more hydrogen bonds form to O5W, correlating with the weaker water to nickel coordination bond also being to O5W.

The structure can be described as a 3-dimensional network of interconnected NiO₆ octahedra and VO₄ tetrahedra. The VO₄ tetrahedra form parallel corner connected chains propagating approximately along the [100] direction. Each NiO₆ octahedra interconnects two chains in the [010] and two chains in the [001] direction as illustrated in Figure 4.4. The interconnections produce extremely small micropores bounded by -Td-Oh-Td-Oh- rings in the [010] direction (horizontal in Figure 4.4) and somewhat larger micropores bounded by -Td-Td-Oh-Td-Td-Oh- rings in the [001] direction (vertical in Figure 4.4; also visible in Figure 4.2). The water molecules occupy channels as illustrated in Figure 4.5, projecting the structure on the mirror plane (rotation of Figure 4.4 by 90 ° about the vertical axis). The channels are bounded by the largest rings in the structure. If the water molecules could be removed the structure would be porous with an approximately 5 x 7 Å channel through the crystal bounded by -Td-Td-Td-Oh-Td-Td-Td-Oh- rings.

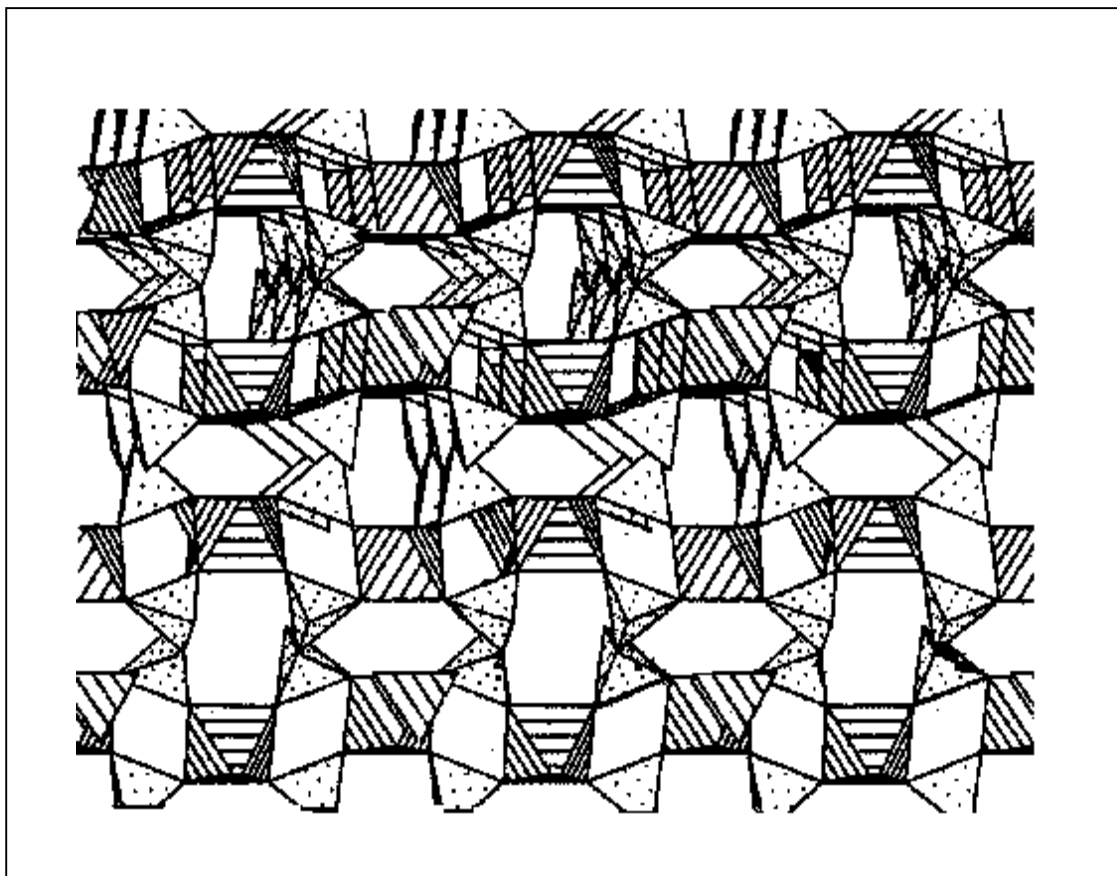


Figure 4.4. Structure of $\text{NiV}_2\text{O}_6 \cdot 2\text{H}_2\text{O}$ Projected Parallel to $[100]$.

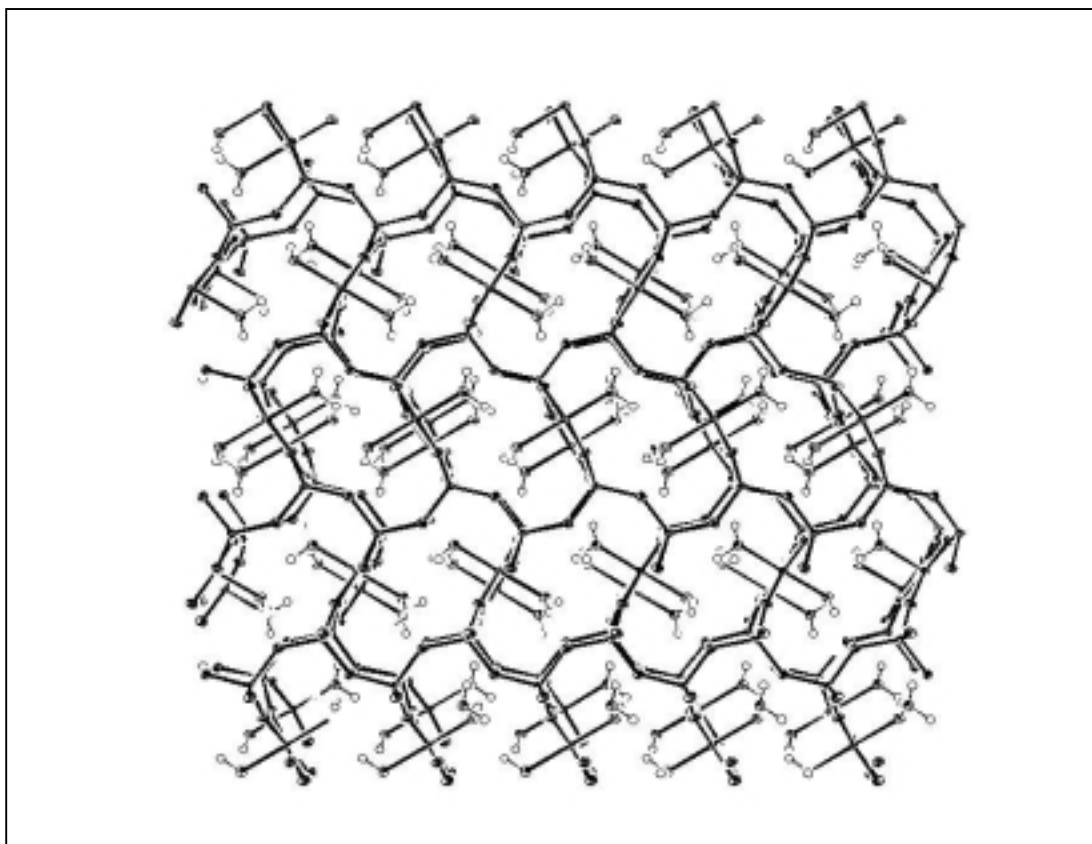


Figure 4.5. Structure of $\text{NiV}_2\text{O}_6 \cdot 2\text{H}_2\text{O}$ Projected Parallel to $[010]$.

A valence bond sum calculation (Brown & Altermatt, 1985) used to check the validity of structure resolutions, showed that Ni and V are in +2 and +5 oxidation state in the compound. Moreover, a valence of around -2 is found for all the oxygen atoms. The application of this model to solids presenting hydrogen bonds is not easy. To solve this problem the graphical correlations of Brown & Altermatt were used to calculate the O-H valence by subtracting the $\text{H} \cdots \text{O}$ hydrogen bond valence from 1.0 to obtain the results shown in Table 4.6.

Table 4.6. Bond Valence Sums for Atoms in NiV₂O₆·2H₂O.

	O1	O2	O4	O3 _w	O5 _w	S _{CAL}	S _{THEO}
Ni	(0.37x2)	(0.367x2)		0.362	0.328	2.164	2
V	1.496	1.57	(0.989,0.995)			5.05	5
H1			0.195		(0.805x2)		1
H2			0.845	0.155			1
H3	(0.14)		0.86				1
S _{CAL}	2.006	1.937	2.179	2.067	2.093		
S _{THEO}	2	2	2	2	2		

4.4. Structure of CoV₂O₆·2H₂O

The structure of the isomorphous cobalt compound has been previously reported (Murashova, Velikodnyi, Potapov & Trunov, 1988). The authors reported the structure of CoV₂O₆·2H₂O with $R_1 = 0.045$ for observed data, $Z = 4$, $\rho = 2.579 \text{ g/cm}^3$, $a = 5.57$, $b = 10.71$, $c = 11.86 \text{ \AA}$. Due to low quality data they were unable to include the hydrogen atoms on the water molecules. They found equivalent Co-O bonds of 2.10(1) and 2.12(1) \AA for the oxygen atoms of the two axial water molecules that complete the coordination octahedra. The cobalt atom and both water molecules were located on the mirror plane. They also reported TGA and DTA results which showed two different temperatures for dissociation of the two water molecules, corresponding to temperatures about 250 °C and 290 °C. They also report the material becomes amorphous when heated above 270 °C. The similarity of their structure and the current nickel structure can be seen by comparing the network diagrams in Figures 4.4. and 4.6.

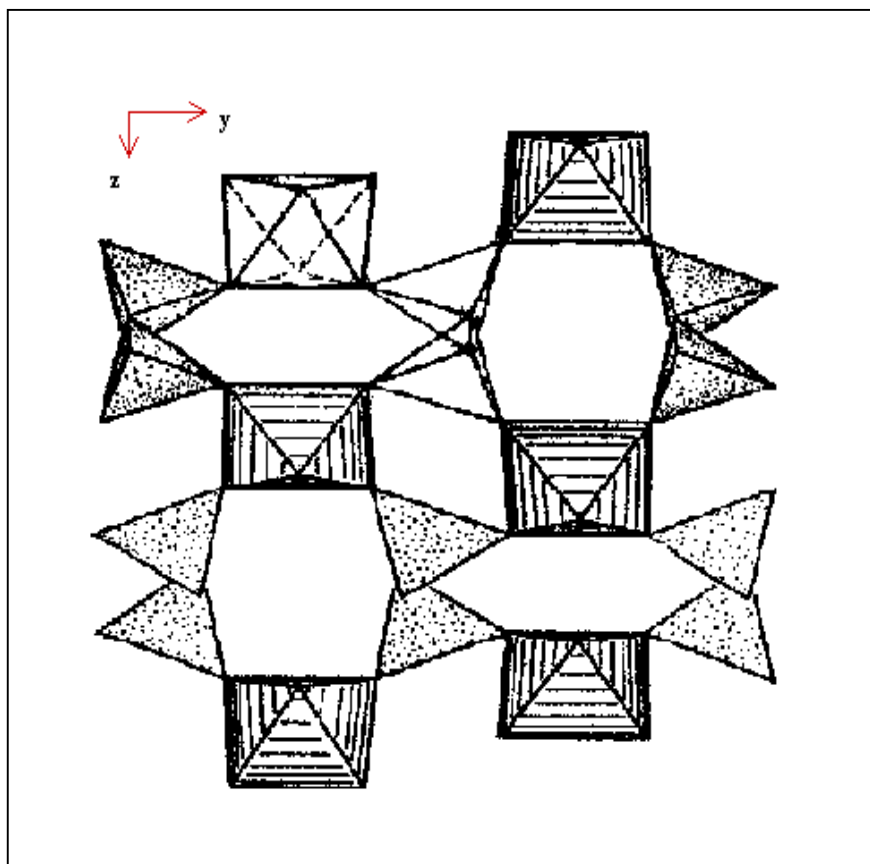


Figure 4.6. Structure of $\text{CoV}_2\text{O}_6 \cdot 2\text{H}_2\text{O}$.

The structure of $\text{CoV}_2\text{O}_6 \cdot 2\text{H}_2\text{O}$ has been redetermined for comparison with the previous cobalt structure and the nickel structure. Refinement including hydrogen atoms converges with $R = 0.0258$ for 1018 observed data (crystal data is given in Table 4.1). The structure has the same features as the isomorphous nickel compound, *i.e.* the Co-OH_2 distances are nonequivalent at 2.079(2) and 2.117(2) Å (19 σ different), and the water molecules engage in the same hydrogen bonding that furthermore provides understanding of why they are different through analysis of the nonequivalent hydrogen bonding as shown in Figure 4.3. Fractional orthorhombic coordinates and equivalent isotropic atomic displacement parameters are given in Table 4.7 and anisotropic atomic displacement parameters are given in Table 4.8. Selected interatomic bond lengths and bond angles are given in Table 4.9 and hydrogen bond parameters are given in Table 4.10.

Table 4.7. Fractional Orthorhombic Coordinates and Isotropic Atomic Displacement Parameters for $\text{CoV}_2\text{O}_6 \cdot 2\text{H}_2\text{O}$

Atom	x	y	z	Ueq(Å ²)
Co	0.0160(1)	1/4	0.9599	0.0098(1)
V	0.1952(1)	0.5311	0.8260	0.0086(1)
O1	0.1671(3)	0.3806(2)	0.8546(1)	0.0185(3)
O2	0.1212(3)	0.6136(2)	0.9363(1)	0.0203(3)
O3A	-0.3024(4)	0.265	0.8696(2)	0.0165(5)
H2A	-0.429(4)	0.291(3)	0.901(2)	0.025
H3A	-0.302(4)	0.291(3)	0.803(2)	0.025
O3B	-0.3024(4)	0.235	0.8696(2)	0.0165(5)
H2B	-0.429(4)	0.209(3)	0.901(2)	0.025
H3B	-0.302(4)	0.209(3)	0.803(2)	0.025
O4	0.0003(3)	0.5710(2)	0.7103(1)	0.0168(3)
O5	0.3407(4)	1/4	1.0523(2)	0.0181(4)
H1	0.387(6)	0.314(2)	1.095(3)	0.027(8)

Table 4.8. Anisotropic Atomic Displacement Parameters for $\text{CoV}_2\text{O}_6 \cdot 2\text{H}_2\text{O}$.

Atom	U ₁₁	U ₂₂	U ₃₃	U ₁₂	U ₁₃	U ₂₃
Co	0.0107(2)	0.0097(2)	0.0089(2)	0	0.0014(1)	0
V	0.0078(2)	0.0091(2)	0.0087(2)	-0.0005(1)	0.0012(1)	-0.0004(1)
O1	0.0236(8)	0.0122(7)	0.0197(7)	-0.0007(6)	0.0051(6)	0.0034(6)
O2	0.0211(8)	0.0208(8)	0.019(1)	0.0014(6)	0.0062(6)	-0.0069(6)
O4	0.0102(7)	0.0224(8)	0.0179(7)	-0.0035(6)	-0.0033(5)	0.0053(6)
O5 _w	0.016(1)	0.019(1)	0.019(1)	0	-0.0065(8)	0

Table 4.9. Selected Interatomic Distances and Angles for $\text{CoV}_2\text{O}_6 \cdot 2\text{H}_2\text{O}$.

CoO ₆ octahedron					
Co–O1	2.055(2)		O1–Co–O1'	85.72(9)	
Co–O2	2.057(2)		O1–Co–O2	91.92(7)	
Co–O3	2.079(2)		O1–Co–O2'	177.18(7)	
Co–O5	2.117(2)		O1–Co–O3	89.10(7)	
			O1–Co–O5	87.96(7)	
			O1'–Co–O2	177.18(7)	
			O1'–Co–O2'	91.92(7)	
			O1'–Co–O3	95.13(7)	
			O1'–Co–O5	87.96(7)	
			O2–Co–O2'	90.4(1)	
			O2–Co–O3	86.36(7)	
			O2–Co–O5	90.43(7)	
			O2'–Co–O3	92.64(7)	
			O2'–Co–O5	90.43(7)	
			O3–Co–O5	175.57(1)	
VO ₄ tetrahedron					
V–O2'	1.632(2)		O1–V–O2'	109.79(8)	
V–O1	1.653(2)		O1–V–O4	109.27(8)	
V–O4	1.802(2)		O1–V–O4'	111.63(8)	
V–O4'	1.806(1)		O2'–V–O4	109.29(8)	
			O2'–V–O4'	107.54(8)	
			O4–V–O4'	109.29(5)	

Table 4.10. Hydrogen Bonding of $\text{Co}_2\text{O}_6 \cdot 2\text{H}_2\text{O}$.

D–H	d[D–H];(Å)	d[H···A];(Å)	<DHA;(°)	d[D···A];(Å)	A
O3–H2	0.842	2.252	139.68	2.947	O5 ^(I)
O3–H2	0.843	2.255	139.47	2.947	O5 ^(I)
O3–H3	0.843	2.102	170.93	2.938	O1 ^(II)
O3–H3	0.843	2.102	170.94	2.938	O1 ^(III)
O5–H1	0.884	1.951	168.78	2.823	O4 ^(IV)

Symmetry codes: (I) $x-1, y, z$; (II) $x-1/2, y, -z+3/2$; (III) $x-1/2, -y+1/2, -z+3/2$; (IV) $-x+1/2, -y+1, z+1/2$.

The bond valence data in Table 4.11 include hydrogen bond contributions as noted before and show that the metal valence states are Co^{+2} and V^{+5} similar to the valence states in $\text{NiV}_2\text{O}_6 \cdot 2\text{H}_2\text{O}$.

Table 4.11. Bond Valence Sums for Atoms in $\text{CoV}_2\text{O}_6 \cdot 2\text{H}_2\text{O}$.

	O1	O2	O4	O3 _w	O5 _w	S _{CAL}	S _{THEO}
Co	(0.375x2)	(0.373x2)		0.351	0.317	2.164	2
V	1.5	1.588	(1.003,0.995)			5.05	5
H1			0.18		(0.82x2)		1
H2				0.87	0.13		1
H3	(0.135)			0.865			1
S _{CAL}	2.010	1.961	2.175	2.086	2.087		
S _{THEO}	2	2	2	2	2		

The room temperature structure of the isomorphous manganese compound, $\text{MnV}_2\text{O}_6 \cdot 2\text{H}_2\text{O}$, has also been reported (Liao, Drezen, Leroux, Guyomard & Piffard, 1996) with $Z = 4$, $a = 6.075(4)$, $b = 10.909(1)$, $c = 12.030(2)$ Å, $R_1 = 0.024$ for the observed data, and goodness of fit = 3.44. Hydrogen atoms on the water molecules were not located. The structure consists of MnO_6 octahedra and VO_4 tetrahedra with nonequivalent Mn-O_w bonds of 2.161(2) and 2.199(2) Å (19σ different) in the axial positions of the manganese octahedra with both water molecule oxygen atoms on the mirror plane and a large anisotropic thermal parameter perpendicular to the mirror plane for O3 (magnitude of 0.050(1)Å²). They reported TGA and DSC results which showed a two step dehydration process, the first one at ~170 °C corresponding to weight loss of ~1.6 water molecules per formula unit and the second dehydration step at ~240 °C. The thermodiffraction experiment indicated that the compound lost crystallinity gradually at 150 °C but they but the authors did not attempt to explain why there are two steps in TGA dehydration experiment. Their DSC curve does not show clear separation of the various thermal phenomena which occur during these dehydration transition processes.

At the time the current $\text{NiV}_2\text{O}_6 \cdot 2\text{H}_2\text{O}$ results were first presented (Chatkon & Haller, 2000) another report appeared in the literature (Baudrin, Touboul &

Nowogrocki, 2000) on " α -Ni(VO₃)₂·2H₂O" with R₁ = 0.017 for the observed data. The authors synthesized the compound using a *chimie douce* process with 24 h reaction time at 150 °C under 20 bar of argon. Their cell parameters, $a = 5.530(1)$, $b = 10.621(10)$ Å , $c = 11.756(5)$ Å indicate, and their structure confirms, they have prepared the same compound reported hePrein. The structure consists of NiO₆ octahedra and VO₄ tetrahedra with nonequivalent Ni-Ow bonds of 2.161(2) and 2.199 (2) Å for the water molecules coordinated in the axial positions of the nickel octahedra. The hydrogen atoms on the water molecules were located by Fourier difference electron density synthesis. The nickel atom, the two axial water oxygen atoms, and the hydrogen atoms of O3 are all located on the mirror plane, but the magnitude of the anisotropic atomic displacement parameter of O3 perpendicular to the mirror plane was 0.045 Å² which is large relative to the amplitudes of the atomic displacement parameters of other atoms in the structure. They did not resolve the disorder of the O3w water molecule.

They did however report the water molecules engage in the same hydrogen bonding described above for NiV₂O₆·2H₂O and used the valence bond model to confirm their hydrogen bond determination showing the oxidation states of Ni = +2, V = +5, and around -2 for all the oxygen atoms in the compound. Their bond valence results are shown in Table 4.12 which can be compared with Table 4.6, the bond valence calculation of NiV₂O₆·2H₂O in the current determination.

Table 4.12. Bond Valence Sums for Atoms in α -Ni(VO₃)₂·2H₂O.

	O1	O2	O4	O3 _w	O5 _w	S _{CAL}	S _{THEO}
Ni	(.36x2)	(.367x2)		0.36	0.34	2.14	2
V	1.53	1.62	(1.01 ,1.01.)			5.17	5
H1			0.125		(0.875x2)		1
H2				0.91	0.09		1
H3	(0.13)			0.87			1
S _{CAL}	1.96	1.98	2.15	2.14	2.18		
S _{THEO}	2	2	2	2	2		

From the three isomorphous structures of MV₂O₆·2H₂O (M = Mn²⁵, Co²⁷, Ni²⁸) the d[M²⁺-O] bond lengths decrease with increasing atomic number (increasing

nuclear charge) in agreement with the observed ionic radii in octahedral oxygenate environments $\text{Ni}^{2+} = 0.690 \text{ \AA}$, $\text{Co}^{2+} = 0.745 \text{ \AA}$ and $\text{Mn}^{2+} = 0.830 \text{ \AA}$ (Shannon, 1976).

4.5. FTIR Experiment

Figure 4.7 shows the FTIR spectrum of $\text{NiV}_2\text{O}_6 \cdot 2\text{H}_2\text{O}$. Examination of the water O–H stretching region of about $3200\text{--}3500 \text{ cm}^{-1}$ reveals three distinct types of water OH groups. Additional data is needed to unambiguously assign these bands. The two bands at 3436.8 and 3494.2 cm^{-1} are quite sharp and the band at 3284.6 cm^{-1} is broad, perhaps suggesting the former represent the OH that are hydrogen bonded to the framework and the latter the OH that is shared between two waters. On the other hand the 3285.6 cm^{-1} band being at lowest energy could correspond to the strongest hydrogen bonds, those being the $\text{O5-H}\cdots\text{O4}$ bonds. This band is also the strongest of the three suggesting it could represent the pair of $\text{O5-H}\cdots\text{O4}$ bonds, while the weaker bands could represent the single interactions $\text{O3-H}\cdots\text{O5}$ and $\text{O3-H}\cdots\text{O1}$. No attempt has been made to assign the lower energy bands.

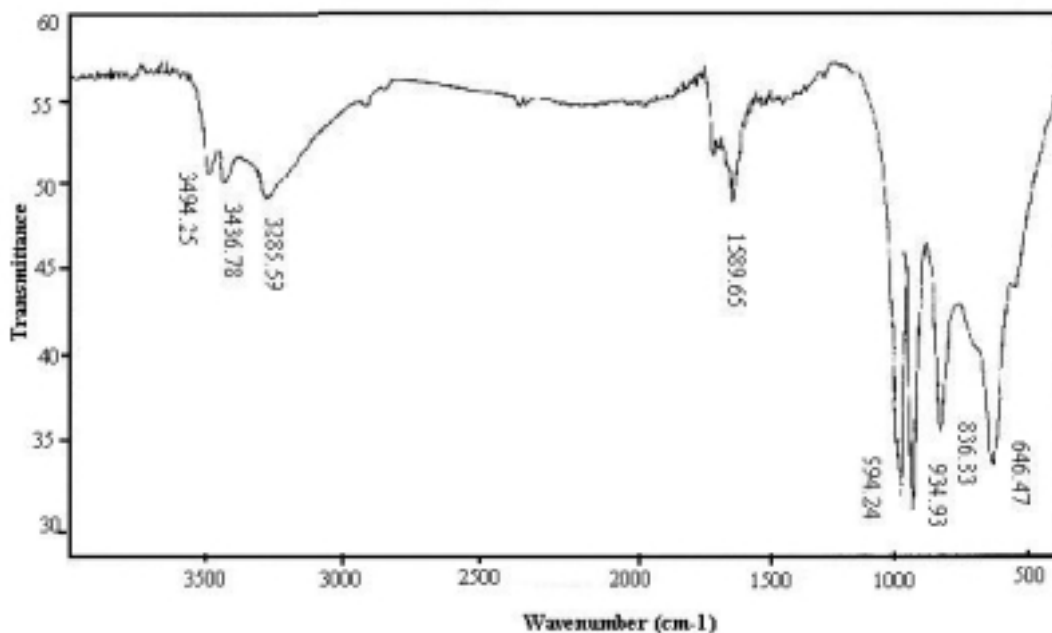


Figure 4.7. FTIR Spectrum of $\text{NiV}_2\text{O}_6 \cdot 2\text{H}_2\text{O}$.

4.6 Thermal Analysis: Dehydration

Hydrothermal preparation gave a mixture of green crystals of $\text{NiV}_2\text{O}_6 \cdot 2\text{H}_2\text{O}$ with a minor phase of orange crystals. Green crystals were separated from the mixture to create a phase pure sample under an optical stereomicroscope. The unit cell of a single crystal was determined to verify the green material is $\text{NiV}_2\text{O}_6 \cdot 2\text{H}_2\text{O}$. The results of TGA are given in Figure 4.8 and of DSC in Figure 4.9.

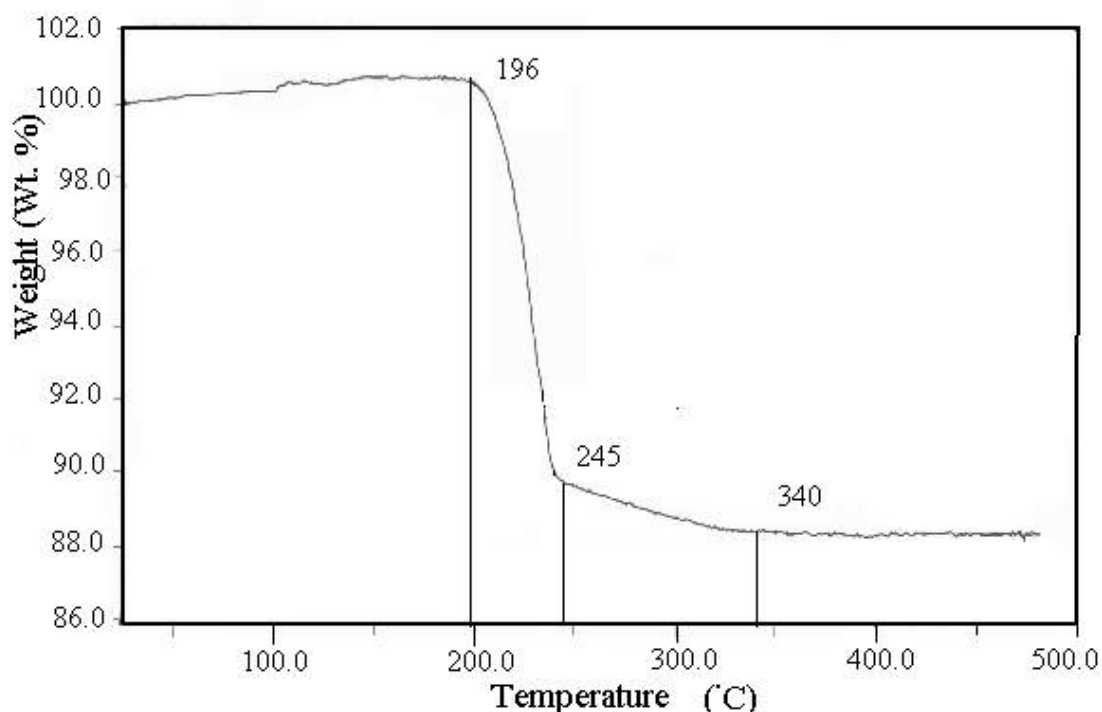


Figure 4.8. TGA Curve of $\text{NiV}_2\text{O}_6 \cdot 2\text{H}_2\text{O}$ ($1\text{ }^\circ\text{C min}^{-1}$).

TGA (heating rate, $\Delta T = 1\text{ }^\circ\text{C/min}$) and DSC (heating rate, $\Delta T = 5\text{ }^\circ\text{C min}^{-1}$) analyses indicated a dehydration process occurring in two stages consistent with the results reported for the isomorphous cobalt (Murashova, Velikodnyi, Potapov & Trunov, 1986) and manganese (Liao, Drezen, Leroux, Guyomard & Pifear, 1996) compounds. A two step dehydration process was reported for the cobalt compound, but details of the process were not given. The first dehydration occurred in the range 196-245 °C showing a weight loss of 10.5% or 1.70 water molecules per formula unit. This is in good agreement with the observations for the manganese compound where

the first dehydration process occurred in the range 170-220 °C with a loss of 1.6 water molecules per formula unit by an endothermic process. The DSC result appears to have a falling baseline in the region below 230 °C and it is difficult to be certain if the first dehydration process is endothermic or not. The second dehydration process occurs in the range of 245-340 °C showing a weight loss of 1.4% or 0.23 water molecules per formula unit by an endothermic process, also in good agreement with the observations for the manganese compound (220-240 °C, -0.4 H₂O). The two dehydration processes together thus account for loss of both of the coordinated water molecules.

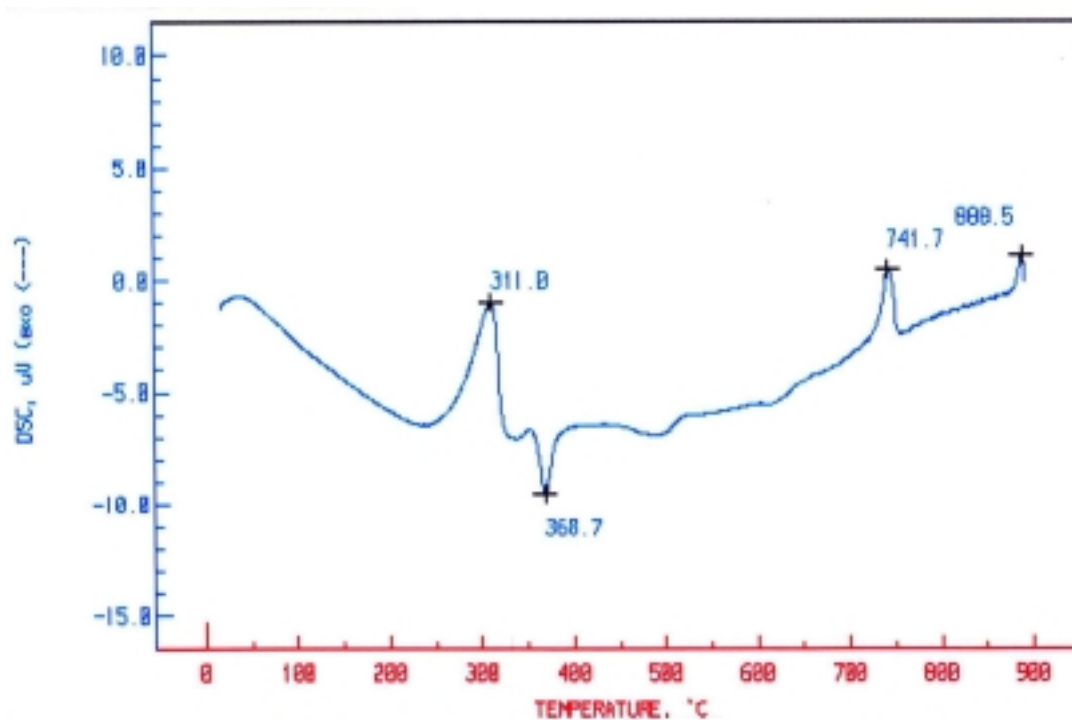


Figure 4.9. DSC Curve of NiV₂O₆•2H₂O (5 °C min⁻¹).

Thermodiffraction (Figure 3.4 and Table 4.13) shows the 25 °C phase to be mixed with a minor phase in the sample after it has been heated to 200 °C then cooled. As the first dehydration has just begun at 200 °C it is presumed that the new phase is the monohydrated intermediate proposed but not observed by Liao and coworkers (1996) for the analogous manganese compound. A sample heated to 280 °C, beyond the end of the first dehydration process, then cooled no longer shows peaks due to the 25 °C phase nor peaks due to the proposed monohydrated

intermediate phase. There are two weak peaks of a new phase but there is not sufficient information to assign them to a particular phase.

Table 4.13. XRD Results for $\text{NiV}_2\text{O}_6 \cdot 2\text{H}_2\text{O}$.

Temperature (°C)	Angle 2-Theta (°)	d value (Å)	Intensity count	Intensity %
25	16.652	5.322	4.19	1.6
	22.498	3.948	254	100
	26.241	3.390	38.1	15
	58.416	1.578	10.2	4.0
200	16.146	5.493	20.6	1.3
	22.520	3.949	1546	100
	26.238	3.394	54.4	3.5
	58.430	1.577	85.8	5.5
280	22.430	3.960	126	100
	33.620	2.663	19.9	15.8
330	22.611	3.804	5.09	100
	24.260	3.679	5.09	99.9
450	8.961	9.861	5.04	70.5
	11.241	7.623	5.06	70.9
	19.938	4.444	7.14	100
	36.154	2.479	6.12	85.6
800	11.481	7.638	27.2	100
	23.299	3.814	8.10	29.8
	33.259	2.690	6.15	22.6
	56.723	1.621	6.22	22.9
900	11.691	7.603	60.7	100
	15.559	5.681	8.74	14.4
	20.270	4.375	25.7	42.4
	31.431	28.43	28.3	46.7

Lack of a stable crystal lattice for the monohydrated intermediate phase may explain the loss of more than one water in the first process. Loss of the first water molecule may allow the local structure to shift in such a way that the second water environment is changed allowing it to dissociate as easily or more easily than the first water. Another possibility is suggested by the fact that in the analogous $\text{CuV}_2\text{O}_6 \cdot 2\text{H}_2\text{O}$

compound (Leblanc & Ferey, 1990), which while not isomorphous does have a similar structure, the two water molecules have identical environments.

A more probable explanation comes from the hydrogen bond analysis above (see Figure 4.3 and text). O5w is held in the lattice by one coordination bond and three hydrogen bonds, while O3w is held by only one coordination bond and two hydrogen bonds. Therefore, one would expect O3w to dissociate preferentially. When O3w dissociates the O3w–H···O5w hydrogen bond to the interrelated O5w is also lost leaving that O5w water molecule with only one coordination bond and two hydrogen bonds, *i.e.* the same number and type of bonds as the remaining O3w water molecules. Thus, the binding energy for an O5w water molecule in a pore from which O3w has been removed will be lowered and will be near the binding energy of O3w, leading to dissociation of both water molecules in the same dehydration wave. At some point, apparently when about 1.7 of the 2.0 water molecules have dissociated, the integrity of the lattice is lost. The resulting rearrangement of the lattice stabilizes the remaining water molecules somewhat leading to the second dehydration wave. The dramatic change in the baseline slope at the end of the dehydration process indicates quite different heat capacity of the material after the loss of water.

Samples heated to 330 °C or to 450 °C and cooled gives powder diffraction spectra characteristic of amorphous materials. Apparently, as the dehydration proceeds the structure cannot support itself and collapses. Similarly, amorphous nature is reported for the cobalt compound for 270 °C and higher. In contrast however, the manganese compound exhibits two distinct crystalline dehydrated phases, an α -phase at 270 °C (the end of the dehydration range) and a β -phase above 320 °C. The authors were attempting to solve the structures, but no further report has appeared to date.

As the temperature is increased, several peaks, some endothermic and some exothermic, occur in the DSC. The slope of the base line changes several times indicating changes in heat capacity and thus in compound or phase. Also, the TGA (Figure 3.3) from 745 °C to 900 °C (the maximum temperature studied) shows a slow weight loss accumulating to 1.58%. The XRD at 800 °C shows a new phase and at 900 °C yet another new phase. The rich solid state chemistry indicated by these observations is left for others to study.

Chapter V



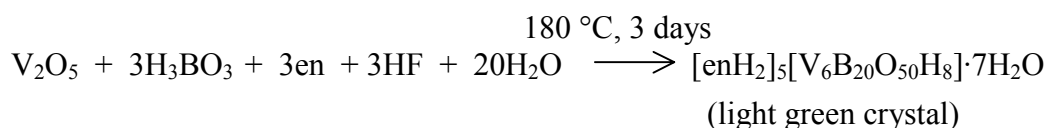
5.1 Introduction

The utilization of hydrothermal technique in combining anionic inorganic species with cationic organic templates has been used extensively in the syntheses of transition metal oxide composition materials such as polyoxovanadates that have applications in catalysis and solid state devices such as electrolytic cells or magnetic materials. The nature of hydrothermal synthesis often leads to materials which use noncovalent bonds to form extended network supramolecular structures, another area of considerable current interest.

Polyoxovanadium borates are a largely unexplored subset of the polyoxovanadates. The few structurally characterized materials exhibit radically different structure types, each characterized by a different polyvanadate moiety associated with a different polyborate moiety. A general characteristic of the materials seems to be the formation of microporous structures. The metal-metal interactions in the oxo-clusters range from virtually no bond to very strong bonds. The cationic organic moieties provide charge balance, and together with water molecules, fill the spaces between the clusters in extensive hydrogen bonded three dimensional supramolecular network structures.

5.2. Experimental

The single crystal selected for x-ray data collection was provided as a mounted sample by Dr. Ian D. Williams, Hong Kong University of Science and Technology. It was synthesized by hydrothermal reaction as part of a study of organically templated supramolecular materials.



where the coefficients of the reactants show the ratio of materials placed in the reaction bomb and not the stoichiometry of the reaction.

A light green sample crystal having dimensions, 0.20 x 0.25 x 0.32 mm, was mounted on the end of a solid glass fiber with epoxy cement. Preliminary examination and data collection were carried out on an Enraf-Nonius KappaCCD diffractometer equipped with a fine focus molybdenum anode ($\lambda_{\text{MoK}\alpha} = 0.71073 \text{ \AA}$) x-ray tube powered at 40 kV and 25 mA, a graphite crystal monochromator, a 0.5 mm *ifg* capillary collimator, and an Oxford Cryosystems 600 low temperature device operating at 200 K. Preliminary examination established a *C* centered monoclinic unit cell for which eight series of omega scans with total scan length of 602.4 ° were created in response to the design goal of four times redundancy on at least 90 % of the collected data. Data were collected at a scan rate of 8.0 °/min as four series of omega scans each divided into steps 2.0 ° in thickness using the COLLECT routine (Nonius BV, 2000). The three dimensional data were extracted from the scans and corrections for Lorentz and polarization effects applied with the Denzo/Scalepack (Otwinowski & Minor, 1997) software package which produces properly scaled reduced data from the three dimensional scan data. Absorption corrections were applied to the intensity data from symmetry related reflections using the multiscan technique implemented in the SORTAV routine (Blessing, 1995, 1997) of the MaXus package (Mackay, Gilmore, Edwards, Tremayne, Stuart & Shankland, 1998).

Initial coordinates for the three crystallographically unique vanadium heavy atoms were located by Patterson interpretation. The ten boron and twenty-five oxygen cluster atoms were located from an electron density difference map phased on the vanadium positions. The cluster was refined assuming isotropic atomic displacement parameters. The boron and oxygen atom assignments were verified based on the magnitudes of the isotropic thermal parameters and chemical considerations. An electron density difference map based on the isotropic atom cluster model was not easy to interpret so the model was improved, first, by additional refinement of the cluster assuming anisotropic atomic displacement parameters and second, by locating the four hydrogen atoms of the cluster -OH groups using ring Fourier calculations and including these hydrogen atoms in the least-squares refinement as isotropic contributors. The ring Fourier calculation helps locate the maximum electron density around the circular section which represents the best possible hydrogen positions for a

fixed suitable O-H distance and B-O-H angle (see Appendix C for a more complete description of ring Fourier calculations).

Considerable effort was required to locate the cationic ethylenediammonium (enH_2)²⁺ counter ions and the oxygen atoms of the waters of crystallization. The coordinates of these atoms were located from a series of electron density difference maps alternating with least squares refinement cycles to verify occupancies and to include additional information in the model to sharpen the maps and thus reveal more positions. The two and one half independent ethylenediammonium molecules exhibit considerable disorder. Therefore, the C-H bond lengths were constrained to be equivalent as were the C-N bond lengths, while N-C-C angles were restrained to be similar. Anisotropic atomic displacement parameters were used when possible, but isotropic atomic displacement parameters were used for badly overlapped and low occupancy atoms.

As the model improved, ring Fourier calculations were carried out on the remaining nitrogen positions to distinguish between the two possibilities; ammonium or amine. Hydrogen atom positions found in this way verified that the nitrogen atoms are ammonium and not amine nitrogens. The hydrogen atoms thus located were included in the model as idealized C_{3v} groups with fixed N-H bond lengths of 0.86 Å and isotropic atomic displacement parameters 10% larger than the isotropic equivalent of the parameters for the nonhydrogen atom to which each is attached. Each C_{3v} group was allowed one degree of freedom, namely rotation about the C-N bond axis.

Water oxygen atoms were assigned occupancy factors based on proximity to ethylenediammonium cations and other water molecules. The sum of the occupancies of the six independent positions is 3.5 giving 7 waters per cluster. Anisotropic atomic displacement parameters were utilized for all six independent water positions, but because of fractional occupancies and disorder the water hydrogen atoms were not located.

The final model, refined with SHELXTL, included anisotropic displacement parameters on all nonhydrogen atoms except C52 (occupancy = 0.15). The hydrogen atoms on the cluster and those described above for the ethylenediammonium cations were included as idealized riding contributions with fixed distances as appropriate for the type of group, and isotropic atomic displacement parameters 10% larger than the isotropic equivalent of the parameters for the nonhydrogen atom to which each is

attached. The final values for the discrepancy indices were $R = 0.048$ and $R_w = 0.177$ and goodness of fit = 1.154. The two highest peaks on the final difference electron density Fourier map (2.34 and $1.92 \text{ e } \text{\AA}^{-3}$) were located near the center of the cluster as might be expected from the pseudo symmetry of the problem and the difficulty in resolving the disordered cation/solvate region. Attempts to model these peaks and refine them resulted in unreasonable occupancies or atomic displacement parameters so they were not included in the final refinement model. The next highest peak on the map was $1.09 \text{ e } \text{\AA}^{-3}$ and the maximum negative peak was $1.02 \text{ e } \text{\AA}^{-3}$. The estimated error of the map was $0.18 \text{ e } \text{\AA}^{-3}$.

Crystal data and refinement details for $[\text{enH}_2]_5[\text{V}_6\text{B}_{20}\text{O}_{50}\text{H}_8] \cdot 7\text{H}_2\text{O}$ are given in Table 5.1, fractional monoclinic crystal coordinates and equivalent isotropic atomic displacement parameters are given in Table 5.2, and selected distances and angles are given in Table 5.3.

Table 5.1. Crystal Data for $[\text{enH}_2]_5[\text{V}_6\text{B}_{20}\text{O}_{50}\text{H}_8]\cdot 7\text{H}_2\text{O}$.

Empirical formula	$[\text{enH}_2]_5[\text{V}_6\text{B}_{20}\text{O}_{50}\text{H}_8]\cdot 7\text{H}_2\text{O}$
Formula weight (Daltons)	1766.6
Crystal system & Space group	monoclinic C2/c (No. 15)
Unit cell parameters	
a (Å)	20.0513(2)
b (Å)	13.4444(1)
c (Å)	21.6003(2)
β (deg)	97.332°
V (Å ³)	5775.3
Cell parameters from	
Z	4
d_{calc} (Mg m ⁻³)	2.04
Radiation type & wavelength (Å)	Mo K α ($\lambda = 0.71073$)
Absorption coefficient, μ (mm ⁻¹)	1.05
Temperature (K)	200
Crystal shape	
Crystal size (mm)	0.20 x 0.25 x 0.32
Color	light green
Diffractometer	Nonius KappaCCD
Absorption corrections	Multiscan
Measured reflections	
Independent data	8425
$F^2 > 2\sigma(F^2)$	7105
R_{merge}	
$2\theta_{\text{max}}$	60.0
h range	0 to 28
k range	0 to 18
l range	-30 to 30
Refinement on	F^2
$R[F^2 > 2\sigma(F^2)]$	0.048
$wR(F^2)$	0.177
Goodness of fit	1.154
weights, $w =$	
$\Delta\rho_{\text{max}}$, $\Delta\rho_{\text{min}}$, Estimated error (e Å ⁻³)	2.34/-1.02/0.13
Structure refinement program	SHELXL
Atomic scattering factors from	Hahn, 1992, Vo

Table 5.2. Fractional Monoclinic Coordinates and Equivalent Atomic Displacement Parameters^a for [enH₂]₅[V₆B₂₀O₅₀H₈]·7H₂O

Atom	x	y	z	U_{eq}
V1	0.1750	0.4371	0.5286	0.0161(1)
O11	0.1359(1)	0.5394(2)	0.5424(1)	0.0269(5)
O3	0.1792(1)	0.4269(2)	0.4398(1)	0.0200(4)
O8	0.2687(1)	0.4725(2)	0.5221(1)	0.0198(4)
V2	0.2744	0.4429	0.4343	0.0172(1)
O21	0.2834(1)	0.5447(2)	0.3961(1)	0.0287(5)
O5	0.2714(1)	0.3318(2)	0.3763(1)	0.0186(4)
O9	0.3602(1)	0.3760(2)	0.4582(1)	0.0185(4)
V3	0.3521	0.2566	0.4063	0.0156(1)
O31	0.4071(1)	0.2663(2)	0.3584(1)	0.0289(5)
O2	0.3890(1)	0.1741(2)	0.4777(1)	0.0172(4)
O6	0.2982(1)	0.1348(2)	0.3944(1)	0.0171(4)
B1	-0.0171(2)	0.1818(3)	0.4984(2)	0.0212(6)
O1	-0.0809(1)	0.1693(2)	0.5150(1)	0.0269(5)
H1	-0.0853(7)	0.1118(9)	0.5264(19)	0.0296
O12	-0.0002(1)	0.2741(2)	0.4794(1)	0.0227(4)
B2	0.0679(2)	0.2955(3)	0.4654(1)	0.0191(6)
O23	0.0653(1)	0.3677(2)	0.4164(1)	0.0214(4)
O29	0.0973(1)	0.1981(2)	0.4426(1)	0.0193(4)
B3	0.1272(2)	0.3871(3)	0.3920(2)	0.0208(6)
O35	0.1541(1)	0.2881(2)	0.3694(1)	0.0197(6)
O34	0.1179(1)	0.45422(2)	0.3386(1)	0.0260(5)
B4	0.1572(2)	0.4492(3)	0.2915(2)	0.0245(7)
O4	0.1533(1)	0.5281(2)	0.2508(1)	0.0300(5)
H4	0.1856(12)	0.5269(19)	0.2311(15)	0.0330
O45	0.1978(1)	0.3700(2)	0.2835(1)	0.0251(5)
B5	0.2150(2)	0.2965(3)	0.3330(2)	0.0196(6)
O56	0.2264(1)	0.2012(2)	0.3069(1)	0.0201(4)
B6	0.2377(2)	0.1209(3)	0.3505(2)	0.0192(8)
O68	0.1775(1)	0.1150(2)	0.3879(1)	0.0203(4)
O67	0.2409(1)	0.0264(2)	0.3175(1)	0.0225(7)
B7	0.2153(2)	-0.0603(3)	0.3384(2)	0.0251(7)
O7	0.2241(2)	-0.1479(2)	0.3080(2)	0.0445(7)
H7	0.2547(17)	0.1415(12)	0.2864(18)	0.0489
O78	0.1803(1)	-0.0646(2)	0.3884(1)	0.0261(5)
B8	0.1742(2)	0.0217(3)	0.4281(2)	0.0204(6)
O89	0.1103(1)	0.0203(2)	0.4519(1)	0.0220(4)
B9	0.0934(2)	0.1075(3)	0.4853(2)	0.0198(6)
O91	0.0247(1)	0.1019(2)	0.5003(1)	0.0223(4)
B10	0.1242(2)	0.1910(3)	0.3818(2)	0.0226(6)
O10	0.0727(1)	0.1646(2)	0.3327(1)	0.0256(5)
H10	0.0567(15)	0.2152(2)	0.3156(13)	0.0282
N2	0.3400(2)	0.6555(3)	0.3062(1)	0.0348(7)
H2A	0.3110(9)	0.6372(9)	0.3320(10)	0.0382
H2B	0.3181(10)	0.6658(15)	0.2682(3)	0.0382
H2C	0.3606(2)	0.7113(6)	0.3201(13)	0.0382
C2	0.3901(2)	0.5765(3)	0.3033(2)	0.0413(9)
H2D	0.4208(2)	0.5969(3)	0.2744(2)	0.0454
H2E	0.3671(2)	0.5170(3)	0.2864(2)	0.0454
C11	0.4308(5)	0.5506(11)	0.3649(3)	0.0408(34)

Table 5.2. -- continued.

Atom	x	y	z	U_{eq}
H11A	0.4399(5)	0.6118(11)	0.3882(3)	0.0449
H11B	0.4028(5)	0.5097(11)	0.3882(3)	0.0449
N11	0.4949(5)	0.4986(8)	0.3636(4)	0.0448(21)
H11A	0.519(15)	0.5028(44)	0.4010(10)	0.0493
H11B	0.5173(15)	0.5266(33)	0.3351(27)	0.0493
H11C	0.4870(5)	0.4350(14)	0.3539(31)	0.0497
C12	0.4345(6)	0.5801(7)	0.3653(4)	0.0302(29)
H12A	0.4690(6)	0.6303(7)	0.3638(4)	0.0333
H12B	0.4077(6)	0.5983(7)	0.3979(4)	0.0333
N12	0.4661(6)	0.4831(6)	0.3796(5)	0.0590(30)
H12A	0.4345(7)	0.4361(11)	0.3769(40)	0.0649
H12B	0.4881(37)	0.4841(22)	0.4181(16)	0.0649
H12C	0.4948(33)	0.4702(30)	0.3524(26)	0.0649
C3	1/2	0.4468(9)	1/4	0.0982(35)
C4	0.5461(5)	0.4104(6)	0.3058(4)	0.1431(40)
N4	0.5101(4)	0.3150(6)	0.3008(4)	0.0567(20)
N5	0.3247(2)	0.8060(2)	0.5482(2)	0.0411(8)
H5A	0.3335	0.8110	0.5890	0.05
H5B	0.3284	0.8615	0.5264	0.05
H5C	0.3552	0.7620	0.5384	0.05
C51	0.2567(2)	0.7641(3)	0.5341(1)	0.0377(10)
H51A	0.2238(2)	0.8127(3)	0.5437(1)	0.0414
H51B	0.2526(2)	0.7057(3)	0.5598(1)	0.0415
C52	0.2735(10)	0.7918(16)	0.4939(6)	0.0515(70)
H52A	0.2953(10)	0.7763(16)	0.4575(6)	0.0566
H52B	0.2481(10)	0.8528(16)	0.4856(6)	0.0566
O42	0.3598(2)	0.8019(3)	0.6800(2)	0.0609(10)
O9F	0.3009(13)	0.8074(18)	0.6629(13)	0.1191(85)
O41	0.4082(2)	0.8282(3)	0.3674(2)	0.0609(10)
O54	-0.0150(5)	0.3058(9)	0.2626(5)	0.0592(28)
N7	0.4973(4)	-0.0278(6)	0.5505(4)	0.0514(20)
C7	0.4802(8)	-0.0954(11)	0.5993(5)	0.056(4)
H7A	0.4872(8)	-0.1639(11)	0.5876(5)	0.056
H7B	0.4334(8)	-0.0873(11)	0.6053(5)	0.056
C8	0.5253(8)	-0.0610(9)	0.6587(6)	0.1069(64)
N81	0.5188(9)	0.0165(19)	0.6987(11)	0.0910(89)
N82	0.5026(8)	-0.1432(16)	0.7018(9)	0.0698(59)
O55	-0.0119(8)	0.5517(14)	0.2973(11)	0.0756(57)
O552	0.4699(9)	-0.0895(14)	0.5784(8)	0.0913(42)

^a Numbers given in parentheses are the estimated standard deviations in the least significant digits.

Table 5.3. Selected Interatomic Bond Distances (Å) and Angles (deg) for the $[\text{V}_6\text{B}_{20}\text{O}_{50}\text{H}_8]^{-10}$ Cluster.

Central band of cluster			
V3- O31	1.611(2)	V3-V2	3.051(1)
- O5	1.947(2)	-V1	3.041(1)
- O9	1.954(2)	V2-V1	3.027(1)
- O6	1.967(2)	V1-V3'	3.041(1)
- O2	1.631(2)	O5-V3- O9	76.64(9)
V2- O21	1.619(2)	O5-V3-O6	88.25(9)
- O3	1.940 (2)	O6-V3-O2	77.12(8)
- O5	1.945(2)	O9-V3-O2	90.97(8)
- O9	1.952(2)	O6-V3-O31	113.24(11)
- O8	1.955(2)	O5-V3-O31	110.67(10)
V1- O11	1.631(2)	O9-V3-O31	106.81(31)
- O3	1.935 (2)	O2-V3-O31	109.27(10)
- O6'	1.939(2)	V3-O6-B6	126.35(18)
- O8	1.960(2)	V3-O5-B5	126.21(18)
-O2'	1.963(2)		
Raft-like polyborate			
B1- O11	1.360(4)	B10- O10	1.427(4)
- O12	1.363(4)	- O35	1.476(4)
- O91	1.360(4)	- O68	1.472(4)
B2- O12	1.465(4)	O3- B3	1.471(4)
- O23	1.432(4)	O8- B8'	1.471(4)
- O29	1.541(4)	O5- B5	1.454(4)
B3- O23	1.433(4)	O9- B9'	1.453(4)
- O34	1.456(4)	O2- B2'	1.468(4)
- O35	1.538(4)	O6- B6	1.454(4)
B4- O41	1.374(4)	O12- B1	1.363(4)
- O34	1.365(4)	O12- B2	1.465(4)
- O45	1.365(4)	O29- B9	1.536(4)
B5- O35	1.538(3)	O29- B10	1.486(4)
- O45	1.464(4)	O1- H1	0.820
-O56	1.429(4)	O4- H4	0.820
B6- O56	1.431(4)	O7- H7	0.820
- O67	1.463(4)	O10- H10	0.820
- O68	1.539(3)	O1-B1-O91	118.96(28)
B7- O7	1.371(4)	O1-B1-O12	117.52(28)
- O67	1.373(4)	O12-B1-O91	123.50(25)
- O78	1.361(4)	O68-B6-O6	108.05(22)
B8- O68	1.532(4)	O67-B6-O6	110.16(24)
- O78	1.547(4)	O6-B6-O56	112.42(23)
- O89	1.440(4)	O29-B10-O68	107.89(24)
B9- O29	1.536(4)	O35-B10-O68	108.84(23)
- O89	1.441(4)	O10-B10-O68	110.06(26)
- O91	1.455(4)	O29-B10-O35	107.75(25)

^a Numbers given in parentheses are the estimated standard deviations in the least significant digits.

5.3. Structure Description

Single crystal x-ray structure analysis of the complex shows that it consists of anionic vanadium polyborate clusters, $[\text{V}_6\text{B}_{20}\text{O}_{50}\text{H}_8]^{-10}$, hydrogen bonded together into a loose porous three dimensional network. The five ethylene diammonium dications required per cluster for charge balance and seven water solvate molecules per cluster fill the porous lattice and hydrogen bond to the clusters and to each other forming an elaborate three dimensional supramolecular structure.

The cluster can be viewed as having a central V_6O_{18} band made up of six edge sharing VO_5 square-pyramids arranged about an inversion center as shown in Figure 5.1. The six terminal vanadyl $[\text{V}=\text{O}]$ distances range between 1.612-1.632(2) Å and the basal $[\text{V}-\text{O}]$ bond distances range between 1.935-1.968(2) Å, consistent with the average values given for square pyramidal V^{+4}O_5 in Table 1.3. Moreover, valence sum calculations also indicate that all six of the vanadium atoms in the cluster are in the +4 oxidation state. The mean V-V internuclear separation of 3.040(7) Å indicates that there is no significant pairing of adjacent vanadium centers.

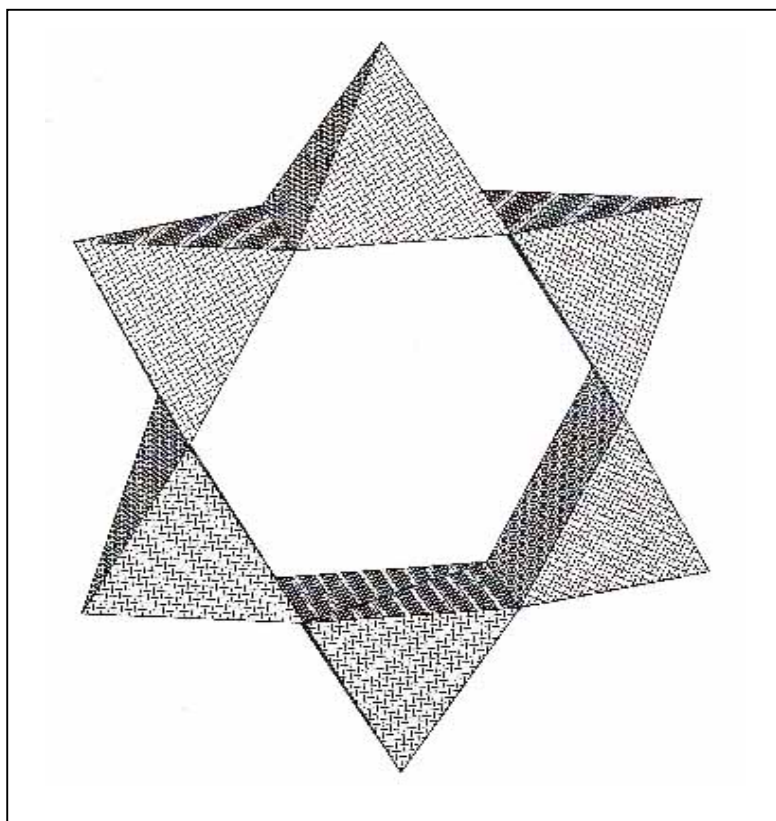


Figure 5.1. Polyhedral Representation of the Central V_6O_{18} Band.

The band is capped above and below by raft like $B_{10}O_{16}H_4$ polyborate triangles as illustrated in Figure 5.2. The central boron atom is bonded tetrahedrally with four oxygen atoms; a terminal 1.432(4) Å B-OH bond, collinear with the pseudo S_6 axis of the cluster and three μ_3 -O each connecting to two additional boron atoms which form a hexagon. The boron atoms of the hexagon are also tetrahedrally bonded with four oxygen atoms. In addition to the μ_3 -O bonds to the central boron, they each form one μ_3 -O bond with one basal oxygen of the vanadyl band (mean $d[B-O] = 1.461(21)$ Å) and one μ_2 -O bond with the adjacent boron of the hexagonal ring that is not already connected by a $B_3\mu_3$ -O bond. The last three boron atoms are arranged trigonally outside the hexagonal ring occupying vertex positions about the hexagonal core connecting pairwise through μ_2 -O bridges to adjacent boron atoms of the hexagon already bonded to the central boron through a μ_3 -O bond; each has a terminal (equatorial) B-OH group with distances in the range $d[B-O_h] = 1.372-1.382(4)$ Å. The individual bond lengths are given in Table 5.3.

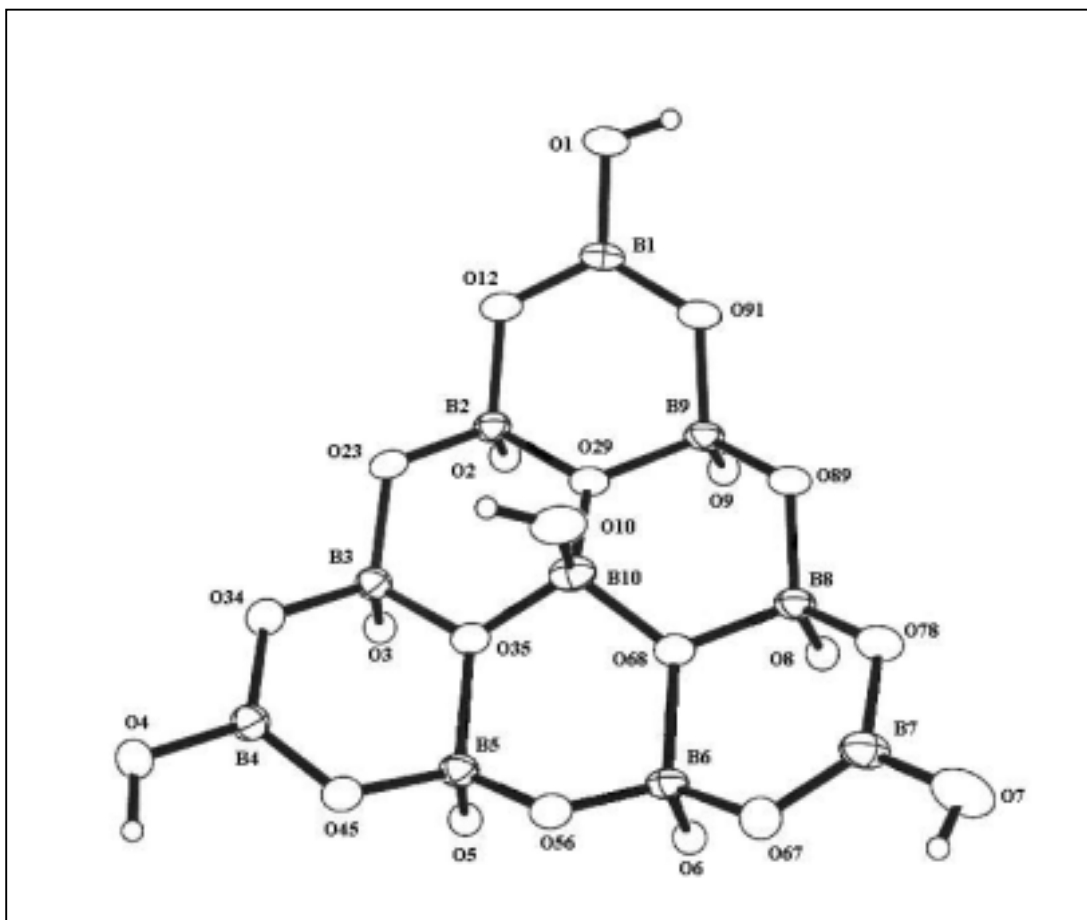


Figure 5.2. The Raft-Like $B_{10}O_{16}H_4$ Polyborate Cap.

The inversion center in the central V_6O_{18} band relates one of the triangular $B_{10}O_{16}H_4$ rafts with a second on the opposite side of the central band, leading to the S_6 cluster illustrated in Figure 5.3.

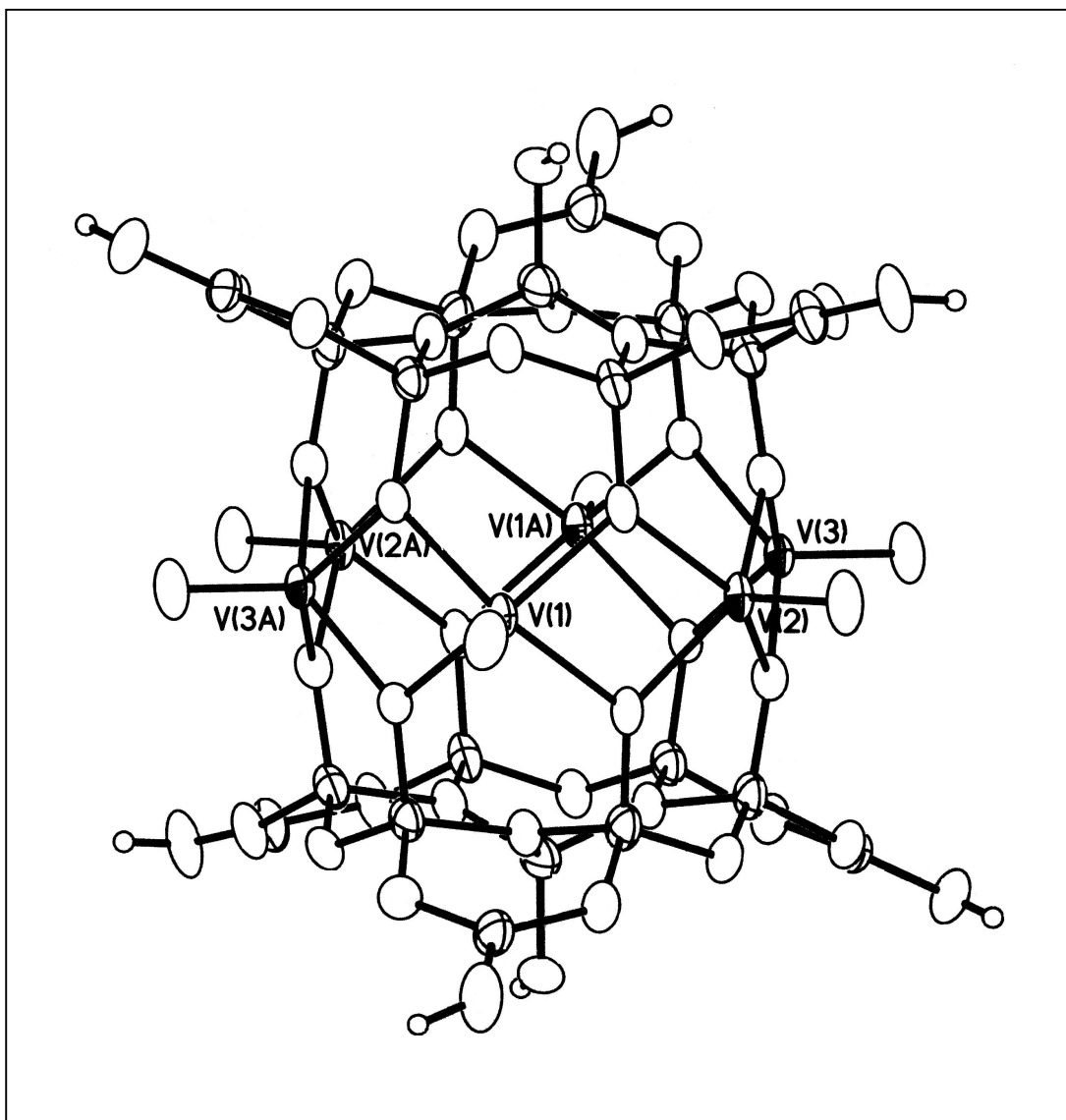


Figure 5.3. $[\text{V}_6\text{B}_{20}\text{O}_{50}\text{H}_8]^{10}$ Cluster.

The cluster hydroxyl hydrogen atoms are ordered and were easily located by use of a Ring Fourier Calculation (see Appendix C). The hydrogen atoms form hydrogen bonds which link the individual clusters into a three dimensional network. Figure 5.4 shows a cluster viewed down the pseudo S_6 axis with three half clusters at the top and to the left of the full cluster. The full cluster extends in front of the plane of the drawing while the half clusters extend behind the plane of the drawing. Two of the hydrogen bond interactions occur between equatorial OH groups on one cluster and the μ_2 -O atoms adjacent to a similar -OH group on the next cluster leading to an 8-connected -B-O-H...O-B-O-H...O- ring. Two of these interactions occur to each

$B_{10}O_{16}H_4$ raft as seen in the two interactions to the left of the cluster in Figure 5.4. Hydrogen bond parameters are given in Table 5.4.

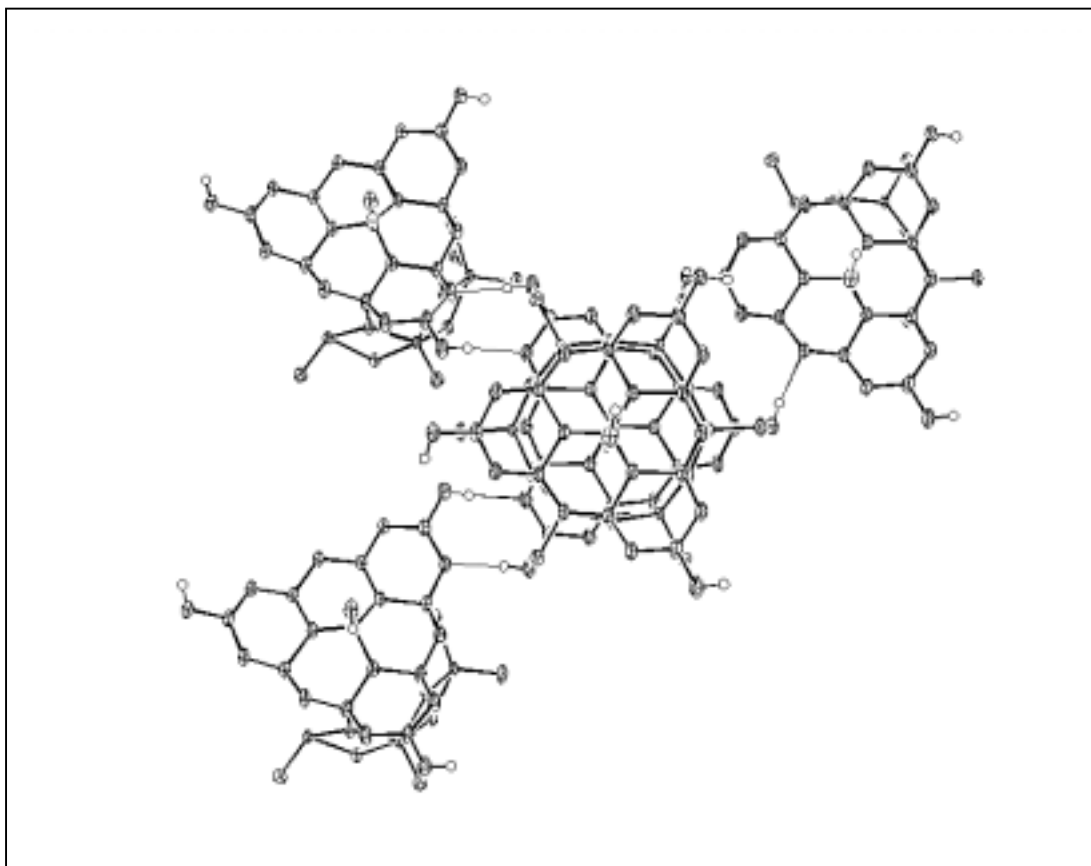


Figure 5.4. Hydrogen Bonds Between Clusters.

The third equatorial hydrogen bond interaction can be seen on the upper right corner of Figure 5.4. Similar equatorial OH groups interact with the central μ_2 -O atom of an adjacent cluster to give a 12-connected -B-O-H...O-B-O-B-O-H...O-B-O- ring.

The central cluster engages in three additional raft-to-raft hydrogen bond interactions in the layer above the plane of the drawing. These additional hydrogen bonds are identical to the three interactions described above and are related to them through the inversion center at the heart of the cluster. Thus there are parallel hydrogen bonded layers of the raft portions of the clusters connected into a three dimensional network by the covalent bonds of the cluster. Hydrogen bond parameters are given in Table 5.4.

Table 5.4. Hydrogen Bond Parameters for $[\text{enH}_2]_5[\text{V}_6\text{B}_{20}\text{O}_{50}\text{H}_8]\cdot 7\text{H}_2\text{O}$.

D-H	d[D-H]	d(H...A)	<DHA	d[D...A]	A
O1-H1	0.82	1.922	172.4	2.734	O89
O4-H4	0.82	1.915	176.4	2.735	O67
O7-H7	0.82	1.894	170.1	2.681	O45
O10-H10	0.82	2.109	157.6	2.884	Ow
O10'-H10	0.82	2.172	155.6	2.926	Ow
N2-H2A	0.89	1.993	150.32	2.801	O21
N2-H2B	0.89	1.814	173.97	2.701	O56
N2-H2C	0.89	2.044	170.11	2.925	O41
N11-H11A	0.89	2.010	150.14	2.817	O89
N11-H11B	0.89	2.176	130.17	2.842	O10
N11-H11C	0.89	2.066	145.49	2.845	N4
N12-H12A	0.89	2.385	145.77	3.161	O31
N12-H12B	0.89	2.204	127.11	2.831	O91
N12-H12C	0.89	2.365	129.61	3.011	N4
N5-H5A	0.845	1.753	169.98	2.589	O9F
N5-H5B	0.793	2.242	170.89	3.028	O11
N5-H5C	1.042	1.751	176.65	2.793	O1

An extended two dimensional array of the hydrogen bonded raft portions of the clusters is given in Figure 5.5. The layers above and below are generated by the inversion centers in the V_6O_{18} band. The nearly rectangular pores visible in Figure 5.5. interconnect with additional identical pores in the layers above and below to produce a three dimensional channel structure analogous to those found in zeolites. In the current structure the channels are filled with ethylene diammonium counter ions and water molecules which are extensively hydrogen bonded to each other and to oxygen atoms of the surrounding clusters.

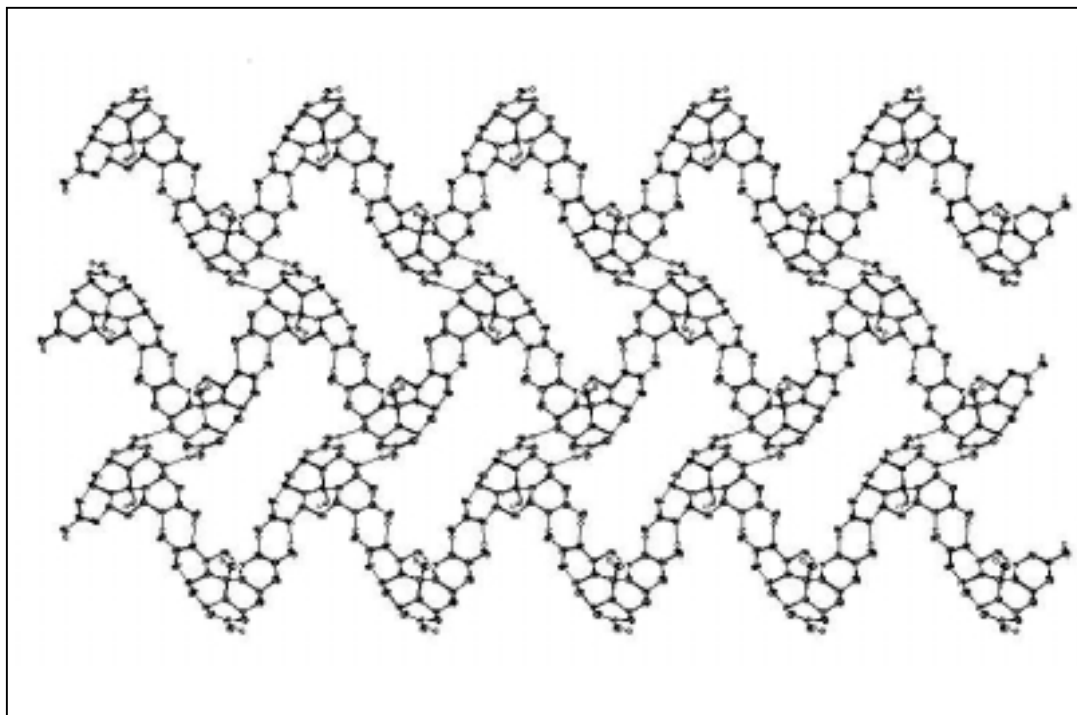


Figure 5.5. Projection of Half-Clusters on the *bc* Plane.

The cluster itself is not new. It was first reported and characterized as the octaanionic $[V_6B_{20}O_{50}H_8]^{8-}$ cluster (Williams, Wu, Sung, Zhang & Yu, 1998) which was also prepared in the presence of ethylenediamine and contains four dicationic ethylenediammonium counterions and 8.5 water molecules. The vanadium atoms are in the +4 oxidation state and the dications and water molecules reside in the channels surrounding the cluster network as in the current compound. The cluster also occurs (Williams, Wu, Sung, Zhang & Yu, 1998) in the one dimensional chain polymer, $[H_2en]_4[Hen]_2[V_6B_{22}O_{53}H_8] \cdot 5H_2O$ which formally contains the same $[V_6B_{20}O_{50}H_6]^{10-}$ cluster reported in this study with the hydroxyls in the centers of the raft-like caps of the subunits replaced with linear diborate $[B_2O_3H_2]$ bridges. Again, the channels surrounding the clusters are filled with hydrogen bonded cations and water molecules. Warren, Rijssenbeek, Rose, Haushalter & Zubieta (1998) have also reported the same cluster synthesized in the presence of rubidium counterions rather than in the presence of ethylenediamine. The vanadium atoms are in the +4 oxidation state, and the atom connectivity of the cluster is the same as the other three examples of the cluster. However, in contrast to the other examples, the oxygen atoms at the central tetrahedral raft-like BO_4 group possess terminal $B-O^-$ groups collinear with the

pseudo 3-fold axis of the cluster and six -OH group radiating out from the triangular raft-like $[\text{B}_{10}\text{O}_{16}(\text{OH})_6]^{8-}$. The large channel spaces seen in the ethylenediammonium systems is absent. The spaces between adjacent $[\text{V}_6\text{B}_{20}\text{O}_{38}(\text{OH})_{12}]^{4-}$ clusters contain only the four Rb^+ cations and one half of a water molecule per cluster.

Chapter VI

Conclusions

$\text{NiV}_2\text{O}_6 \cdot 2\text{H}_2\text{O}$ has been prepared under hydrothermal conditions by reaction of nickel acetate with vanadium(V) oxide in the presence of ethylenediamine or simply by reaction of nickel nitrate with ammonium metavanadate. $\text{CoV}_2\text{O}_6 \cdot 2\text{H}_2\text{O}$ has also been prepared under hydrothermal conditions by reaction of cobalt acetate with vanadium(V) oxide in the presence of ethylenediamine. The isomorphous compounds crystallize in an extended three dimensional framework as expected.

The structure consists of chains of VO_4 tetrahedra linked through two of the oxygen atoms propagating approximately along the [100] direction. The remaining two oxygen atoms of the VO_4 tetrahedra are shared with M atoms. Adjacent VO_4 chains are interconnected by MO_6 octahedra where each of the four equatorial oxygen atoms is shared with a VO_4 oxygen atom of a different chain, and the axial oxygen atoms are waters of hydration. Channels along the [001] direction are bounded on two sides by single MO_6 octahedra and on the other two sides by connected pairs of VO_4 tetrahedra and are too small to be of use for molecular absorption. The waters of hydration occur as hydrogen bonded pairs, which if removed would leave porous channels along the [010] direction bounded by -Td-Td-Td-Oh-Td-Td-Td-Oh rings. The vanadium atoms are in the +5 oxidation state and the nickel or cobalt atoms are in +2 oxidation state, consistent with the bond length and angle data and confirmed by bond valence calculations.

There are three distinct O-H...O hydrogen bond types, one between the two water molecules and the other two from water to framework oxygen atoms. The water stretching region in the infrared spectrum shows three resolved bands corresponding to the change in the O-H force constants when the hydrogen atoms are donated into hydrogen bond interactions.

Thermal analysis shows a two step dehydration process, the first step at 196-245 °C corresponding to loss of about 1.7 molecules of water and the second step at 125-340 °C corresponding to loss of about 0.3 molecules of water. Thermodiffraction

tometry shows that during the first process the crystal integrity is lost. Presumably this is due to water making up a large fraction of the volume of the compound. As the waters are lost during the dehydration process the metal oxide framework can not support itself and collapses. Thus, while these materials are microporous, they are unlikely to have useful microporous applications.

The second vanadium containing compound studied is the supramolecular material $[\text{enH}_2]_5[\text{V}_6\text{B}_{20}\text{O}_{50}\text{H}_8]\cdot 7\text{H}_2\text{O}$ consisting of five ethylenediammonium dications, an anionic vanadium polyborate cluster, $[\text{V}_6\text{B}_{20}\text{O}_{50}\text{H}_8]^{-10}$, and seven water solvate molecules.

The $[\text{V}_6\text{B}_{20}\text{O}_{50}\text{H}_8]^{-10}$ cluster consists of a central V_6O_{18} band of six square-pyramidal vanadium(IV) vanadyl groups ($d[\text{V}=\text{O}] = 1.612\text{-}1.632(2)$, $d[\text{V}-\text{O}] = 1.935\text{-}1.968(33)$ Å) which is capped top and bottom by triangular raft-like $[\text{B}_{10}\text{O}_{16}\text{H}_4]$ ligands, each terminated by four hydroxyl groups. The anionic vanadium borate clusters interact by $\text{O}-\text{H}\cdots\text{O}$ hydrogen bonding from the raft portions of the cluster using the eight hydroxyl groups and one bridging water molecule to form a three dimensional porous supramolecular array.

Charge balance is maintained by the ethylene diammonium counter ions which are located in the channels surrounding the clusters. They, along with the clusters and the water molecules form an extensive $\text{N}-\text{H}\cdots\text{O}$ and $\text{O}-\text{H}\cdots\text{O}$ hydrogen bonded network completely filling the channels.

Suggestions for Further Work

$\text{MV}_2\text{O}_6\cdot 2\text{H}_2\text{O}$: The nature of the water coordination could be explored further. There are three bands in the FTIR spectrum corresponding with the three different hydrogen bonds in the compound. Use of a variable temperature infrared study may shed further light on the precise nature of the bonds, and in conjunction with thermal analysis and diffraction studies may add to our understanding of the dehydration process.

The thermal analysis results indicate a rich solid state phase space in the upper ranges of temperature studied, and the diffraction results indicate crystalline materials forming at the same time. Additional studies of the higher temperature products should prove to be interesting.

$[\text{V}_6\text{B}_{20}\text{O}_{50}\text{H}_8]^{n-}$: The four existing examples of this cluster exhibit three quite different supramolecular structures, ranging from the cluster dense array formed with rubidium cations to the large channel separations between clusters with the ethylenediamine derived systems and the one dimensional polymeric cluster chains system. Additional syntheses under similar hydrothermal conditions with other cations is expected to provide additional interesting supramolecular networks. The ion exchange properties of these materials could prove to be interesting as well.

References

References

- Altomare, A., Cascarano, G., Giacobazzo, G., Guagliard, A., Burla, M. C., Polidori, G. & Camalli, M. (1994). *J. Appl. Cryst.*, 27: 435-436.
- Atwood, J. L., Davies, J. E., MacNicol, D. D. & Vögtle, F. (1996). "Comprehensive Supramolecular Chemistry", Elsevier Science Ltd.
- Baudrin, E., Touboul, M. & Nowogrocki, G. (2000). *J. Sol. State Chem.*, 152: 511-516.
- Berrah, F., Leclaire, A., Borel, M-M., Guesden, A. & Raveau, B. (1999). *Acta Cryst*, C55: 288-291.
- Blessing, Robert H. (1995). *Acta Cryst.*, A51: 33-37.
- Blessing, Robert H. (1997). *J. Appl. Cryst.*, 30: 421-426.
- Brese, N. E. & O'Keeffe, M. (1991). *Acta Cryst.*, B47: 192-197.
- Broussely, M., Biensan, P. & Simon, B. (1999). *Electrochimica Acta*, 45: 3-22.
- Brown, I. D. & Altermatt, D. (1985). *Acta Cryst.*, B41: 244-247.,
- Chatkon, A & Haller, K. J. (2000). "Crystal Structure of the Supramolecular Nickel Vanadium Oxide, NiV₂O₆.2H₂O", 26th Congress on Science and Technology of Thailand, Bangkok, Thailand: Abstract 18-I2P-13.
- Chirayil, T., Zavalij, P. Y. & Whittingham, M. S. (1998). *Chem. Mater.*, 10: 2629-2640.
- Clegg, W. (1998). "Crystal Structure Determination". Oxford University Press Inc.:New York.
- Dagani, R. (1997). News of the Week section. *Chem. Eng. News*, December 1, p4.
- Dagani, R. (1998). Science/Technology section. *Chem. Eng. News*, June 8, 35-46.
- Desiraju, G. R. (1995). *Angew. Chem., Int. Ed. Engl.*, 34: 2311-2327.
- Drain, C. M., Nifiatis, F., Vasenko, A. & Batteas, J. D. (1998). *Angew. Chem., Int. Ed. Engl.*, 37: 2344-2347.
- Evans, C. C., Sukarto, L. & Ward, M. D. (1999). *J. Am. Chem. Soc.*, 121: 320-325.
- Feng, P., Bu, X. & Stucky, G. D. (1997). *Nature*, 388: 735-741.
- Fernández, S., Mesa, J. L., Pizarro, J. L., Lezama, L., Arriortua, M. I., Olazcuaga, R. & Rojo, T. (2000). *Chem. Mater.*, 12: 2092-2098.
- Fur, E. L., Riou, A., Pena, O. & Pivan, J. Y. (2000). *Sol. State Sci.*, 2: 135-141.
- Funeriu, D. P., Lehn, J. M., Baum, G. & Fenske, D. (1997). *Chem. Eur. J.*, 3: 99.
- Fyfe, M. C. T. & Stoddart, J. F. (1997). *Acc. Chem. Res.*, 30: 393-401.
- Gao, Q., Li, B. Chen. J., Li, S., Xu, R., Williams, I.D., Zhang, J. & Barber, D. (1997). *J. Sol. State Chem*, 129: 37-44.

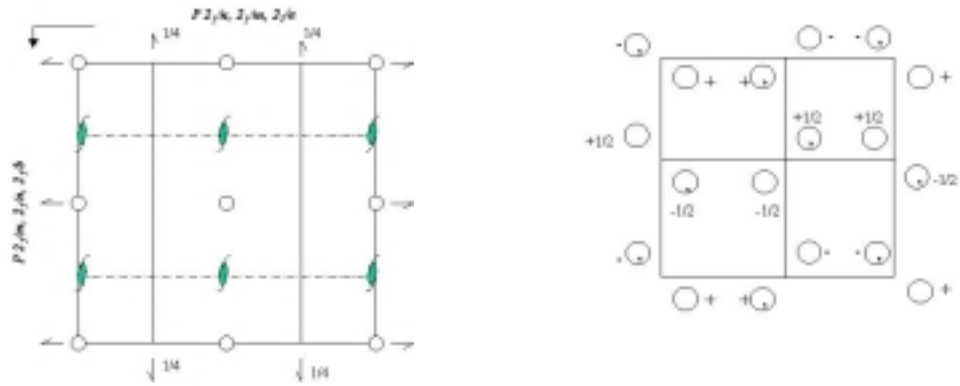
- Giacovazzo, C., Monaco, H. L., Viterbo, D., Scordari, F., Gilli, G., Zanotti, G. & Catti, M. (1992). "Fundamentals of Crystallography", Oxford University Press Inc.:New York.
- Glusker, J. P. & Trueblood, K. N. (1985). "Crystal Structure Analysis: A Primer", 2nd Edition, Oxford University Press Inc.:New York.
- Hahn, T. (1992). "International Tables for Crystallography, Volume A, Space Group Symmetry", 3rd Revised Edition, International Union of Crystallography/Kluwer Academic:Dordrecht.
- Hamilton, W. C. (1964). "Statistics in Physical Science", Ronald:New York.
- Hammond, C. (1997). "The Basics of Crystallography and Diffraction", International Union of Crystallography; Oxford University Press Inc.:New York.
- Hannon, M. J., Painting, C. L., Jackson, A., Hamblin, J & Errington, W. (1997). *Chem. Commun.*, 1807-1808.
- Haushalter, R. C. & Mundi, L. A. (1992). *Chem. Mater.*, 4: 31-48.
- Khan, M. I., Meyer, L. M., Haushalter, R. C., Schweitzer, A. L., Zubieta, J. & Dye, J. L. (1996). *Chem. Mater.*, 8: 43-53.
- Leblanc, M. & Ferey, G. (1990). *Acta Cryst.*, C46:, 15-18.
- Lewis, D. W., Freeman, C. M. & Catlow, C. R. A. (1995). *J. Phys. Chem.*, 99: 11194-11202.
- Lewis, C. W., Willock, D. J., Catlow, C. R. A., Thomas, J. M. & Hutching, G. J. (1996). *Nature*, 382: 604-607.
- Liao, J-H., Drezen, T., Leroux, F., Guyomard, D. & Piffard, Y. (1996). *Eur. J. Solid State Inorg. Chem.*, 33: 411-516.
- Lu, J. J., Xu, Y., Goh, N. K. & Chia, L. S. (1998). *Chem. Commun.*, 1709-1710.
- Mackay, S., Gilmore, C. J., Edwards, C., Tremayne, M., Stuart, N. & Shankland, K. (1998). "maXus: a computer program for the solution and refinement of crystal structure from diffraction data", U. of Glasgow, Scotland, UK, Nonius BV, Delft, and MacScience Co. Ltd., Yokohama.
- Massa, W. (2000). "Crystal Structure Determination", Springer-Verlag.
- Murashova, E. V., Velikodnyi, Y. A., Potapov, M. A. & Trunov, V. K. (1988). *Izv. Akad. Nauk. SSSR Neorg. Mater.*, 24: 519-521 (*Inorg. Mater. (Eng. Ed.)*, 519-521).
- Nonius B.V. (2000). "Collect Data Collection Software", Nonius B.V.:Delft.
- O'Keeffe, M. (1990). *Acta Cryst.*, A46: 136-142.
- Otwinowski, Z. & Minor, W. (1997). "Processing of X-ray Diffraction Data Collected in Oscillation Mode", in *Methods in Enzymology*, Vol. 276: Macromolecular Crystallography, part A, C. W. Carter & R. M. Sweet, Eds., pp307-326.
- Page, E. M. & Wass, S. A. (1997). *Coord. Chem. Rev.* 164: 203-259.
- Rhodes, G. (2000). "Crystallography Made Crystal Clear", 2nd Edition, Academic Press.

- Rijssenbeek, J. T., Rose, D. J., Haushalter, R. C. & Zubieta, J. (1997). *Angew. Chem., Int. Ed. Engl.*, 36: 1008-1010.
- Russell, V. A. & Ward, M. D. (1997). *J. Mater. Chem.*, 7: 1123-1133.
- Schindler, M., Hawthorne, F. C. & Baur, W. H. (2000). *Chem. Mater.*, 12: 1248-1259.
- Schubert, U. S. & Eisenbach, C. D. (1999). *Polymer*, 40: 222-223.
- Shannon, R. D. (1976). *Acta Cryst.*, A32: 751-767.
- Sheldrick, G. M. (1997). SHELXTL Reference Manual, Ver. 5.1, Bruker AXS, Inc. Madison.
- Shizo, M. & Fernando, Q. (1971). *Anal. Chem.* 43: 1222-1230.
- Sijbesma, R. P., Beijer, F. H., Brunsveld, L., Folmer B. J. B., Hirschberg, J. H. K. K., Lange, R. F. M., Lowe, J. K. L. & Meijer, E. W. (1997). *Science*, 278: 1601-1604.
- Soghomonian, V., Chen, Q., Haushalter, R. C., Zubieta, J. & O'Connor, J. (1993). *Science*, 259: 1596-1599.
- Stout, G. H. & Jensen, L. H. (1989). "X- Ray Structure Dermination", 2nd Edition, John Wiley & Son.
- Skyllas-Kazacos, M. & Robins, R. G. (1988). "All Vanadium Redox Battery", US Patent No. 4,786,567.
- Vansant, E. F. (1994). "Separation Technology", Elsevier.
- Wang, D., Yu, R., Kumada, N. & Kinomura, N. (2000). *Chem. Mater.*, 12: 956-960.
- Warren, C. J., Rijssenbeek, J. T., Rose, D. J., Haushalter, R. C. & Zubieta, J. (1998). *Polyhedron*, 17: 2599-2605.
- Weller, M. T. (1994). "Inorganic Materials Chemistry", Oxford University Press Inc.:New York.
- Whisten, C. (1987). "X-ray Methods", John Wiley & Son:Singapore.
- Williams, I. D., Gao, Q., Chen, J., Ngai, L.-Y., Lin, Z. & Xu, R. (1996). *Chem. Commun.*, 1781-1782
- Williams, I. D., Wu, M., Sung, H.H-Y., Zhang, X. X. & Yu, J. (1998). *Chem. Commun.*, 22: 2463-2464.
- Williams, I. D., Law, T. S-C., Sung, H. H-Y., Wen, G. H. & Zhang, X. X. (2000). *Sol. State Sci.*, 2: 47-55.
- Wills, A. S. & Brown, I. D. (1999). VaList, Commissariat l'Energie Atomique, France.
- Yamase, T., Suzuki, M. & Ohtaka, K., (1997). *J. Chem. Soc., Dalton Trans*, 2463-2472.
- Yu, J., Sung, H. H-Y. & Williams, I. D. (1999). *J. Sol. State Chem.*, 142: 244-246.
- Zavalij, P. & Whittingham, M. S. (1999). *Acta Cryst.*, B55: 627-663.

Appendices

Appendix A

Space group *Pnma* (No. 62)



Origin at $\bar{1}$ on $1\ 2_1\ 1$

Asymmetric unit $0 \leq x \leq \frac{1}{2};\ 0 \leq y \leq \frac{1}{4};\ 0 \leq z \leq 1$

Symmetry operations

(1) 1 (2) $2\ (0,0, \frac{1}{2})\ \frac{1}{4};0,z$ (3) $2\ (0,\frac{1}{2},0)\ 0,y,0$ (4) $2\ (\frac{1}{2},0,0)\ x,\frac{1}{4};$
 $\frac{1}{4}$

(5) $\bar{1}\ 0,0,0$ (6) $a\ x, y, \frac{1}{4}$ (7) $m\ x, \frac{1}{4},z$ (8) $n(0,\frac{1}{2},\frac{1}{2})$
 $\frac{1}{4};y,z$

Multiplicity 8

Coordinates

(1) x, y, z (2) $-x+\frac{1}{2},-y,z+\frac{1}{2}$ (3) $-x,y+\frac{1}{2},-z$ (4) $x+\frac{1}{2},-y+\frac{1}{2},-$
 $z+\frac{1}{2}$

(5) $-x,-y,-z$ (6) $x+\frac{1}{2},y,-z+\frac{1}{2}$ (7) $x,-y+\frac{1}{2},z$ (8) $-x+\frac{1}{2},y+\frac{1}{2},z+\frac{1}{2}$

Reflection conditions

General: $0kl : k+l = 2n$

$hk0 : h = 2n$

$h00 : h = 2n$

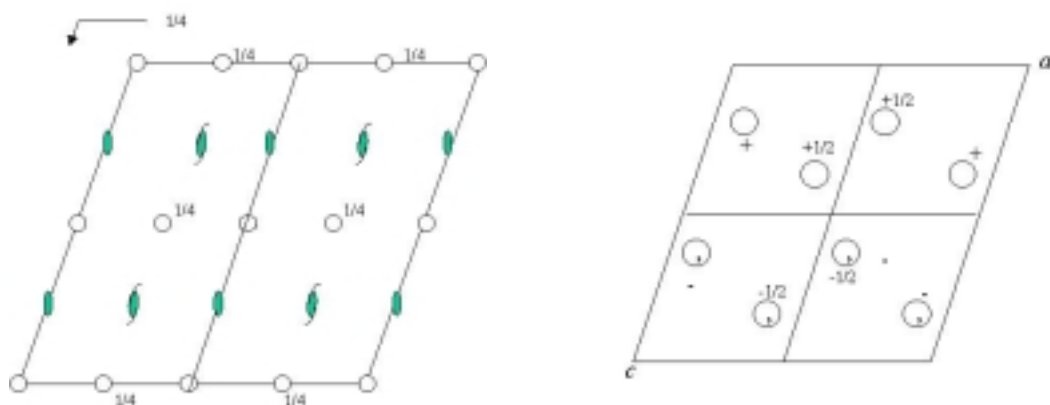
$0k0 : k = 2n$

$00l : l = 2n$

Space group $C2/c$ (No. 15)

UNIQUE AXIS b , CELL CHOICE 1

$C 1 2/c 1$



Origin at $\bar{1}$ on glide plane c

Asymmetric unit $0 \leq x \leq 1/2$; $0 \leq y \leq 1/2$; $0 \leq z \leq 1/2$

Generators selected

(1) $t(1,0,0)$ $t(0,1,0)$ $t(0,0,1)$ $t(1/2,1/2,0)$

Multiplicity 8

Coordinates

(0,0,0)⁺ (1/2,1/2,0)⁺
 (1) x, y, z (2) $-x, y, -z+1/2$ (3) $-x, -y, -z$ (4) $x, -y, z+1/2$

Reflection conditions

General: $hkl : h+k = 2n$

$h0l : h, l = 2n$

$0kl : k = 2n$

$hk0 : h+k = 2n$

$0k0 : k = 2n$

$h00 : h = 2n$

$00l : l = 2n$

Appendix B

Bond Valence Calculation

Determine the chemical connectivity in an inorganic crystal express used to describe are bond length and bond valence when bond length between atoms are correlated with formal valences of species, the total strength of the valency bonds which reach an ion from all neighboring atom is equal to the charge of ion.

The bond valence model work remarkably formal valence, coordination number and bond length by equation below (Brown & Altermatt, 1985, Brese & O'Keeffe, 1991).

$$s_{(ij)} = (\exp[R_{0(ij)} - R_{(ij)}] / B_{(ij)})$$

$$V_i = \sum_j s_{(ij)}$$

$s_{(ij)}$ is valence of bond between the cation i and the anion j

$R_{(ij)}$ is bond length between pairs of atom in structure

$R_{0(ij)}$ is bond length between pairs of atom in observed crystal structure (empirically)

$B_{(ij)} = 0.37$ (the slope of the correlation curve from empirically)

V_i is oxidation state of cation i where the sum over all neighboring atom j, with each bond between atom i and j having bond valence $s_{(ij)}$

Determining the valence of hydrogen bonds using graph should be careful because hydrogen not well located, the hydrogen has a strong bond to donor anion and weak bonded to acceptor anion when hydrogen has +1 oxidation state then bond valence of D-H is best determined by subtracting the sum of $H \cdots A$ valences from 1.0.

The bond valence use for determining the oxidation state, especially in mixed valence compound, for checking if the structure is correct or for predicting new structure.

Appendix C

Ring Fourier Calculation

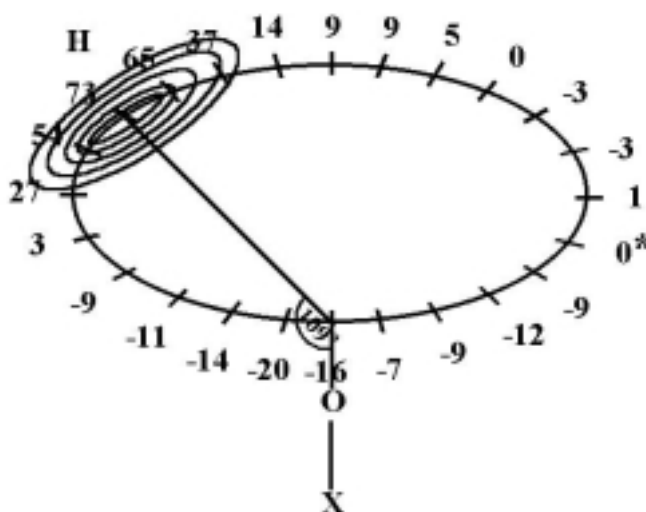
It's difficult to locate hydrogen atom accurately in structure because hydrogen has low scattering power. Ring Fourier Calculation is a method purposed to calculate the hydrogen position by calculated maximum electron density around the cycle of element expected bonded with hydrogen with fixed X-H distance and Y-X-H.

Example of Ring Fourier Calculation

(1). HFIX 147 is idealized -OH group with X-OH angle tetrahedral when H atoms are ride on atom O and rotate about the X-O bond that show resulted below

Difference electron density Fourier synthesis were calculated at 15 degree intervals around the circle which represents the locus of possible hydrogen atom positions determined by the normal O-H distance and eclipsed (cis) to nearest nonhydrogen atom bonded to the X atom. Rotation is clockwise looking down X to O.

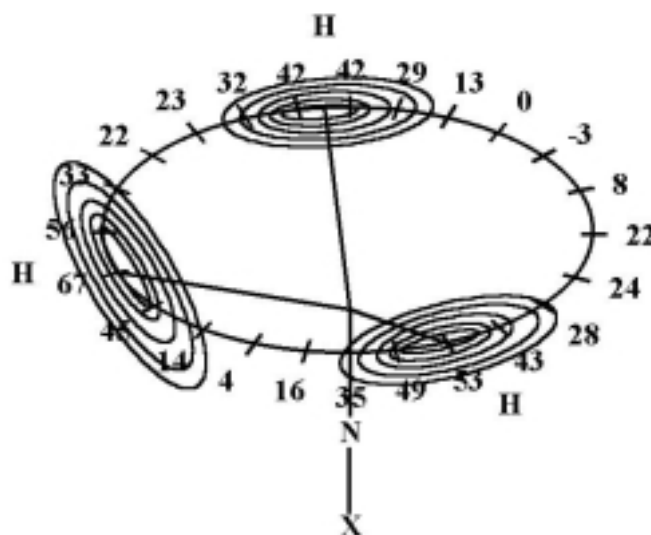
73	65	37	14	9	9	5	0	-3	3	1	0*
-9	-12	-9	-7	-16	-20	-14	-11	-9	3	27	54



(2). HFIX 137 is idealized -NH_3 group with tetrahedral angle, otherwise when H atoms are ride on atom N and rotate about the N-X bond that show resulted below

Difference electron density Fourier synthesis were calculated at 15 degree intervals around the circle which represents the locus of possible hydrogen atom positions determined by the normal N-H distance and eclipsed (cis) to nearest nonhydrogen atom bonded to the X atom. Rotation is clockwise looking down X to N.

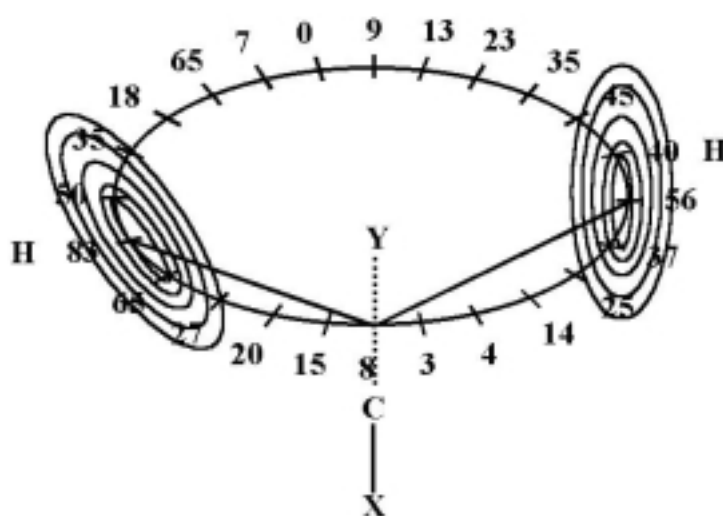
22	23	32	42	42	29	13	0	-3	8	22	24*
28	43	53	49	35	16	4	14	45	67	56	33



(3) HFIX 23 is idealized secondary $-\text{CH}_2$ group with all X-C-H and Y-C-H angles equal, when H-C-H determined by X-C-Y and coordinate of H atoms are riding on atom C that show resulted below

Difference electron density Fourier synthesis were calculated at 15 degree intervals around the circle which represents the locus of possible hydrogen atom positions determined by the normal C-H distance and eclipsed (cis) to nearest nonhydrogen atom bonded to the X atom. Rotation is clockwise looking down X to C.

18	15	7	0	9	13	23	35	45	40	56	37*
25	14	4	3	8	15	20	27	65	83	-50	35



Curriculum Vitae

AUNGKANA CHATKON

e-mail : tuy448@yahoo.com

Born: October 16, 1973, Sakaeo

Citizenship: Thailand

Marital Status: Single

Education

1991-1994 B.Sc., Chemistry
Rajabhat Institute, Nakhon Ratchasima, Thailand

Experience

1994-1998 Teaching Chemistry at Secondary School
Takasaem Pittaya Secondary School, Sakaeo

Presentations

"Crystal Structure of the Supramolecular Nickel Vanadium Oxide, $\text{NiV}_2\text{O}_6 \cdot 2\text{H}_2\text{O}$ ", (with Kenneth J. Haller), 26th Congress on Science and Technology of Thailand, Bangkok, Thailand: Abstract 18-I2P-13, 2000.

"Crystal Structure of the Anionic Vanadium Borate Cluster, $[\text{V}_6\text{B}_{20}\text{O}_{50}\text{H}_8]$." (with Kenneth J. Haller) 27th Annual Meeting of the Science Society of Thailand, Hat Yai, Thailand, 2001.

"X-Ray Crystal Structure of the Supramolecular Calcium Vanadium Oxide, CaV_2O_6 ", (with Kenneth J. Haller), AsCA'01, 4th Asian Crystallographic Association Meeting, Bangalore, India: Abstract A4-8, 2001.

"Crystal Structures of Supramolecular Metavanadate Compounds" (with Kenneth J. Haller), 3rd National Graduate Student Symposium, Suranaree University of Technology, Nakhon Ratchasima 30000, Abstract accepted for presentation.

Scholarships and Honors:

Undergraduate, Thai Government Scholarship, Ministry of Education.

Graduate, Thai Government Scholarship, Ministry of Education.

Travel Scholarship to present paper at AsCA'01, Bangalore, India

MacScience Registration Scholarship Grant for AsCA'01, Bangalore, India